Deliverable 8.10: Chemical and structural / crystallographic properties of simulated fuel pellets and irradiated fuel pellets at the cladding / fuel interface

Work Package 8 SFC

The project leading to this application has received funding from the European Union's Horizon 2020 research and innovation programme under grant agreement No 847593.

Document information

Project Acronym	**EURAD**
Project Title	**European Joint Programme on Radioactive Waste Management**
Project Type	**European Joint Programme (EJP)**
EC grant agreement No.	**847593**
Project starting / end date	**1st June 2019 – 30 May 2024**
Work Package No.	**8**
Work Package Title	**Spent Fuel Characterisation and Evolution Until Disposal**
Work Package Acronym	**SFC**
Deliverable No.	**8.10**
Deliverable Title	**Chemical and structural / crystallographic properties of simulated fuel pellets and irradiated fuel pellets at the cladding / fuel interface**
Lead Beneficiary	**KIT**
Contractual Delivery Date	**M60**
Actual Delivery Date	**M60**
Type	**Report**
Dissemination level	**PU**
Authors	**Tobias König (KIT), Michel Herm (KIT), Volker Metz (KIT), Nieves Rodriguez Villagra (CIEMAT), Jone M. Elorrieta (CIEMAT), Abel Milena-Pérez (CIEMAT), Laura J. Bonales (CIEMAT), Luis Gutiérrez (CIEMAT), Sergio Fernández-Carretero (CIEMAT), Ana Núñez (CIEMAT), Hitos Galán (CIEMAT), Márton Király (HUN-REN EK), Johannes Bertsch (PSI), Liliana Isabel Duarte (PSI), Kari Goutam (PSI), Chloé Schneider (PSI).**

To be cited as:

König T., Herm M., Metz V., Rodriguez Villagra N., Elorrieta J. M., Milena-Pérez A., Bonales L. J., Gutiérrez L., Fernández-Carretero S., Núñez A., Galán H., Király M., Bertsch J., Duarte L. I., Goutam K., Schneider C., Zencker U. (2024). Final version as of 10.05.2024 of deliverable D8.10 of the HORIZON 2020 project EURAD. EC Grant agreement no: 847593.

Disclaimer

Acknowledgement

This document is a deliverable of the European Joint Programme on Radioactive Waste Management (EURAD). EURAD has received funding from the European Union's Horizon 2020 research and innovation programme under grant agreement No 847593.

Status of deliverable		
	By	Date
Delivered (Lead Beneficiary)	Tobias König (KIT)	10/05/2024
Verified (Task Leader)	Uwe Zencker	12/05/2024
Reviewed (Reviewers)	Fredrik Johansson	12/05/2024
Approved (PMO)	Paul Carbol	13/05/2024
Submitted to EC (Coordinator)	Andra (Coordinator)	17/05/2024

Executive Summary

The European Joint Programme on Radioactive Waste Management (EURAD) focusses on the European wide collaboration towards the safe and robust radioactive waste management. In EURAD, the work package (WP) “Spent Fuel Characterisation and Evolution until Disposal” (SFC) foresees to develop and document an experimentally verified procedure to accurately determine the source term of irradiated spent nuclear fuels (SNF), in order to establish a profound scientific database to understand the physicochemical evolution of SNF compounds, i.e., pellets and claddings.

Subtask 3.3 within the EURAD SFC WP contributes to the knowledge increase on pellet-cladding interaction under conditions of extended storage, transport and handling of SNF rods. The aim is to get deeper insights in particularly chemical effects of activation and fission products on the cladding integrity, as well as activity release considerations under dry storage and subsequent transportation conditions.

This final report summarises the experimental results gained within subtask 3.3 until the 48th month of the project. The research groups contributing with experiments are Centro de Investigaciones Energétic, Medioambientales y Tecnológicas (CIEMAT), Karlsruher Institut für Technologie – Institut für Nukleare Entsorgung (KIT-INE), HUN-REN Energiatudományi Kutatóközpont (HUN-REN EK) and Paul Scherrer Institut (PSI). Analyses of pellet-cladding interactions were performed using non-irradiated UO_2 fuel, as well as high burn-up UO_2 and mixed oxide (MOX) fuel, irradiated in commercial pressurised water reactors (PWR). The morphological and chemical/spectroscopic analyses of fuel-cladding interfaces and claddings were performed by means of X-ray photoelectron spectroscopy (XPS), X-ray diffractometry (XRD), Raman spectroscopy, scanning electron microscopy in conjunction with energy dispersive X-ray spectroscopy (SEM-EDX) as well as X-ray absorption spectroscopy (XAS) to elucidate the pellet-cladding chemical interaction mechanisms and chemical speciation.

The outcomes and insights of the work performed within this report, help to gain a deeper understanding of the processes occurring during interim storage of spent nuclear fuel rods by using state-of-the-art methods in different laboratories. It is demonstrated, that the effect of hydrogen loading, oxygen ingress and temperature affect the integrity of fuel rod claddings during non-accident scenarios. Furthermore, spectroscopic analyses performed on actual SNF specimens, elucidate the importance of research on irradiated specimens in order to describe the different processes occurring during irradiation and subsequent storage of SNF assemblies, which may affect the later handling and conditioning of the fuel rods for disposal in a geological disposal facility.

Altogether, the results obtained within subtask 3.3 of the EURAD SFC WP help to understand the physicochemical parameters and properties of SNF claddings throughout the nuclear fuel cycle. Maintaining the integrity of the cladding tube during the interim storage period until relocation into a geological disposal facility is of utter importance in order to prevent the release of radionuclides into the biosphere.

Table of Content

List of Figures

List of Tables

Glossary

ADU	Ammonium Di-Uranate
BU	Burn-up [GWd/t_{HM}]
BSE	Backscatter electron
BWR	Boiling water reactor
CIEMAT	Centro de Investigaciones Energétic, Medioambientales y Tecnológicas
EDS/EDX	Energy dispersive X-ray spectroscopy
EPMA	Electron probe micro analysis
FCI	Fuel-cladding interaction
FIB	Focussed ion beam
FP	Fission products
HBU	High burn-up
HBS	High burn-up structure
HUN-REN EK	HUN-REN Energiatudományi Kutatóközpont
IET	Institute for Energy and Transport
IW	Integral work
JRC	Joint Research Centre
KIT-INE	Karlsruher Institut für Technologie – Institut für Nukleare Entsorgung
KKG	Nuclear power plant Gösgen
KWO	Nuclear power plant Obrigheim
LWR	Light water reactor
MOX	Mixed oxide
MRT	Maximum reaction temperature
NPP	Nuclear power plant
NRC	Nuclear Regulatory Commission
OOT	Oxidation onset temperature
PSI	Paul Scherrer Institut
PWR	Pressurised water reactor
RQA	Rietveld refinement quantitative analysis
RR_{MRT}	Reaction rate at maximum reaction temperature
SEM/STEM	Scanning (transmission) electron microscopy
SLS	Swiss Light Source
SNF	Spent nuclear fuel
TGA	Thermogravimetric analysis
VVER	Water-water cooled reactor
XAS	X-ray absorption spectroscopy

XPS	X-ray photoelectron spectroscopy
XRD	X-ray diffraction
XRF	X-ray fluorescence spectroscopy

1. Introduction

After utilisation in a nuclear power reactor and the subsequent storage period in spent nuclear fuel pools, many countries envisage storing used fuel assemblies in dry interim storage facilities until their conditioning for final disposal in a deep geological repository. During the interim storage period, the nuclear fuel assemblies are emplaced in storage or dual-purpose casks, which provide shielding from the abiding radioactivity due to decay of radioactive isotopes. However, due to the absence of an operational final repository for highly radioactive waste up until now and the subsequent time spans until construction and commissioning of the facility, a prolongation of dry interim storage is inevitable.

Several chemical and physical effects may alter the cladding integrity of the zirconium-based alloys throughout in-reactor usage and the subsequent dry storage period, potentially impacting the latter handling, transport and conditioning of fuel assemblies, such as [1,2]:

- Irradiation damage induced by alpha emitters.
- Delayed hydride cracking.
- Air oxidation.
- Stress corrosion cracking.
- Fuel-cladding chemical interactions.

Especially nuclear fuels experiencing high stress loads, such as high burn-up UO_2 or mixed oxide (MOX) (U, Pu)O_2 fuels are susceptible for cladding degradation throughout the storage period [3].

1.1 Spent nuclear fuel

The main product arising from energy production using nuclear fission is spent nuclear fuel (SNF). During utilisation in a nuclear reactor, several reactions take place, altering the initial composition of the pristine UO_2 or MOX (U, Pu)O_2 fuel. One substantial nuclear reaction is the fission of heavy nuclei (e.g., ^{235}U, ^{239}Pu) under neutron emission, generation of fission fragments and the release of a large amount of energy. Furthermore, transuranium isotopes, such as neptunium, plutonium or americium, are built-up through neutron capture reactions and subsequent β^- decays, starting from ^{238}U. However, the final composition of SNF is subject to various factors, e.g., the initial type of fissile material, the enrichment of the fissile material, reactor operation conditions such as linear power rate or burn-up [4].

The distribution and chemical state of the individual fission products and transuranium isotopes can be categorised in five groups, however transitions for certain isotopes between the groups occur [5,6]:

1. Volatile fission products and fission gases (e.g., Cs, I, Kr and Xe), finely dispersed in bubbles or present in voids within the fuel matrix.
2. Fission products characterised as ε-particles (e.g., Mo, Tc, Ru, Rh and Pd), precipitated as metallic solid solutions and immiscible with the fuel matrix.
3. Perovskite-type oxide precipitates (e.g., Rb, Sr, Zr and Ba).
4. Fission products forming solid solutions with the matrix (e.g., Y, Zr, Nb and the lanthanides).
5. Transuranium isotopes and lanthanides substituting uranium within the fuel matrix. (e.g., Np, Pu and Am).

In addition to fission products and transuranium isotopes, activation products such as ^{14}C and ^{36}Cl, generated through neutron capture reactions of impurities within the fuel and cladding, are present within the irradiated material. An overview on the elemental distribution and the microstructure within the SNF pellet is shown in *Figure 1-1*.

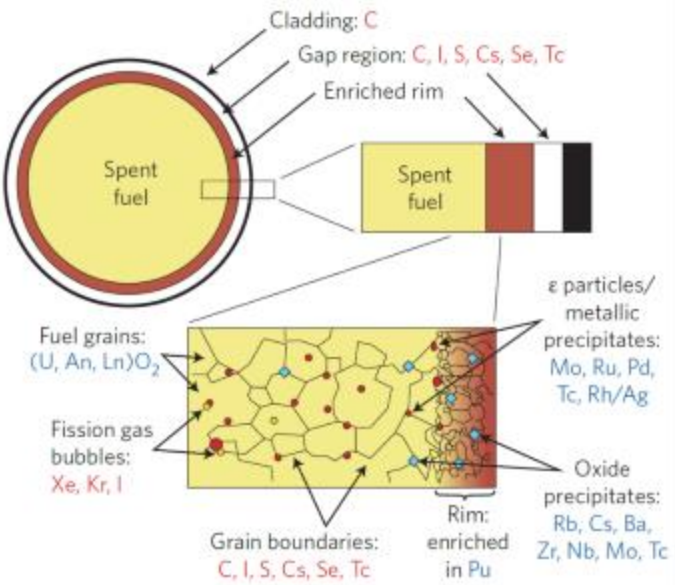

Figure 1-1: Elemental distribution and microstructure of SNF after reactor irradiation [7,8].

Especially those fission products being volatile during reactor operation such as caesium or iodine are highly mobile within the SNF matrix due to the established radial temperature gradient between the hot centre and the colder rim area adjacent to the cladding tube, which itself is in contact with the coolant. Due to this temperature difference in the pellet, the distribution of radionuclides in the fuel is largely heterogeneous, resulting in the complex chemistry of SNF [4].

1.2 Cladding tubes

Cylindrical nuclear fuel pellets are usually stacked in cladding tubes consisting of inert and corrosion resistant metal alloys. Prior to sealing of the tubes, a helium overpressure is applied to improve the heat conductivity of the fuel rods. In present light water reactor (LWR) concepts, most cladding tubes are fabricated using low-hafnium zirconium alloys due to the mechanical properties and low neutron cross section of pristine zirconium. Chemical compositions of the most used cladding alloys for boiling water reactors (BWR) and pressurised water reactors (PWR) are shown in *Table 1-1*. The individual tubes are bundled together in different lattices, depending on the reactor type, forming the nuclear fuel assembly [9,10].

Table 1-1: Chemical composition of Zircaloy-2 and Zircaloy-4 cladding alloys [11].

Alloying elements	Zry-2	Zry-4
Zirconium	balanced	balanced
Tin	1.20 – 1.70	1.20 – 1.70
Iron	0.07 – 0.20	0.18 – 0.24
Chromium	0.05 – 0.15	0.07 – 0.13
Nickel	0.03 – 0.08	-
Oxygen	0.09 – 0.16	0.09 – 0.16
Silicon	0.005 – 0.012	0.005 – 0.012
Impurities		
Aluminium	< 0.0075	< 0.0075
Boron	< 0.00005	< 0.00005
Cadmium	< 0.00005	< 0.00005
Carbon	< 0.0270	< 0.0270
Cobalt	< 0.0020	< 0.0020
Copper	< 0.0050	< 0.0050
Hafnium	< 0.0100	< 0.0100
Hydrogen	< 0.0025	< 0.0025
Magnesium	< 0.0020	< 0.0020
Manganese	< 0.0050	< 0.0050
Molybdenum	< 0.0050	< 0.0050
Nitrogen	< 0.0080	< 0.0080
Tungsten	< 0.01	< 0.01
Titanium	< 0.0050	< 0.0050
Uranium	< 0.00035	< 0.00035

Several effects strain the mechanical properties of the cladding tubes during reactor-operation and subsequent storage periods, such as an elevated hoop-stress resulting from the swelling of the nuclear fuel pellets, a creep effect induced by the radiation field or, in PWRs, an additional creep effect due to the external pressure of the coolant. Since the cladding tube displays the very first barrier preventing a release of radionuclides from the fuel, maintaining cladding integrity is one of the most crucial aspects regarding their latter handling and transport after the storage period up until their emplacement into a final repository.

1.3 The fuel-cladding interface

With burn-ups exceeding 40 GWd/t_{HM}, the initially open gap between fuel and cladding is permanently closed under formation of a fuel-cladding interaction layer. Studies performed by Ciszak and colleagues on high burn-up UO_2 fuel using Raman-spectroscopy and electron probe micro analysis indicate, that a zirconia layer is built-up between fuel and cladding displaying the adhesive interface for fuel-cladding bonding phenomena [12].

With the closed interface between fuel pellet and cladding tube, chemical interactions between both are possible. These attacks on the cladding are regarded to rely on various fission products such as iodine, caesium or tellurium intertwined with the local oxygen potential and thus the thermodynamics of the fission product – fuel system at the interface layer, the initial oxygen-to-metal ratio of the fuel and various reactor operation conditions [13]. *Figure 1-2* shows exemplarily the fuel-cladding interaction layer of a previously defueled high burn-up UO_2 specimen.

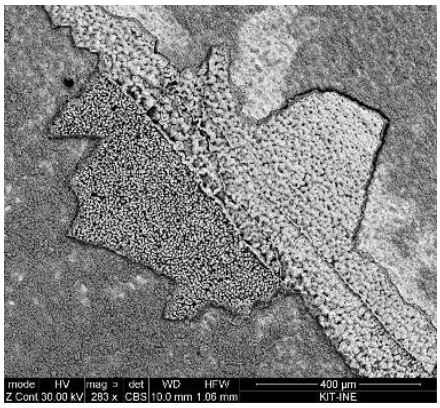

Figure 1-2: Fuel-cladding interface of a defueled high burn-up UO_2 fuel [14].

As stated in section 1.1 of this report, volatile fission products such as caesium, iodine and tellurium are subject to chemical transport processes from the central part of the fuel pellet to the cladding adherent parts due to the established temperature gradient within the fuel. This transport process is expected to occur over a vapour phase similar to a van-Arkel-de-Boer process, resulting in the enrichment of the elements in the rim area of the fuel pellet, close to the cladding surface. It is expected, that chemical interactions between the formed reaction products such as CsI or Cs2Te and the cladding tube are possible leading to some extent to cladding embrittlement processes under formation of various zirconium iodides or tellurides [15,16].

Stress corrosion cracking (SCC) processes induced by halogens, e.g., iodine, bromine and chlorine, are regarded as one of the reasons for low-ductility failures of cladding tubes [17]. All elemental halogens are able to induce SCC or pitting corrosion processes with the cladding material [18]. However, only iodine and bromine are generated by fission in sufficient amounts to enable cladding attack, while chlorine and fluorine are impurities within the fuel, resulting from manufacturing processes.

Especially the interaction of precipitated CsI near the cladding inner surface can be seen as one of the main phenomena for iodine induced SCC [19,20]. Albeit CsI being a thermodynamically relatively stable compound, it is expected, that due to the immense radiation field a radiolytically assisted dissociation of CsI could occur. As CsI dissociates, the required iodine partial pressure for cladding attack could be reached and vapour transport reactions between volatile iodine and the exposed zirconium layers of the cladding tube could occur, forming a pitting site which could lead to further embrittlement of the cladding [16,21]. Both compounds, radiolytically dissociated CsI and the resulting zirconium iodides can lead to iodine induced SCC and thus affect the cladding integrity already at temperatures within the range of 300 – 400 °C as described by Hofmann and Spino, Wood as well as Kaufmann [22–24].

2. Spectroscopic investigations on irradiated PWR high burn-up UO_2 (50.4 GWd/t_{HM}) and MOX (38.0 GWd/t_{HM}) fuel performed by KIT-INE

2.1 Introduction

After utilisation of nuclear fuel in a reactor and subsequent storage in spent fuel pools to dissipate the decay heat, many countries, such as Germany and Switzerland, envisage to emplace the irradiated fuel assemblies in storage or dual-purpose casks[1] in a dry interim storage facility. During the storage period, maintaining cladding integrity of the SNF rods is one of the main criteria regarding the latter handling and relocating of the assemblies into a suitable disposal container. Several physical and chemical phenomena may affect the cladding integrity during the storage period, such as irradiation damage by alpha emitters in the pellets rim zone, reorientation of incorporated hydrides or the interaction of cladding degrading elements such as chlorine and iodine with the zirconium-alloy.

Within this report, studies performed by KIT-INE provide experimental data concerning the analysis of pellet-cladding interaction layers of irradiated, high burn-up UO_2 (50.4 GWd/t_{HM}) and MOX (38.0 GWd/t_{HM}) fuels. Besides characterisation with SEM-EDX and XPS, high-energy resolution XAS measurements were performed at the KIT Light Source, in order to provide additional chemical speciation analyses. In the following, relevant experimental conditions and results of the spectroscopic investigations are presented.

2.2 Details of experiments with irradiated PWR UO_2 and MOX fuel at KIT-INE

Fabrication and irradiation data of the selected SNF types are given in *Table 2-1*. The examined spent UO_2 fuel specimens were sampled from the fuel rod segment N0204 of fuel rod SBS1108, which was irradiated in the PWR Gösgen (KKG, Switzerland). The fuel achieved an end-of-life burn-up of 50.4 GWd/t_{HM} during its four-cycle irradiation upon discharge in May 1989. The fuel was manufactured via a NIKUSI short term, low temperature sintering process with an initial enrichment of 3.8 % ^{235}U [25,26].

The analysed MOX fuel specimens were taken from the fuel rod 5810, which has been irradiated for four cycles in the PWR Obrigheim (KWO, Germany) until a burn-up of 38.0 GWd/t_{HM} [27,28] It was fabricated following an optimised co-milling (OCOM) manufacturing process and had an initial enrichment of 3.2 % Pu_{fiss} [28,29]. Cladding tubes of both fuel types were manufactured from Zircaloy-4.

[1] Vessels suitable for transport and storage of irradiated fuel assemblies.

Table 2-1: Fuel, cladding and irradiation data of the examined SNF specimens.

Reactor	PWR Gösgen, Switzerland	PWR Obrigheim, Germany
Fuel data	UO_2 fuel with 3.8 % enrichment of ^{235}U Pellet length = 11.0 mm Pellet diameter = 9.11 mm Initial O/U ratio = 2.002 Density = 10.41 g/cm³	MOX fuel with 3.2 % Pu_{fiss} enrichment Pellet length = 11.0 mm Pellet diameter = 9.08 mm Initial O/M ratio = 1.99 Density = 10.36 g/cm³
Cladding data	Zircaloy-4 Outer diameter = 10.75 mm	Zircaloy-4 Outer diameter = 10.75 mm
Irradiation data	Average burn-up: 50.4 GWd/t_{HM} Number of cycles: 4 Average linear power: 260 W/cm Date of discharge: 27.05.1989 Full power days: 1226 days Cooling time: approx. 33 years	Average burn-up: 38.0 GWd/t_{HM} Number of cycles: 4 Average linear power: 200 W/cm Date of discharge: 31.05.1986 Full power days: 1157 days Cooling time: approx. 36 years

Both fuel types were selected for analysis due to their initial conditions and irradiation history. The analysed UO_2 fuel was chosen due to its elevated burn-up, i.e., the burn-up range in which the initial gap area between the pristine fuel pellet and cladding tube is permanently closed under formation of a bonding rim structure and chemical as well as mechanical interactions between both are enhanced. Contrary to the homogeneous distribution of fissile material in UO_2 fuels, fissions in MOX fuels occur predominantly in the Pu-rich agglomerates, heterogeneously distributed in the fuel pellet due to the manufacturing process. Within these agglomerates, high local burn-ups exceeding 100 GWd/t_{HM} are possible, resembling the morphological change of the high burn-up structure evolved in UO_2 at burn-ups exceeding 50 GWd/t_{HM} [30–32]. Both fuels, i.e., high burn-up UO_2 and MOX fuels, are commonly referred to as the fuels with the highest stress loads and thus susceptible for cladding degrading effects during interim storage, transport and the latter handling for final disposal.

From each SNF, an approximately 2 mm disk was cut using a diamond wavering blade (IsoMet, 15LC, Buehler Ltd.) mounted on a low-speed saw (IsoMet 11-1180, Buehler Ltd.). *Figure 2-1* shows exemplarily the cutting process for the MOX fuel.

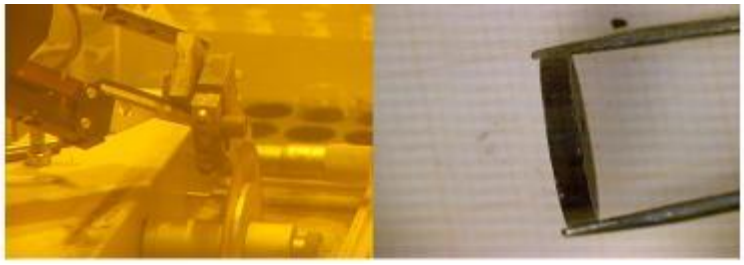

Figure 2-1: Cutting process of a 2 mm thick disk of the MOX fuel specimen.

From both fuel rod specimens, fuel fragments were retrieved by mechanical defueling of the previously cut 2 mm slices. Both fuel disks were defueled with a punch in order to obtain fuel fragments from the central region of the respective SNF disk at first. Subsequently, the fuel still attached to the cladding was removed by means of a pick and scalpel. In addition to the fuel itself, cladding specimens, previously in contact with the fuel pellet, were cut from the respective SNF sample. All specimens were removed from the hot cell and prepared for spectroscopic measurements.

For SEM-EDX and XPS analysis, the cladding specimens were previously cleaned from fines via ultra-sonic cleaning (SONOREX Super RK 225 H, Bandelin) in ultra-pure MilliQ water. Surface investigations were conducted using a Quanta 650 field emission gun SEM equipped with energy and wavelength dispersive X-ray spectrometers, as well as an ULVAC-PHI VersaProbe II spectrometer equipped with Mg Kα and Al Kα radiation sources. Data treatment were performed using the Pathfinder software and PHI MultiPak program for the SEM-EDX and XPS analyses, respectively.

Furthermore, XAS measurements of both cladding segments and fuel fragments were performed at two beamlines (INE-beamline and CAT/ACT-station), dedicated for radionuclide research, at the KIT Light Source (Karlsruhe Research Accelerator, 2.5 GeV storage ring energy). For this, a custom-built sample holder, consisting of a 25 x 25 x10 mm cubic aluminium block with a central immersion of 5 mm was manufactured as shown in *Figure 2-2*.

Figure 2-2: Custom built sample holder for XAS measurements of fuel fragments and cladding segments.

All sample holders used for XAS analysis were previously cleaned thoroughly for 30 min in isopropanol in an ultra-sonic bath in order to remove any residuals from the manufacturing process. Subsequently, the respective specimens were mounted on the sample holder and sealed with a double layer of 8 µm thick polyimide foil (KAPTON®). For the measurements, the loaded sample holders were positioned in a 45° angle to the incident X-ray beam, whereas the intensity of the beam was monitored by ionisation chambers filled with Ar.

In order to scrutinise the chemical speciation of chlorine within the specimens, Cl K-edge measurements were performed at the INE beamline equipped with a Vortex 60EX double crystal monochromator (Hitachi) and Si[111] crystals. Prior to the measurement of fuel fragments and cladding segments, an energy calibration was performed using a CsCl reference with a Cl K-edge energy of 2,824.9 keV. To ensure, that no contamination of pristine chlorine within sample holders, polyimide foil or surrounding materials in the measuring chamber biased the chlorine measurements, blank measurements with and without empty sample holders were performed as well.

For I K-edge analysis (E = 33,169 keV) at the CAT/ACT-station, a previous energy calibration was performed with crystalline CsI and KI reference materials. Measurements were performed using a pair of Ge[422] crystals as well as a 5-pixel LEGe detector in order to discriminate the fluorescence yield.

Data treatment for all measurements was performed by a prior normalisation to the edge jump of the calibrated spectra and processing using the Demeter IFEFFIT program pack as well as with the PyMCA software package[33,34].

2.3 Results and discussions of experiments performed with irradiated PWR UO_2 and MOX fuel

2.3.1 SEM-EDX and XPS analyses

Figure 2-3 depicts the SEM-EDX analysis of residual SNF on the cladding of the UO_2 fuel. As shown, the crystalline, needle-shaped precipitate present on the surface of the cladding sample consist of a mixed compound of uranium, caesium, oxygen and chlorine (see *Table 2-2*). The fission product caesium is mobile during in-reactor service and volatilises due to the high temperature in the SNF pellet. In its volatilised form it is expected to follow the established radial thermal gradient in the fuel pellet, as the centre of the pellet is significantly hotter than the peripheral part being in contact with the cladding surrounded by the primary circuit coolant [35]. In the course of this vapour transport process, initially formed caesium halides are expected to precipitate at the pellet periphery. Furthermore, caesium uranates as well as the corresponding caesium zirconates and molybdates are anticipated to form, depending on the local oxygen potential in the cladding adherent rim region [36,37]. An incorporation process of chlorine into the caesium uranate structure thus could be conceivable, which would result in the shown crystalline compounds differing from the expected CsCl stoichiometry as shown in the XAS analyses in section 1.2.2.

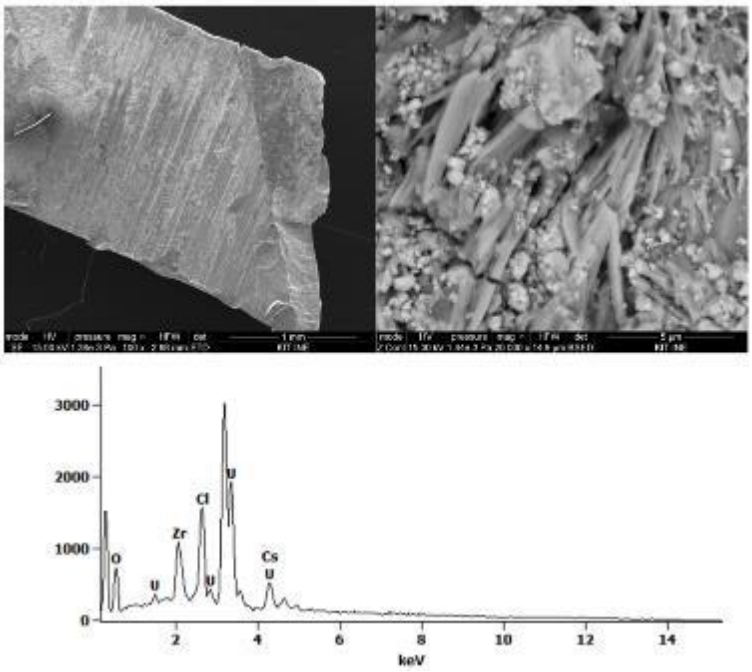

Figure 2-3: SEM-EDX spectra of chlorine rich deposits on the Zircaloy-4 cladding of the UO_2 fuel.

Table 2-2: SEM-EDX analysis of crystalline precipitate on UO_2 fuel cladding. Values are given in [at-%].

O	Cl	Cs	U
60.9±3.1	14.3±0.7	2.7±0.4	22.1±0.7

In addition to the SEM-EDX analyses for the high burn-up UO_2 fuel, investigations for a MOX cladding segment were performed as shown in *Figure 2-4*. Similar chlorine containing precipitates were identified upon the MOX cladding surface, containing additionally significant amounts of tellurium. *Table 2-3* depicts the chemical composition of the precipitates. Tellurium is a relatively abundant fission product with approximate thermal fission yields of 4.3 % for ^{235}U and 5.1 % for ^{239}Pu, suspected to cause cladding attacks in its telluride speciation (e.g., Cs_2Te, Cs_2TeO_3 or CdTe). Comparable to caesium and iodine, tellurium is expected to follow the radial temperature gradient within the fuel and is enriched in the peripheral parts of the SNF pellet adjacent to the inner surface of the cladding[38,39].

Table 2-3: SEM-EDX analysis of precipitates upon the MOX cladding surface. Values are given in [at-%].

O	Cl	Fe	Zr	Cs	Te	U
49.6±2.3	4.4±0.3	0.2±0.1	33.3±2.1	2.8±0.2	0.7±0.2	8.9±0.2

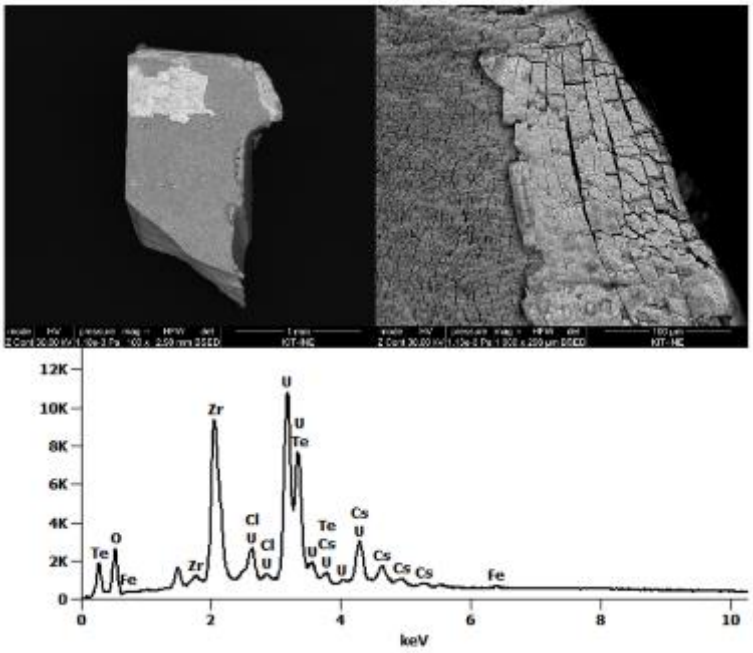

Figure 2-4: SEM-EDX analysis of chlorine rich deposits on the Zircaloy-4 cladding of the MOX fuel.

XPS survey spectra, recorded for the inner cladding surfaces previously in contact with the UO_2 and MOX fuel are shown in *Figure 2-5* and *Figure 2-6*. Both spectra show the presence of chlorine in addition to the fission products Te, Ba and Cs within the interface layer of both cladding samples. It should be noted, that iodine, presumably present as CsI within the fuel-cladding interaction layer, could not be detected by neither XPS nor SEM-EDX analysis. It is conceivable, that highly soluble CsI was dissolved during the prior cleaning of the specimens in an ultra-sonic bath with ultra-pure MilliQ water.

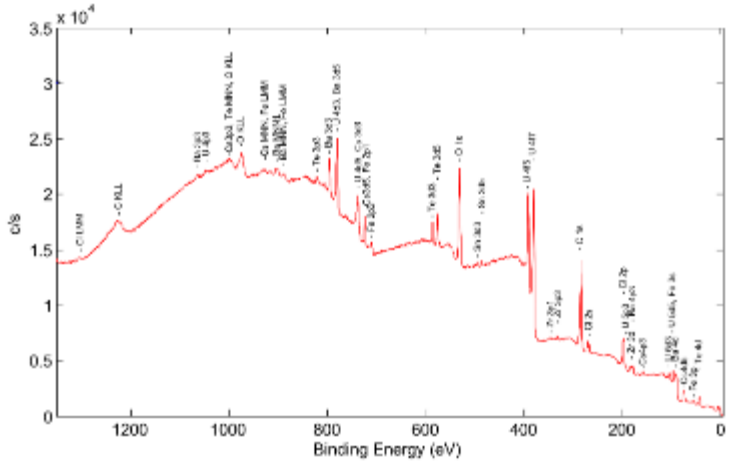

Figure 2-5: XPS spectra of the inner surface of the Zircaloy-4 cladding previously in contact with UO_2 fuel.

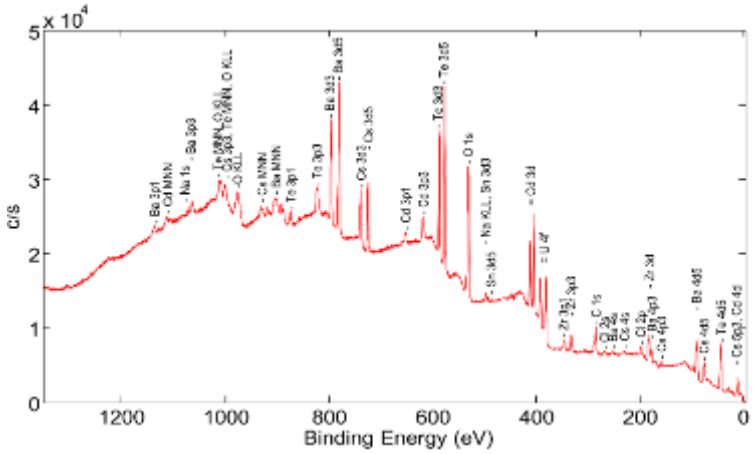

Figure 2-6: XPS spectra of the inner surface of the Zircaloy-4 cladding previously in contact with MOX fuel.

In addition to XPS survey scans, atomic concentrations of the surface area were determined for all specimens. *Figure 2-7* depicts exemplarily the MOX cladding specimen designated for XPS analysis, whereas the area of investigation is marked with a red rectangle. Similar to SEM-EDX measurements, surface analysis of the residual MOX fuel-cladding interaction layer confirms the presence of caesium, chlorine and tellurium present on the inner surface of the cladding as depicted in *Table 2-4*.

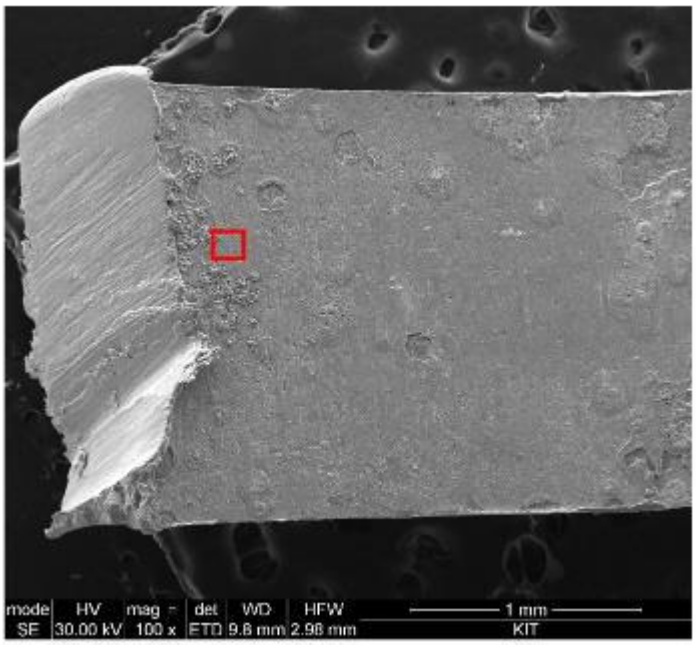

Figure 2-7: MOX cladding specimen designated for XPS analysis and area of investigation indicated by red rectangle.

Table 2-4: XPS surface analysis for selected MOX cladding area. Values are given in [at-%].

O	Cl	Cd	Te	Cs	Ba	U
79.7±12.0	1.8±0.3	0.2±0.1	1.0±0.2	4.3±0.6	5.7±0.9	7.3±1.1

In order to elucidate the speciation of chlorine within the fuel-cladding interaction layers present on the Zircaloy-4 specimens, additional narrow scans for the Cl $2p_{1/2}$ and Cl $2p_{3/2}$ elemental lines were recorded. Both cladding samples show for Cl 2p elemental lines a Cl $2p_{3/2}$ binding energy at 198.1 eV, which confirms chlorine being present in its negatively charged chloride (-I) form, as shown in *Figure 2-8*. All spectra were superposed by minor intensities of U $5p_{3/2}$ due to the strong matrix background.

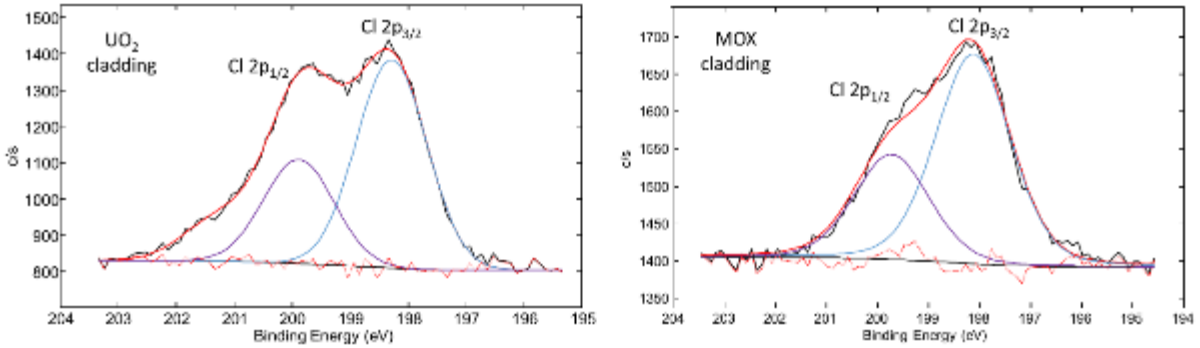

Figure 2-8: XPS narrow scans of the binding energy range of Cl $2p_{1/2}$ and Cl $2p_{3/2}$ elemental lines for the fuel-cladding interaction layers present on UO_2 (left) and MOX fuel (right) cladding.

2.3.2 XAS analyses

Figure 2-9 depicts the normalised Cl-K edge spectra for a CsCl reference compound, a sample of non-irradiated Zircaloy-4 as well as for all UO_2 and MOX fuel and cladding specimens. As shown, a clear similarity for the K-edge positions of Cl is evident for each individual spectrum. For the white lines following the edge jumps, the irradiated specimens exhibit fewer characteristic features, which could be the result of a dampening effect due to the strong reabsorption in the fuel matrix or the formation of distinct chlorine compounds, differing from CsCl or the chlorine compound in the non-irradiated material. In addition, an elevated concentration of ruthenium could be detected within both MOX specimens, resulting in the intense Ru-L_3 signals at 2838 keV featured in the spectra below.

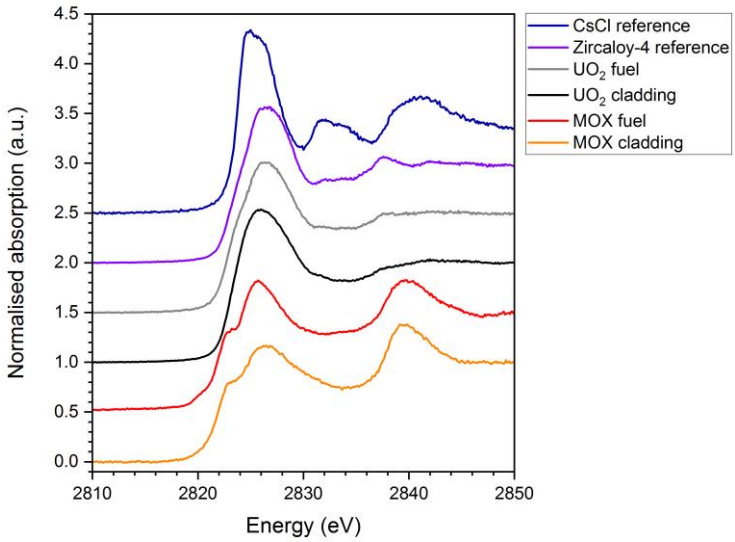

Figure 2-9: Cl-K edge spectra for UO_2 and MOX specimens as well as reference samples.

However, a change in edge structure regarding the pre-absorption edge can be seen for the irradiated specimens at 2823.6 eV. Pipon and colleagues described similar features during chlorine diffusion experiments performed with non-irradiated UO_2, in which chlorine migrated similar to iodine from the pellet centre to the peripheral parts of the pellet [40]. The differences seen between the edge structures of the cladding and fuel specimens can be explained by the amount of chlorine within the respective part of the pellet. Pipon and co-workers stated, that in case of elevated amounts of chlorine, a single signal structure would evolve, whereas in lesser-enriched parts, the signal will evolve into a double peak spectrum.

I-K edge spectra for all fuel and cladding specimens including CsI and KI reference compounds are shown in *Figure 2-10*. From the obtained data, it is conceivable, that the present iodine species formed within the fuel fragments as well as on the inner part of the cladding specimens resembles an iodide (I^-) species, e.g., crystalline CsI. The formation of CsI within nuclear fuel during reactor operation is predicted by Cubicciotti and Sanecki as well as Yaggee, Mattas and Neimark as a result of a gas phase transport process from the hot fuel centre to the colder, peripheral surface of the cladding being in contact with the primary cooling circuit itself [41,42]. In general, iodine compounds are presumed to degrade zirconium-based claddings due to the reactivity of iodine [24,43,44]. . However, the existing iodine partial pressure within the fuel-cladding interaction layer is not sufficient to initiate chemical reactions and thus stress-corrosion cracking processes due to the chemical stability of CsI as stated by Sidky as well as Ball and colleagues [16,45]. Nevertheless, a radiolytic dissociation of CsI as a result of the immense radiation field of SNF, increasing the iodine partial pressure to a threshold where a degradation of the cladding appears, could be conceivable.

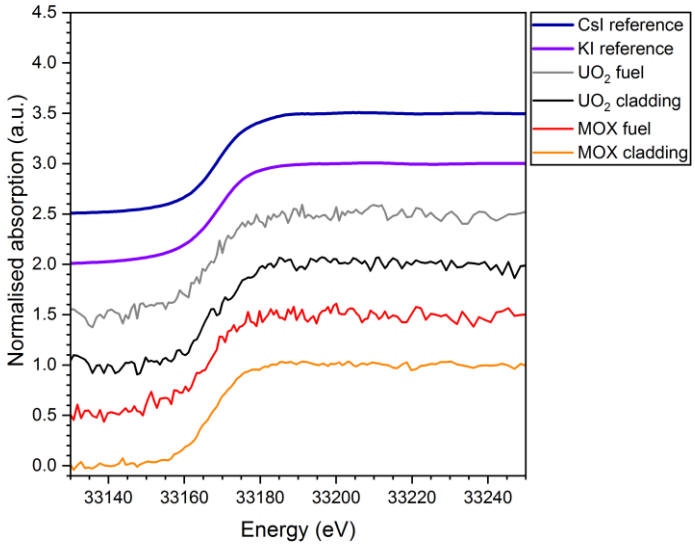

Figure 2-10: I-K edge spectra for UO_2 and MOX specimens as well as reference samples.

3. Investigation of the oxidation resistance of post pellet-cladding interaction in ZrO_2-UO_2 systems performed by CIEMAT

3.1 Introduction

The fuel-cladding interface can be described as composed of two zones, one closer to the cladding (polycrystalline ZrO_2) and a second one nearer the fuel pellet, which is mainly formed by solid solutions of $(U,Zr)O_2$ (cubic fluorite) [46]. This second layer is composed by variable relative concentrations of U and Zr [47,48].

In the framework of back-end of nuclear fuel, prior to or after the dry interim storage period, the nuclear fuel assemblies are transferred into a transfer shield unit. Dry transfer system provides an "interface between large and small casks and between storage-only and transportation casks" [49] and it can also allow fuel handling for examination and reparation [49,50]. The criteria inventories of oxidizing gases in typical storage designs with cask are accepted by NRC (Nuclear Regulatory Commission, US) to be less than 1 mole per cask (moisture less than 0.4 kPa) and an inert helium or nitrogen atmosphere for storing UO_2 spent fuel in a dry environment [51,52]. Considering possible scenarios that may take place in a dry interim storage facility, including transfer module, important variables such as time/temperature limits need further investigation to prevent Spent Nuclear Fuel (SNF) oxidation when it is exposed to an oxidizing atmosphere. In such scenario, the degradation of both, Zircaloy cladding against gross rupture, and the irradiated UO_2, needs to be fully understood for the appropriate technical support to be adopted in order to prevent release of radioactive material [53–55]. The availability of oxygen (oxidant agent) and temperatures higher than 250 °C may entail the oxidation of the fuel matrix from UO_2 (fluorite, cubic) to U_3O_8 (orthorhombic) that implies a volume increase of around 36%, which in turn may result in pulverization, spallation, splitting of the sheath and leakage of radioactive material. The oxidation of UO_2 constitutes a two-step reaction: $UO_2 \rightarrow U_4O_9/U_3O_7 \rightarrow U_3O_8$ [56]. The better-required final stabilized form for the uranium oxides should be limited to intermediate oxides U_4O_9, where fluorite structure is preserved. Although oxidation of UO_2 under different surrounding conditions, such as temperature and oxygen partial pressure, has been studied for more than five decades [57,58], some topics still remain

unclear and are not even included in fuel performance codes, like the influence of the fuel-cladding inter-diffusion zone [46,59].

Understanding the properties of the pellet-clad bonding layers is worthy of study. Specifically, the potential chemical oxidation resistance of UO_2 (matrix fuel) to U_3O_8 by the ZrO_2/Zr system, after a potential air intrusion, in case of undetected damaged cladding (zirconium alloy) or defective fuel, is relevant in terms of assessing fuel integrity covering all possible scenarios during storage. Therefore, assuming evidences on Zircaloy-fuel interaction [60–62], here we conduct characterisation of ZrO_2-doped UO_2 pellets including morphological, chemical, and crystallographic analyses. Furthermore, we present some results of the oxidation behaviour of these powdered samples under dry conditions, that prove the chemical oxidation resistance of UO_2 to U_3O_8, when it forms part of the $(U,Zr)O_2$ solid solution, trying to mimic the chemical bonding between ZrO_2 and UO_2. In this study, we investigated both individual and joint effect of temperature, oxygen partial pressure and Zr content to analyse scenarios facing matrix oxidation with competing factors [63].

3.2 Objectives

In this part of the report, we study the behaviour of the pellet-cladding interface under a potential oxygen exposure during dry storage and subsequent transportation conditions. More specifically, the ultimate goal seeks to provide empirical data on chemical oxidation resistance of UO_2 to U_3O_8 because of the interlayer bonding of urania and zirconia formed during reactor operation in LWR. The experimental programme aims (1) to synthesize and characterise in detail model materials to support SNF oxidation studies on the pellet-cladding bonding layer, *i.e.,* UO_2 ceramics doped with different ZrO_2 contents, and (2) to understand matrix oxidation of ZrO_2-doped UO_2 under a wide range of potential dry storage conditions (temperature and oxygen partial pressure).

3.3 Experiments with ZrO_2-doped UO_2 performed by CIEMAT

3.3.1 Synthesis and microstructure analysis of model materials: ZrO_2-doped UO_2 samples

At CIEMAT, a series of ZrO_2-doped and undoped UO_2 pellets (UO_2, UO_2-20 wt% ZrO_2, UO_2-40 wt% ZrO_2, UO_2-80 wt% ZrO_2 and pure ZrO_2) were manufactured by pressing mixtures of the weighted amounts of precursor oxide powder. Zirconium oxide of 99.98 % purity (Alfa Aesar) and natural uranium oxide obtained via Ammonium Di-Uranate (ADU) [64] were the powders used for preparing the samples. Oxide powders were mixed with 1 wt% of EBS (N,N'-Ethylenebisoctadecanamide) as a binder and lubricant. The pellets were fabricated by conventional ceramic processing that consisted of three sequential steps: preparation and mixing of starting materials, pelletizing (uniaxial press at 700 MPa), and sintering (1675 °C for 4 h under H_2/N_2 atmosphere on an alumina tubular furnace). This fabrication procedure is described in more detail in our earlier articles [65–67]. Once sintered, the microstructures of the sintered pellets were characterised in detail, and thereafter those pellets were manually crushed in an agate mortar before being subjected to dry oxidation experiments. These powdered samples were likewise characterised. All these solids characterisation outcomes are hereunder described.

An overview of the determined specifications and characteristics of the as-sintered ZrO_2-doped and un-doped UO_2 pellets is given in *Table 3-1*. The crystal structure of the pellets was studied by XRD (Bruker D8 Advance Eco diffractometer) at 40 kV and 25 mA using Cu Kα radiation (λ = 1.54056 Å), with a Bragg-Brentano configuration over the 2θ range of 20° - 120° and at a step size of 0.01°. The lattice parameter of each sample was calculated by a Rietveld refinement Quantitative Analysis (RQA), using the DIFFRAC.TOPAS program (Bruker Analytical X-Ray Systems), considering the Fm-3m space group (*Figure 3-2*). The bulk density of the pellet was measured by the general water immersion Archimedes method (Sartorius kit) and was calculated from the weight and dimensions of the pellet. The density values were calculated using mean plus one standard deviation (± 1σ), on a number of measurements (between four and twelve). The average bulk density decreased from the un-doped UO_2 pellet (9.1 $g \cdot cm^{-3}$) with increasing ZrO_2 content in the UO_2 sintered pellets, as expected.

The morphology of the pellets surface was examined by Scanning Electron Microscopy (SEM) (TM4000 Plus, HITACHI), revealing a non-homogeneous grain structure (*Figure 3-1*). As the composition becomes richer in ZrO_2, small grains located between the matrix grains start to appear, probably due to ZrO_2-rich particles [68] and once the solubility of ZrO_2 in cubic UO_2 is achieved (*Figure 3-1*).

Table 3-1: Lattice parameters of the undoped UO_2 and as-sintered ZrO_2 doped pellets.

SAMPLE	**a)** **UO_2** **#476**	**b)** **20 wt% ZrO_2 -UO_2** **#629**	**c)** **40 wt% ZrO_2 -UO_2** **#631**	**d)** **80 wt% ZrO_2 -UO_2** **#757**	**e)** **100 wt% ZrO_2**
Lattice param. (nm)	100% UO_2 *Fm-3m* a=b=c= 0.5470(2)	92% $U_{1-y}Zr_yO_2$ (y = 0.48) *Fm-3m* a=b=c= 0.5403 (1) < 8% t-ZrO_2 SG P *42/nmc* a=0.3686(2) b=0.3686(2) c=0.5138(3)	67% $U_{0.5}Zr_{0.5}O_2$ *Fm-3m* a=b=c= 0.5404(1) 33% t-ZrO_2 SG P *42/nmc* a=0.3688(4) b=0.3688(4) c=0.5150(1)	91% $U_{1-x}Zr_xO_2$ (x = 0.04) *P1 21/c1* a=0.5161(2); b=0.5214 (2); c=0.5324(2) 44% t-ZrO_2 SG P *42/nmc* a=0.3660; b=0.3660; c= 0.5206 (8) ~3% $U_{1-y}Zr_yO_2$ (y = 0.5) *Fm-3m* a=b=c=0.5461(9) 2% UO_2 *Fm-3m* a=b=c=0.5471(2)	100% m-ZrO_2 *P1 21/c1* a=0.5156(3) b=0.5211(1) c=0.5324(7)
Density immersion ($g \cdot cm^{-3}$)	9.1 ± 0.1	8.6 ± 0.1	8.1 ± 0.1	6.1 ± 0.6	5.5 ± 0.3

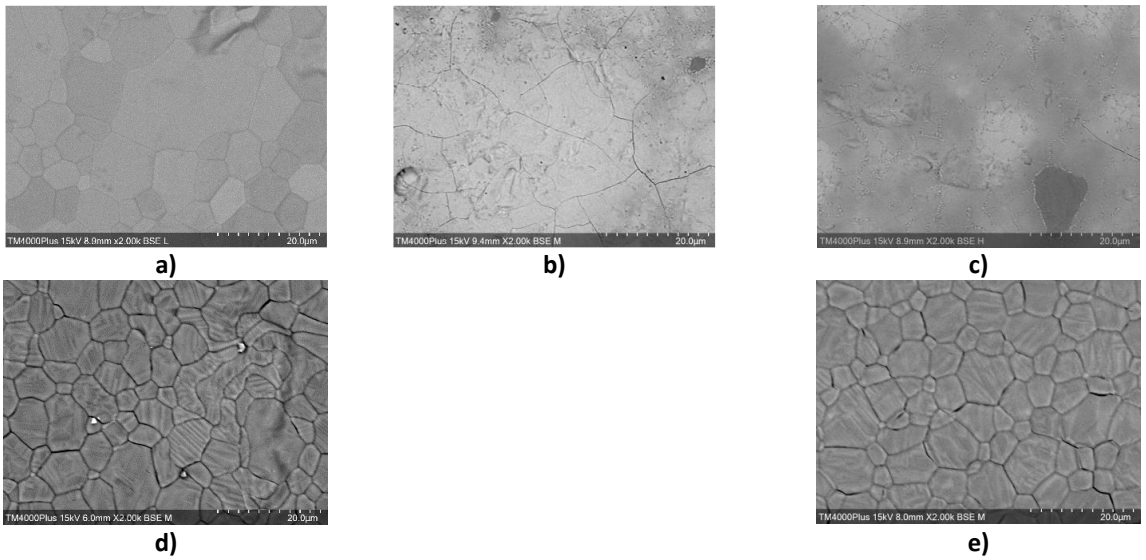

Figure 3-1: SEM images of the prepared samples: a) UO_2, b) 20 wt% ZrO_2 -UO_2, c) 40 wt% ZrO_2 -UO_2, d) 80 wt% ZrO_2 -UO_2 and e) 100 wt% ZrO_2.

The XRD patterns of the ZrO_2-doped and undoped UO_2 and ZrO_2 sintered pellets (*Figure 3-2*) show that the main peak positions shift to higher angles with increasing ZrO_2 content up to 40 wt% of ZrO_2, indicating that the lattice contracts when Zr(IV) is incorporated into the UO_2 lattice substituting the U(IV) atoms as stated in the literature [69]. Beyond this mixture composition, the cubic fluorite structure is lost and the existence of polymorphic forms of pure ZrO_2 is observed, whose main phases are found in the form of tetragonal and monoclinic. Pure ZrO_2 under atmospheric pressure shows three thermodynamically stable polymorphs in relation to the temperature: monoclinic (m-ZrO_2), tetragonal (t-ZrO_2) and cubic (c-ZrO_2) structures [68,70,71]. Generally, m-ZrO_2 is the stable form of ZrO_2 at low temperature [68,71]. Around 1173 ˚C, there is a transition to a tetragonal structure [71] that exists up to around 2300 ˚C [70,71]. Then, there is a controversy about the existence of the c- ZrO_2 allotropic form at a temperature greater than 2370 °C [72], or whether it could reach its melting temperature (around 2700 ˚C) [71].

Based on the XRD analysis, incorporation of UO_2 into the ZrO_2 structure might be the reason for the transformation of monoclinic ZrO_2 to its tetragonal polymorph. Urania-zirconia solid solution have been previously studied by Cohen *et al.* [68], who prepared a range of (U,Zr)O_2 solid solutions by dry powder route at 1725-1750 ˚C in H_2(g) for 72-110 h. They observed the following: (i) below 1660 ˚C there is a "miscibility gap" with a sharp decrease of the ZrO_2 solubility in UO_2; (ii) a two-phase region of cubic and tetragonal at 1600-2300 ˚C. At 1690 ˚C, the solubility limit is in the range of 30 – 60 wt% ZrO_2, however it is around 30 wt% ZrO_2 at 1875 ˚C; (iii) stabilization of a cubic solid solution in the temperature range 2366 to 2556 ˚C. According to these data and under our sintering conditions, a conservative estimate for the solubility limit would therefore be around 30 – 60 wt% ZrO_2.

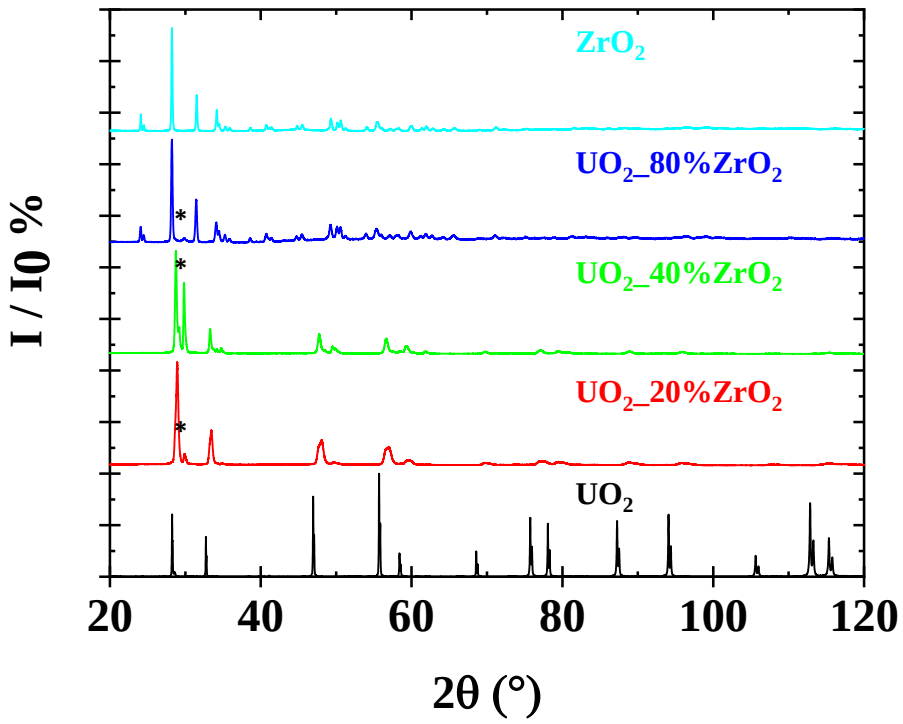

Figure 3-2: XRD patterns of the sintered pellets: UO_2, 20 wt% ZrO_2 -UO_2, 40 wt% ZrO_2 -UO_2, 80 wt% ZrO_2 -UO_2, ZrO_2.

As already mentioned, prior to the dry oxidation experiments in the thermogravimetric analyser, samples were prepared by manually milling in an agate mortar a replica of the sintered pellets for each Zr composition (see an example in *Figure 3-3*).

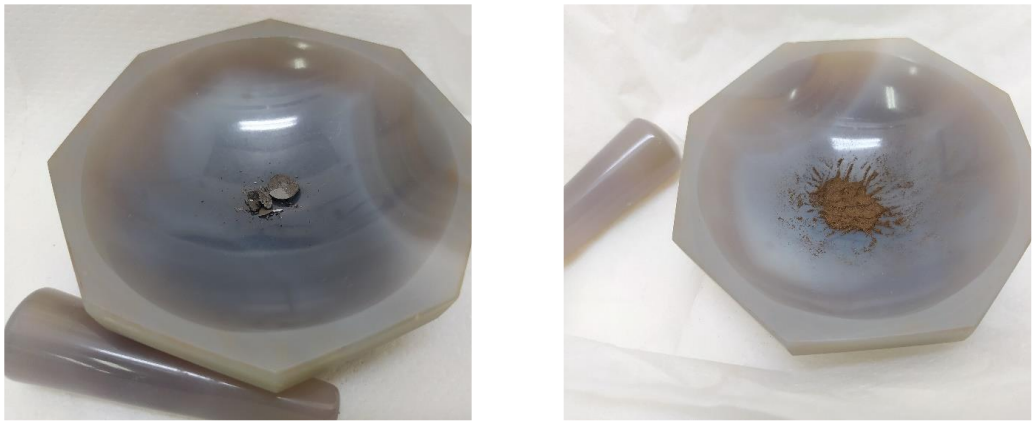

Figure 3-3: The 40 wt% ZrO_2 -UO_2 sintered pellet before (a) and after (b) being manually milled in an agate mortar prior to thermobalance oxidation.

The obtained powder of ground pellets obtained was also analysed by XRD (diffractograms are not shown). XRD patterns of pellets crushed into powders were found similar when compared to those obtained on the pellets. Raman spectroscopy analysis was carried out on sample powders with a LabRAM HR Evolution spectrometer (Horiba Jobin Yvon Technology) provided with a He-Ne laser (λ=632.8 nm) and Olympus BX41 microscope. Raman spectra were recorded at room temperature with the 50x objective, using a power of 1 mW (5% nominal power filter) and an acquisition time of 150 s in the 50–2200 cm^{-1} range. Acquired spectra were re-calibrated by using the emission lines of a Ne arc-lamp. Typically, 10 spectra were acquired and summed for each sample.

Figure 3-4 shows the Raman spectra of the as-prepared powdered ZrO_2-doped and undoped UO_2 samples. Raman spectrum of undoped UO_2 shows the typical profile of a fluorite structure. The main T_{2g} band, assigned to the U-O symmetric stretching mode [66], is centred at ~445 cm^{-1}, and the second-order longitudinal optical mode (2LO) at ~1150 cm^{-1} [73]. Additionally, the longitudinal optical mode (LO) centred at 570 cm^{-1}, associated with a reduced symmetry of the cubic fluorite lattice structure and interpreted as a “defects band” can also be observed [74,75]. As the theoretical U/Zr ratio decreases, it induces changes in the Raman spectra, such as the T_{2g}, LO and 2LO bands broadening and their shift towards higher wavenumber (up to 40 wt% ZrO_2), what indicates that Zr has been incorporated into the UO_2 lattice, and an increase of local disorder is taking place [76]. Conversely, for the sample doped with 80 wt% ZrO_2 several peaks centred at 183, 301, 335, 381, 476, 536, 559, 613, and 636 cm^{-1} appear, which correspond to a dominant monoclinic phase of ZrO_2 [12].

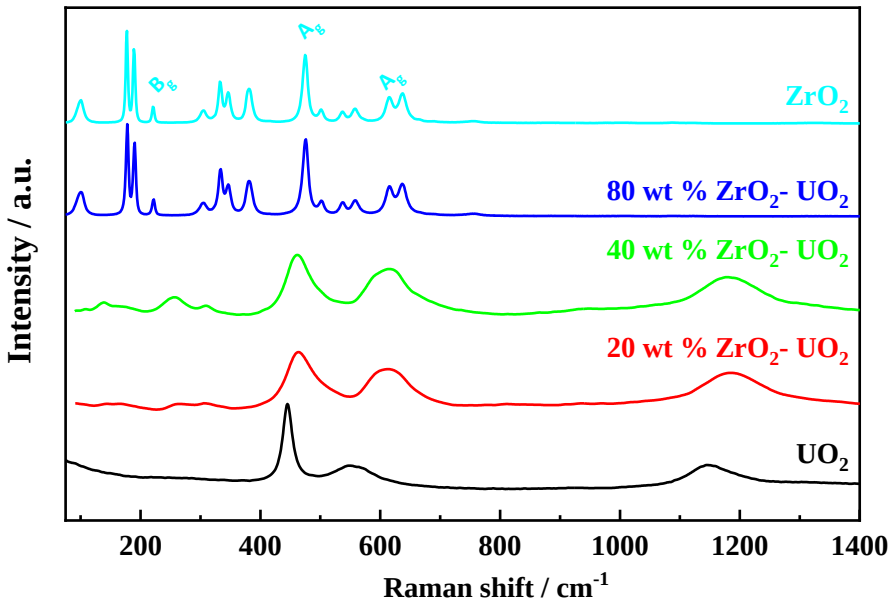

Figure 3-4: Normalized Raman spectra of powdered samples prior to the oxidative treatments: UO_2, 20 wt% ZrO_2 -UO_2, 40 wt% ZrO_2 -UO_2, 80 wt% ZrO_2 -UO_2, ZrO_2.

3.3.2 Dry oxidation experiments of ZrO_2-doped UO_2

In order to study the influence of the ZrO_2 amount present in UO_2 and the O_2 concentration on the oxidation kinetics behaviour, the prepared and ground samples of ZrO_2-doped UO_2 were tested by thermogravimetric analysis (TGA). A TGA Q50 thermobalance (TA Instruments) was used under an O_2/N_2 flow rate of 60 mL min^{-1}. The TGA calibration was performed in both, temperature of magnetic standards (Curie point, ASTM E−1582) with Alumel, Ni and $Ni_{0.63}Co_{0.37}$ alloy standards (154.16 ± 0.31, 358 ± 1.1 and 764.4±1.6 °C, respectively), and weight (200 mg to 1 g calibration weight range). Different O_2/N_2 gas mixtures were used in thermal treatments: synthetic air 20% O_2 – 80% N_2 (named as 21% O_2); and low oxygen availability using 1% O_2–99% N_2 (from now on referred as 1% O_2), both supplied by Air Liquide.

Oxidations were conducted under non-isothermal and isothermal conditions (*Figure 3-5*) by heating the powdered samples in an open platinum crucible. For non-isothermal experiments samples were heated from room temperature up to 900 °C at a linear rate of 10 °C·min^{-1} under both, 21% vol O_2 and 1% vol O_2, to obtain the complete conversion to U_3O_8 and then, to study the overall reaction. Isothermal experiments consisted of different stages: in the first stage, the samples were stabilized during 10 min (1) and heated to the temperature of interest (200, 300 and 400 °C) at 10 °C·min^{-1} both in N_2 (2). Then, after being the reaction temperature maintained during 10 min in N_2 (3), a mixture of O_2/N_2 was introduced into the balance at a constant gas flow rate of 60 mL·min^{-1} (4) and the target temperature was kept throughout the experiments up to 10 h (5). Thermogravimetric curves were analysed by using the Universal Analysis software (TA Instruments).

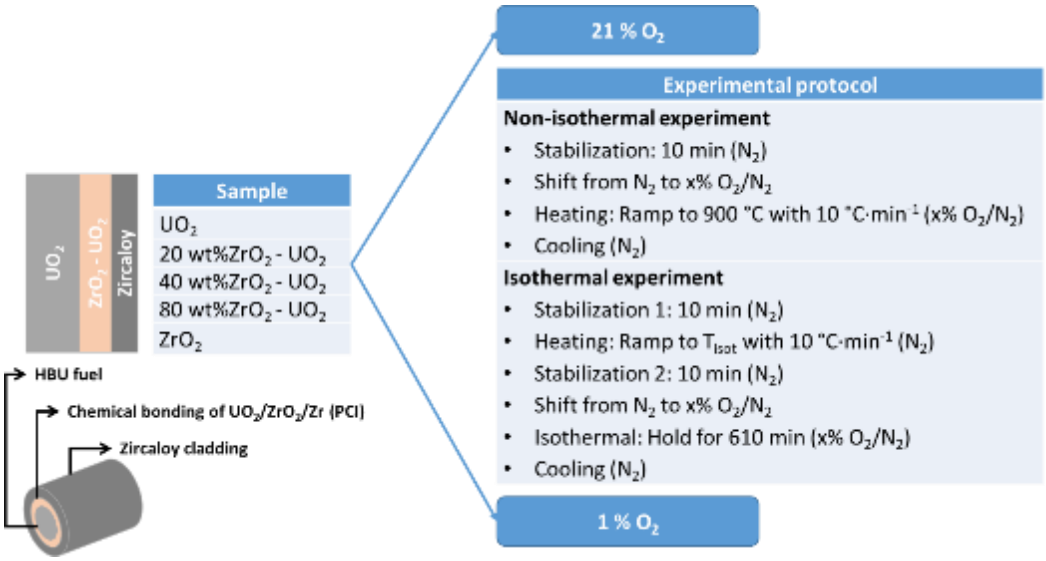

Figure 3-5: Schematic representation of the oxidation tests under non-isothermal and isothermal conditions performed on: UO_2, 20 wt% ZrO_2 -UO_2, 40 wt% ZrO_2 -UO_2, 80 wt% ZrO_2 -UO_2, ZrO_2.

3.3.3 Results and discussions of oxidation experiments performed with ZrO_2-doped UO_2

To understand the effect of different ZrO_2 loading on the formation of U_3O_8, an *in-situ* analysis of the oxidation reaction performed by TGA on ZrO_2-doped UO_2 samples containing a range of Zr concentrations is presented under non-isothermal (*Figure 3-6*) and isothermal conditions (*Figure 3-11*), both under different oxygen partial pressure. In between the measurements, the samples were stored at room conditions. Complete oxidation TGA measurements were performed in triplicate to include uncertainties (standard deviations) of all mean values of the total weight change (%), oxidation onset temperatures (OOTs), maximum reaction temperatures (MRTs), and reaction rate at the maximum reaction temperature (RR_{MRT}), in addition to ensuring the repeatability and reliability of the TGA results [64,77,78]. Additionally, pure UO_2 powder was evaluated and used as a reference.

3.3.3.1 Oxidation behaviour of ZrO_2-doped UO_2: non-isothermal (21% O_2 and 1% O_2)

The *in-situ* oxidation TGA measurements from UO_2 to U_3O_8 were performed in triplicate at 10 ˚C·min^{-1} from room temperature up to 900 ˚C under two oxygen concentrations to compare the effects of Zr doping levels and O_2 % on the thermal oxidation of UO_2. The weight increase and derivative weight (or weight gain rate) measured by TGA for the five U-Zr mixed oxides samples in 21% O_2 –N_2 and 1% O_2 - N_2 are plotted in *Figure 3-6*a and *Figure 3-6*c, and *Figure 3-6*b and *Figure 3-6*d, correspondingly. As shown in *Figure 3-6*a and c, no significant weight gain was observed in pure ZrO_2 as expected; therefore, derivative weight curves have not been calculated. These results show significant differences on the oxidation behavior for studied ZrO_2-doped UO_2 vs. Zr content (0-100%) at the same O_2 %. On the one hand, increasing Zr content seems to slow the mean oxidation's degree and rates. On the other hand, the higher the O_2 %, the higher the oxidation degree at the same ZrO_2 content on the sample.

Between 350 and 600 °C, the derivative weight signal under 1% O_2 displays a broader oxidation peak than 21% O_2, indicating a slower reaction rate. The calculated values from the TGA curves, *i.e.,* total weight change (%), OOTs, MRTs and RRM_{RT}, with their deviations, described as a percentage weight change are shown in *Figure 3-6*. Errors represent ± 1σ from triplicate samples.

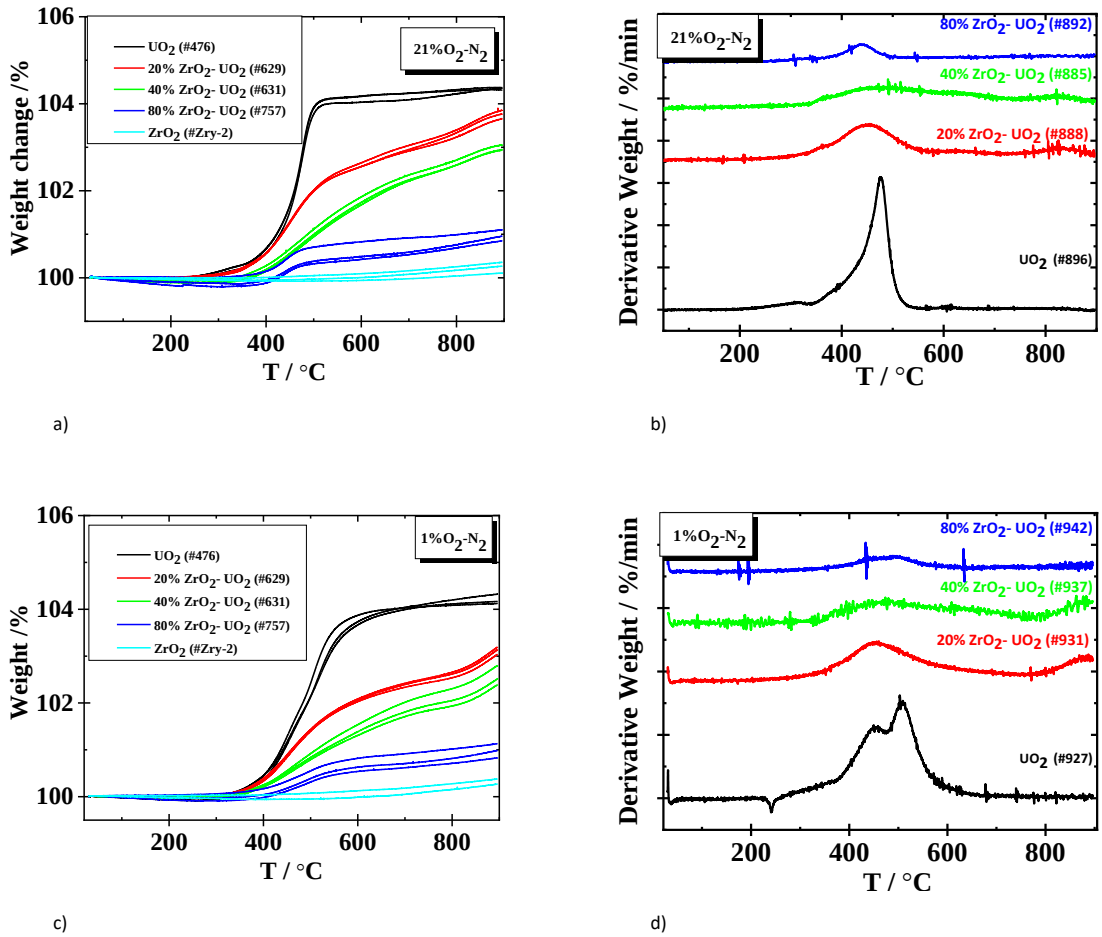

Figure 3-6: Weight change curves at 21%O_2 (a) and 1%O_2 (c), and reaction rates at 21%O_2 (b) and 1%O_2 (d) of: UO_2, 20 wt% ZrO_2 -UO_2, 40 wt% ZrO_2 -UO_2, 80 wt% ZrO_2 -UO_2, ZrO_2.

Total weight change at 900 ˚C (*Figure 3-7*a) evidences a dependence on Zr content. The change in weight decreased with additional loading of ZrO_2. After an oxygen concentration resembling 40 wt% ZrO_2, no effect of either 21% or 1% O_2 was evident. Then, the differences in weight increase are negligible as a function of O_2%. These results reveal an apparently enhanced thermal stability effect of ZrO_2 on UO_2 matrix, which is most likely attributed to the chemical stability of zirconia to high temperatures and under strong oxidative environments. It should be noted that from 80 wt% ZrO_2, changes in the oxidizing agent concentration have a negligible effect on the thermal oxidative stability of UO_2 matrix; this interesting phenomenon could be attributed to the decreased solubility of UO_2 in tetragonal and monoclinic ZrO_2, respectively [68].

The OOT (*Figure 3-7*b) is a relative quantity of the resistance of a substance to oxidative degradation. UO_2 starts oxidizing at about 250 °C, and degrades in two steps with a small and then a large peak in both atmospheres. The first peak corresponds to the thermal transition from UO_2 to U_4O_9/U_3O_7 and the second starting at about 350 °C to the conversion to U_3O_8 [64]. Loading with 20 and 40 wt% ZrO_2 results in significant changes. As proved by the first derivative curve of the weight gain (*Figure 3-6*b and *Figure 3-6*d), the reaction proceeds in one single step. Additionally, delayed initial oxidation temperature (OOT) from ~400 ˚C to ~370 and 360 ˚C, respectively, was observed (*Figure 3-7*b). With incorporation of 80 wt% ZrO_2 into UO_2, the OTT value increased to ~390 °C.

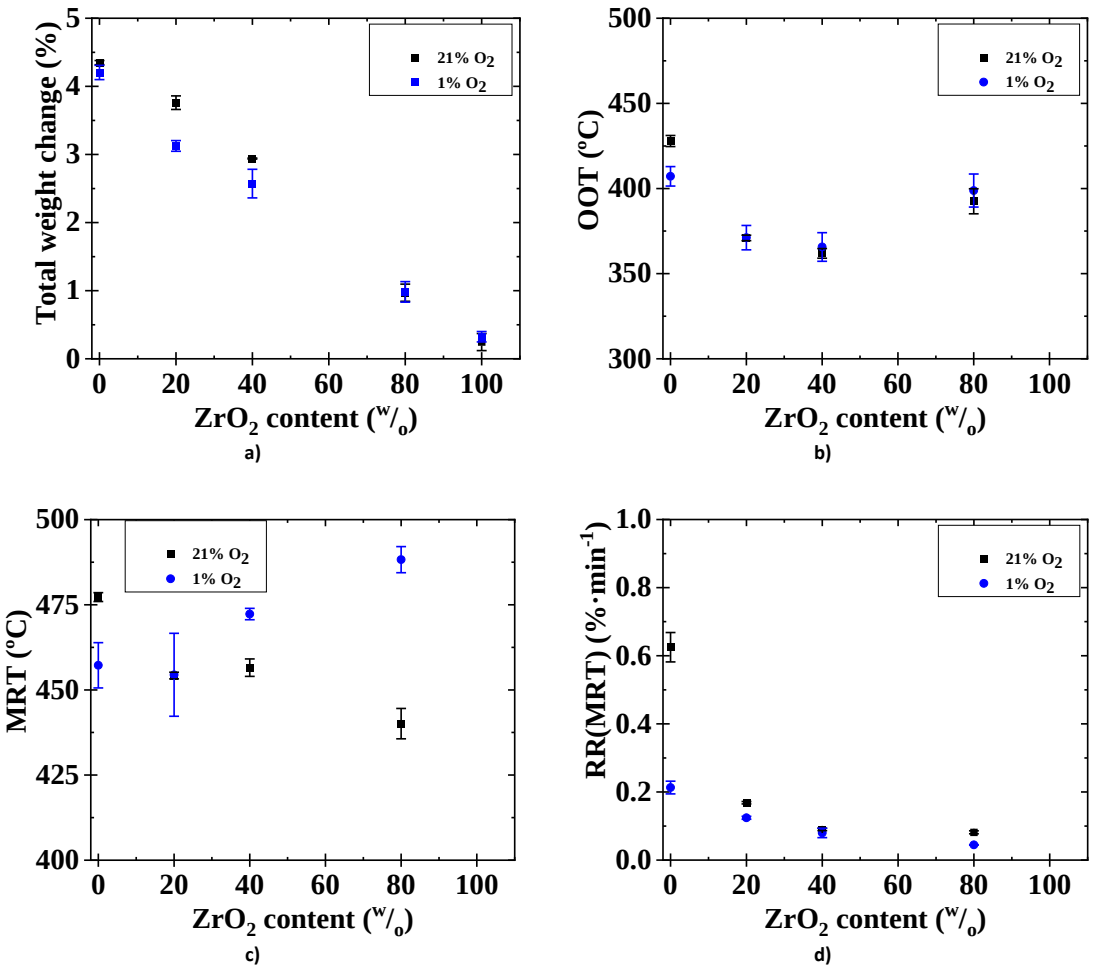

Figure 3-7: Total weight change at 900 ˚C (a), OOT (b), MRT (c) and RR (MRT) (d) using two O_2 contents (21% and 1% O_2) of: UO_2, 20 wt% ZrO_2 -UO_2, 40 wt% ZrO_2 -UO_2, 80 wt% ZrO_2 -UO_2, ZrO_2.

The MRT and RR_{MRT} of the second oxidation stage (*Figure 3-7*c and d) were calculated using the first derivatives of the weight variation curves (% min^{-1}) [77] from *Figure 3-6*b and *Figure 3-6*d. In general, the higher the initial ZrO_2 content in the sample, the lower the total weight change. The same decreasing trend as a function of ZrO_2 content is observed for the OOT and RR_{MRT} values at both O_2 %. However, the MRT values result in the opposite: they decrease with Zr content at 21% O_2 while they seem to increase at 1% O_2 from 20 wt% ZrO_2. The observed OOT for the last sample (corresponding to 80 wt% ZrO_2) breaks the trend probably as a consequence of the already pointed out decreased solubility of UO_2 in tetragonal and monoclinic ZrO_2 [68], which may induce segregated UO_2. The relatively low uncertainties associated to the OOT demonstrate reliability [79].

All the oxidized ZrO_2-doped UO_2 samples have been characterised by Raman spectroscopy, XRD and SEM. Regarding Raman spectroscopy, the corresponding acquired spectra are included in *Figure 3-8*. A similar trend is observed independently of the atmosphere used (1% O_2 and 21% O_2). On the one hand, the oxidized UO_2 sample has been completely transformed to the orthorhombic U_3O_8 phase. This is confirmed by the Raman features obtained, characteristic of U_3O_8 (see asterisks in *Figure 3-8*): a broad and intense contribution in the 300-500 cm^{-1} region, and three significant bands at around 120, 240 and 810 cm^{-1} [80–84]. The same behaviour is observed for the segregated UO_2 present in the 80 wt% ZrO_2 sample, while, as expected, its greater proportion of ZrO_2 (predominant in *Figure 3-4*) has not been altered by the thermal treatment (corresponding Raman spectra not shown). On the other hand, the 20 wt% and 40 wt% ZrO_2 samples, although likewise converted to U_3O_8, seem to contain ZrO_2 within its structure. This can be assumed taking into account the additional peaks (at around 290, 610, 660

and 770 cm^{-1}) observed in these samples when compared to the "pure" U_3O_8. In fact, the incorporated ZrO_2 might be present in its tetragonal form, given that the positions of some of the latter extra peaks (especially the one at around 610 cm^{-1}) are quite in accordance with the reported values for such a t-ZrO_2 phase [85,86]. Another remarkable feature that corroborates the presence of ZrO_2 within the UO_2 lattice is the increase in intensity suffered by the band located at ~770 cm^{-1} in these two samples, which is almost negligible in the "pure" U_3O_8. If there was segregated m-ZrO_2 (monoclinic), its most intense bands (at about 180, 335, and 476 cm^{-1}) should be noticeable in the Raman spectrum.

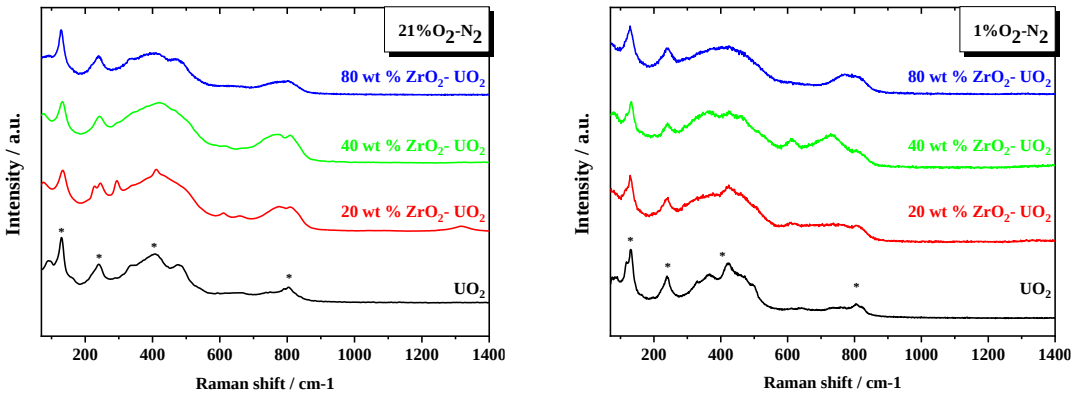

Figure 3-8: Raman spectra of oxidized UO_2, 20 wt% ZrO_2 -UO_2, 40 wt% ZrO_2 -UO_2 and 80 wt% ZrO_2 -UO_2 up to 900 °C at 21% O_2 (a) and 1% O_2 (b).

Figure 3-9 shows the change in the diffractograms during the oxidation of UO_2 and of ZrO_2-doped UO_2 samples into U_3O_8 at temperatures up to 900 °C in atmospheric air. The RQA from XRD measurements performed on the ZrO_2-doped UO_2 samples oxidized at non-isothermal conditions is still undergoing to calculate the weight fraction of all crystalline U-oxides present.

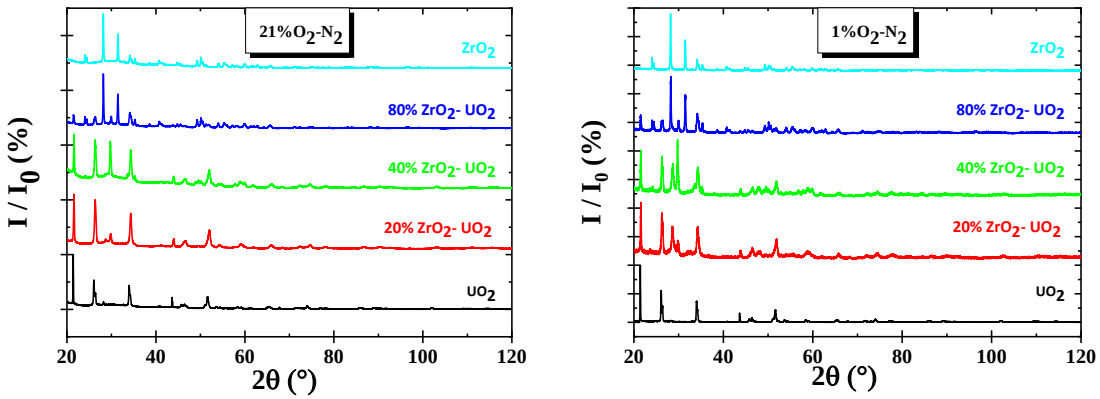

Figure 3-9: XRD patterns of oxidized UO_2, 20 wt% ZrO_2 -UO_2, 40 wt% ZrO_2 -UO_2 and 80 wt% ZrO_2 -UO_2 at 21% O_2 (a) and 1% O_2 (b) up to 900 °C.

As observed in the XRD patterns, the pure UO_2 is completely oxidized to U_3O_8 under air, and almost fully oxidized to U_3O_8 in 1% O_2. Increased loadings of ZrO_2 lead to lower U_3O_8 intensities for both atmospheres used. However, even being the U_3O_8 phase prevalent, with the lowest oxygen partial pressure used, it is possible to observe intermediate oxidized phases of Uranium for the 20 wt% and 40 wt% ZrO_2 samples. These results, are in agreement with our previous published studies by Milena *et al.* [87] using Cr_2O_3-doped UO_2 samples oxidized up to 700 ˚C under 21% and 1% O_2, who by using XRD observed the presence of U_3O_7 and U_3O_8. Tetragonal zirconia phase vs monoclinic-ZrO_2 is stabilized by

the presence of UO_2 (maybe as a solid solution) up to solubility limit (~40 wt%), compared to the monoclinic zirconia. Raman spectroscopy also confirm this observation (*Figure 3-8*).

Figure 3-10 shows SEM-EDX images of the powders obtained by oxidizing the *ZrO_2-doped UO_2* samples (only shown at 20 and 80 wt%) at 900 ˚C and in air. During the oxidation, the initial small fragments were partially pulverized to the product of oxidation U_3O_8 because of the aforementioned increase in the lattice volume. This U_3O_8 powder presents typically popcorn-like morphology, and visible cracks were developed on the surface. Additionally, initial particles appear surrounded by columnar-shaped fines of U_3O_8. Cracked surface induces material spallation [88]. Energy dispersive X-ray spectroscopy (EDX) mapping confirms the presence of uranium, oxygen and zirconium on the surface for the oxidized materials. The EDX mapping of the oxidized sample with 80 wt% of ZrO_2 reveals that some segregation of zirconium oxides has occurred (*Figure 3-10*b). The large ZrO_2-rich regions in the EDX map of the *80 wt% ZrO_2 -UO_2* are visible also in the SEM image, due to the difference in morphology between the U_3O_8 and ZrO_2. In contrast, after oxidation reaction, the Zr-rich particles of the *20 wt% ZrO_2 -UO_2* material cannot be observed in the SEM image (*Figure 3-10*a) and it appears to exhibit a more significant U_3O_8 growth compared to the *80 wt% ZrO_2 -UO_2* sample. This corroborates the assumption of ZrO_2 containment within the U_3O_8 structure in the case of *20 wt% ZrO_2 -UO_2*, previously considered from Raman spectroscopy results.

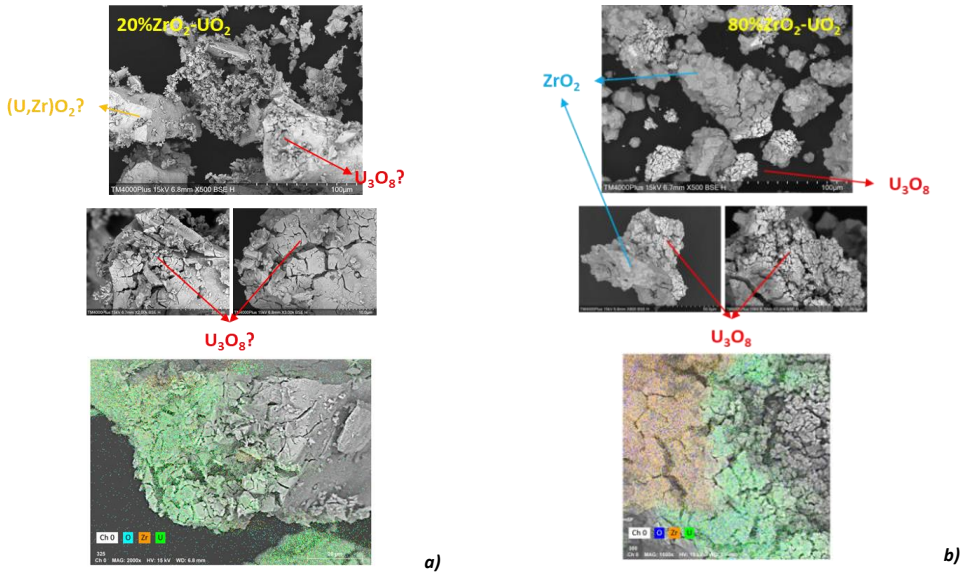

Figure 3-10: SEM micrographs of oxidized 20 wt% ZrO_2 -UO_2 (a) and 80 wt% ZrO_2 -UO_2 (b) at 21% O_2 under non-isothermal conditions up to 900 °C.

3.3.3.2 Oxidation behaviour of ZrO_2-doped UO_2: isothermal (21% O_2 and 1% O_2)

The weight gain of ZrO_2-doped and undoped UO_2 samples (powder) during the isothermal oxidation was measured continuously by TGA at 200, 300 and 400 ˚C under air and 1% O_2 (*Figure 3-11*). At 200 °C after 10 h of exposure to the oxidant agent, the weight increase is below 0.5 % for all the materials and oxygen concentration in the gas phase (*Table 3-2*). This means that the oxygen partial pressure at this temperature has a negligible effect on the oxidation degree. After an increase of 100 ˚C, *i.e.,* 300 ˚C, a sigmoid shape of the weight gain curves measured during isothermal oxidation is observed [57,82,89–95]. This temperature-dependent behaviour is interpreted as two different mechanisms: 1) nucleation and growth [96]; and 2) fresh reactive surface formed after an “incubation time” or “induction period” associated with a “critical layer thickness” of UO_{2+x} and/or U_4O_9 /U_3O_7 [57,88]. Similar sigmoidal curves have also been obtained at 400 ˚C for both oxygen contents. The oxidation of UO_2 to U_3O_8 at 400 ˚C in air and 1% O_2 is completed; however, this behaviour is different depending on the Zr content, as total conversion to U_3O_8 is not reached. At both, 300 and 400 ˚C, increasing Zr content

decreases the mean oxidation degree. The effect of tetravalent dopants in the oxidation of UO_2 has been previously studied, specially focused on plutonium, thorium and cerium [97–102]. According to the observations inferred from the reviewed literature, resistance to complete oxidation in the second step of the reaction ($U_4O_9/U_3O_7 \rightarrow U_3O_8$) was observed for those tetravalent dopants and the intermediate cubic phase U_4O_9/U_3O_7 is stabilised. The case of Ce is singular because it can exist in both oxidation states, i.e., as Ce(IV) and Ce(III), with the later inducing charge balancing and oxygen vacancies, resulting in non-stoichiometry. Nevertheless, an increase of Ce content has been shown to prevent the formation of U_3O_8 and consequently a reduction of the oxidation rate. Similar results were obtained here using Zr.

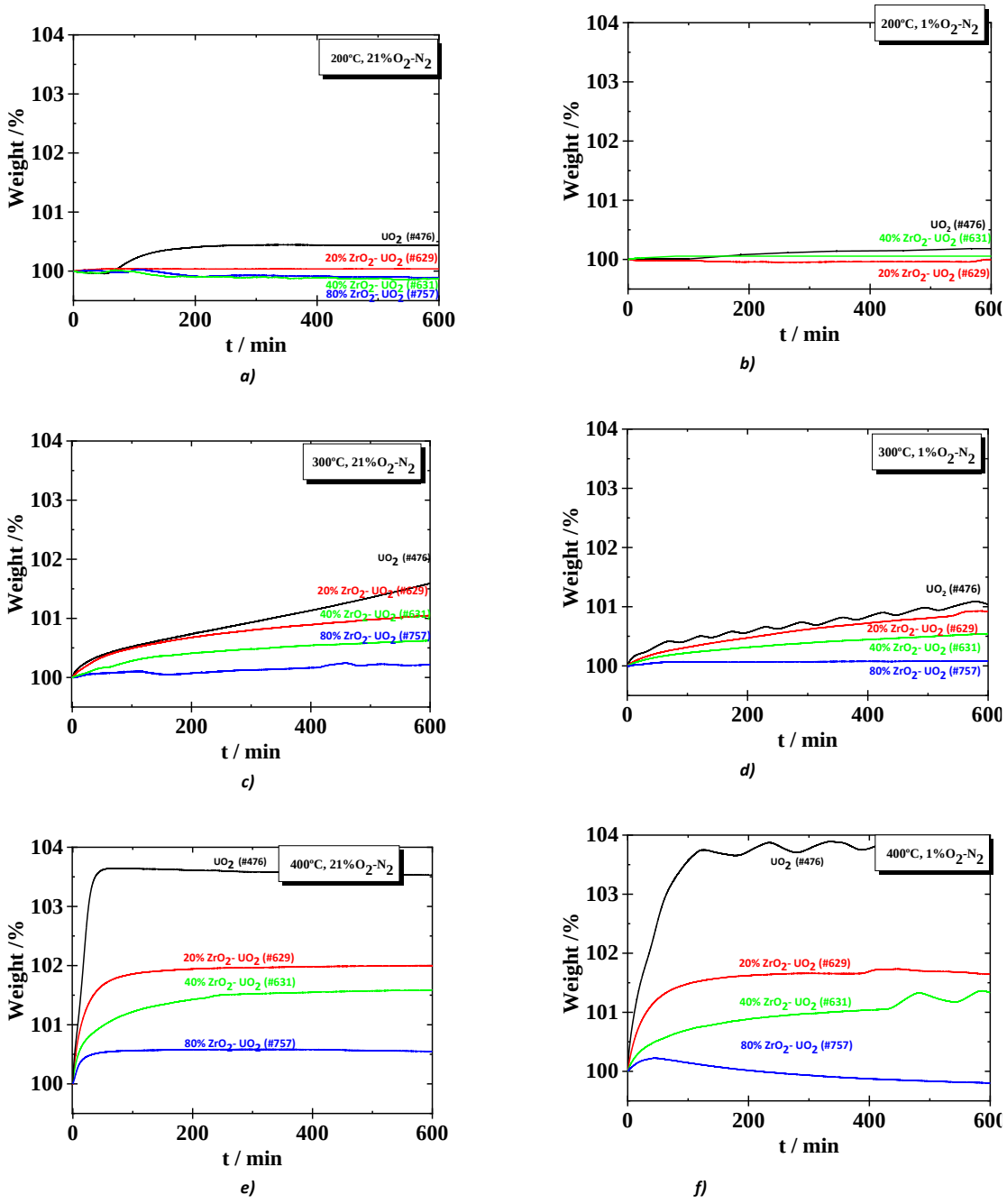

Figure 3-11: Weight change curves at 21% O2 (a, c, e) and 1% O_2 (b, d, f) under isothermal conditions at 200 ˚C (a,b), 300 ˚C (c,d) and 400 ˚C (e,f) during 10 h of: UO_2, 20 wt% ZrO_2 -UO_2, 40 wt% ZrO_2 -UO_2, 80 wt% ZrO_2 -UO_2.

The results showed in *Table 3-2* indicate that the presence of a higher oxygen concentration in the gas phase seems to enhance slightly the oxidation degree on average in the ZrO_2-doped samples and relating the same Zr content as compared to lower oxidizing conditions (1% O_2). We found that temperature and Zr content are the most important effects on the fresh UO_2 oxidation.

Table 3-2: Weight gain data (± 0.001) for the isothermal oxidation at 200 ˚C, 300 ˚C and 400 ˚C of each studied material at 21% O_2 and at 1% O_2 during 10 h.

Weight gain (%)		UO_2	20 wt% ZrO_2 -UO_2	40 wt% ZrO_2 -UO_2	80 wt% ZrO_2 -UO_2
21%O_2	200 ˚C	0.434	0.039	0	0
	300 ˚C	1.616	1.059	0.924	0.224
	400 ˚C	3.525	2.001	1.913	0.532
1%O_2	200 ˚C	0.183	0	0.055	
	300 ˚C	1.048	0.906	0.548	0.083
	400 ˚C	3.780	1.638	1.306	0.200

Also in this case, the isothermally oxidized at 300 °C ZrO_2-doped UO_2 samples have been characterised by Raman spectroscopy. *Figure 3-12* shows the Raman spectra obtained on the 20 wt% and 40 wt% ZrO_2 samples only, since those of UO_2 an 80 wt% ZrO_2 (the 20 wt% UO_2 proportion) correspond to "pure" U_3O_8 (*i.e.,* there is no difference with the non-isothermal treatment). Again, a similar trend is observed independently of the atmosphere used (1% O_2 and 21% O_2). The detected Raman features are the same for the 20 wt% and 40 wt% ZrO_2 samples. As a matter of fact, most of these features (marked with an asterisk in *Figure 3-12*) can be related to the intermediate U_4O_9 phase [103]: two peaks located at ~160 and 240 cm^{-1}, a broadened and shifted T_{2g} band (at ~460 cm^{-1}), and an intense and broad band at around 630 cm^{-1}. Moreover, the detection of an additional band at ~610 cm^{-1}, associated with the presence of a ZrO_8 type-complex in the UO_2 cubic lattice [104], indicates that these U_4O_9 oxides still contain ZrO_2 within their structure. These outcomes suggest that the incorporation of ZrO_2 into the UO_2 lattice, which has been observed to occur at least up to 40 wt% ZrO_2-UO_2, seems to stabilize the intermediate U_4O_9 phase, therefore hindering the formation of U_3O_8.

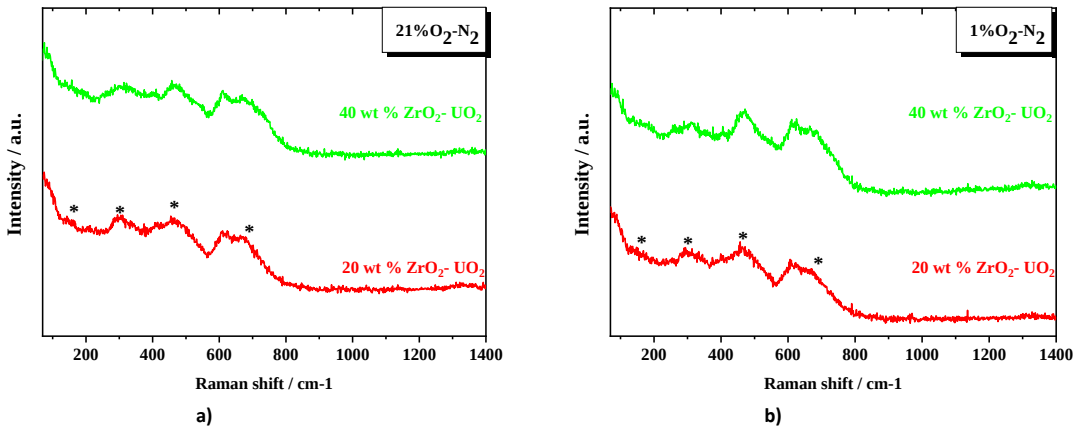

Figure 3-12: Raman spectra of oxidized 20 wt% ZrO_2 -UO_2 and 40 wt% ZrO_2 -UO_2, under 21% O_2 (a) and 1% O_2 (b) at 300 °C. (*) related to the intermediate U_4O_9 phase.

Figure 3-13 shows the diffraction patterns of the isothermally oxidized at 300 °C ZrO_2-doped UO_2 samples during 10h under 21% O_2 (*Figure 3-13*a) and 1% O_2 (*Figure 3-13*b). At intermediate temperatures, *i.e.,* 300 °C, the conversion to U_3O_8 for pure UO_2 is not complete. The intermediate U oxidized phases are distinguishable after 10h of isothermal treatment in all the cases. Also, the hyper-stoichiometric UO_{2+x} (Fm-3m) is present in 21% and 1%O_2. The tetragonal zirconia (t-ZrO_2) and solid solution $(U,Zr)O_2$ with a range of stoichiometries were identified, also confirmed by Raman.

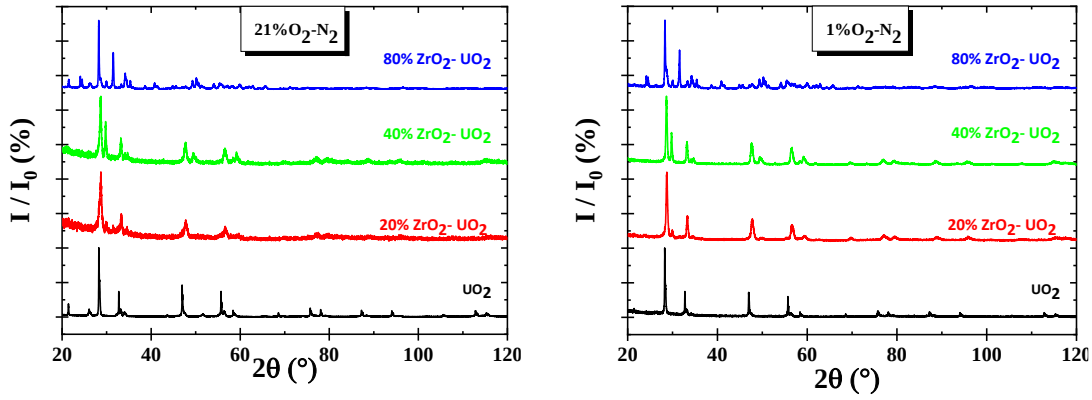

Figure 3-13: XRD patterns of oxidized UO_2, 20 wt% ZrO_2 -UO_2, 40 wt% ZrO_2 -UO_2 and 80 wt% ZrO_2 -UO_2 at 21% O_2 (a) and 1% O_2 (b) at 300 °C during 10 h.

The RQA from XRD measurements performed on the ZrO_2-doped UO_2 samples oxidized at isothermal conditions is still being evaluated. *Figure 3-14* shows an example of SEM images and EDX analyses of the oxidized 20 wt% ZrO_2 (a) and 80 wt% ZrO_2 (b) doped UO_2 powders after the 300 ˚C treatment under air. The U_3O_8 spallation particles are only observed for the sample doped with 80 wt% ZrO_2 and cracked surface is clearly shown on the micrograph. This means that transformation to U_3O_8 has been hindered in the 20 wt% ZrO_2 sample. These results are in good agreement with those obtained by Raman spectroscopy.

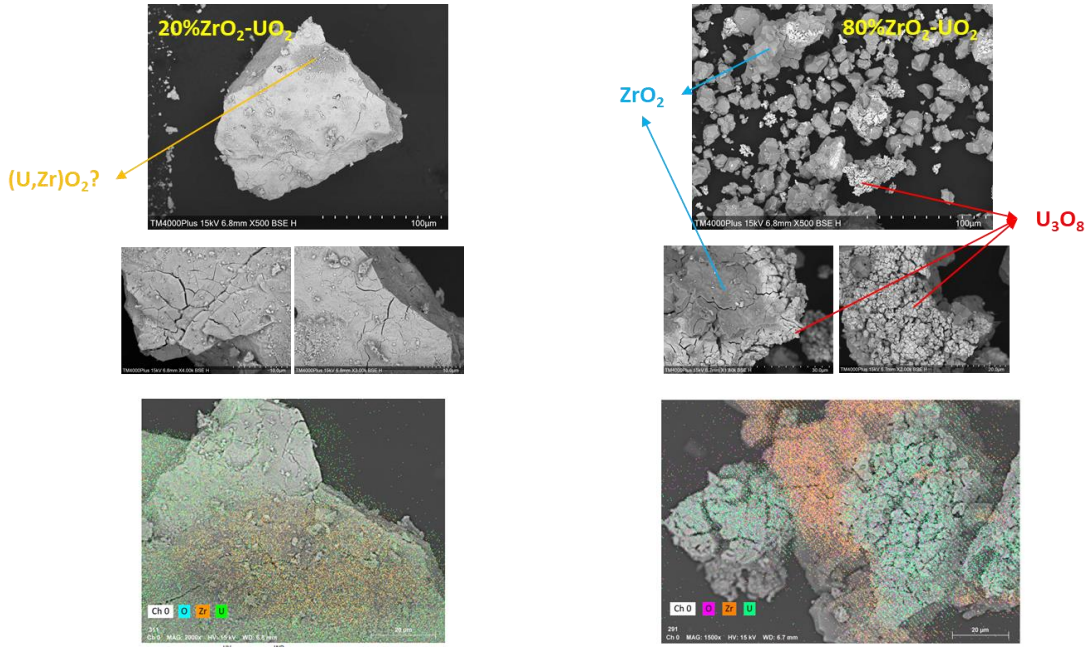

Figure 3-14: SEM-EDX images of the 20 wt% ZrO_2 -UO_2 (a) and 80 wt% ZrO_2 -UO_2 (b) samples after 10 h of oxidation treatment in air at 300 °C.

3.4 General discussion and conclusions

This task comprises description of experimental approaches and obtaining experimental data that can be used for the examination of the multiscale systems with irradiated fuel. Three issues are addressed in detail: 1) the synthesis and microstructural characterisation of *ad-hoc* fuel surrogate of FCI in a

representative way; 2) the evolution of these ZrO_2-UO_2 systems (with a range of ZrO_2 contents) due to oxidizing degradation; 3) the overall responses of powdered samples at temperature and oxygen partial pressure coupling effects.

The oxidation behaviour observed for the three ZrO_2-doped UO_2 contents (20, 40 and 80 wt%) as a function of temperature and oxygen partial pressure provides essential data for evaluating FCI behaviour as a consequence of oxygen exposure. Mixtures of ZrO_2-doped UO_2, in the full range of possible compositions across the layer (simulating the ZrO_2/UO_2 chemical bonding in LWR fuels, FCI phenomenon), and undoped UO_2 have been obtained and characterised. The fabrication of surrogate samples via "powder route", is a complex process, and it is susceptible to inducing segregated ZrO_2 phases (depending on the solubility limit) and polymorphism of ZrO_2 in samples depending on the sintering conditions.

This work aims to better understand the parameters that govern the oxidation reaction by analysing a variety of ZrO_2-doped UO_2 materials. The systematic methodology using thermogravimetry was used on x wt% ZrO_2-UO_2 (x=0, 20, 40, 80 and 100) samples for *in-situ* monitoring of the oxidation reaction of UO_2 to U_3O_8 under "representative" conditions of a dry environment as a function of: a) ZrO_2 content; b) oxidizing atmosphere: O_2 % (1 and 21%); and c) temperature. A series of TGA tests were performed and oxidized samples were also characterised. Solid samples were analysed under non-isothermal (10 $^{\circ}C \cdot min^{-1}$, up to 900 $^{\circ}C$) and isothermal (100, 300 and 400 $^{\circ}C$) conditions. Kinetic data illustrating the oxidation of these compounds is presented and discussed. The thermal analysis on some representative model materials of a HBU fuel and FCI showed that no clear differences in non-isothermal systems were observed between different oxidizing conditions (1 and 21 $\%O_2$). According to the results obtained so far, some preliminary concluding remarks can be formulated. The pointed-out difficulties about ZrO_2 solubility in the UO_2 matrix and polymorphism of ZrO_2 can affect the subsequent oxidation responses of the tested samples.

The complete oxidation of powdered samples under non-isothermal conditions reveals potential effects of ZrO_2. The obtained TGA curves indicate that the presence of zirconium in the UO_2 fuel matrix provides certain oxidation resistance to U_3O_8, hindering matrix oxidation. Additionally, the higher the O_2%, the higher the oxidation degree of uranium matrix for ZrO_2 contents below 40 wt% in UO_2 showing that ZrO_2 can improve the thermal oxidative stability of UO_2 to some extent. The use of relatively low partial pressures of oxygen did not avoid severe degradation, although the evidences found for samples analysed suggest that, over a certain ZrO_2 content threshold, the oxidation degree is slightly influenced by oxygen pressure.

Under isothermal conditions, the temperature as a key affecting parameter on fuel matrix alteration is confirmed. Increasing ZrO_2 content decreases the mean oxidation degree. In general, the effect of low oxygen concentration in the gas phase induces a moderation of the oxidation degree on average, for the same Zr content but with no remarkable implications. Additional characterisation is ongoing.

The experimental results obtained in this task provide a very interesting dataset for future multiscale experimental approaches. Further experimental work is necessary to better characterise and simulate the UO_2-ZrO_2 inter-diffusion layer. Additional analyses with controlled ZrO_2 polymorphic phases will refine the data and contribute to describe the FCI behaviour under the context of a potential oxygen exposure during storage conditions.

Therefore, the results of this analysis are important not only for considering possible loading/unloading cells of SNF or even under transport in O_2 containing environments, once closure of pellet-cladding gap occurs, but also in evaluating a conventional method to be applied for understanding the oxidation behaviour of SNF during the back-end of the fuel cycle, *i.e.*, handling transport and storage. However, to implement this assumption on real irradiated fuel, further research involving other characterisation techniques , such as transmission electron microscopy, Raman spectroscopy or thermal test, as well as considering the presence of FP (*e.g.*, Cs, I, Cd) in the Zr/ZrO_2 zone must be explored.

4. Segmented mandrel tests of pristine and hydrogenated VVER fuel cladding tubes performed by HUN-REN EK

4.1 Introduction

During normal reactor operation, the fuel pellet goes through several processes, breaks up, compacts, swells, and then reaches the cladding. During this time, the cladding creeps inwards towards the pellet due to the high external pressure. The coefficient of thermal expansion and the operating temperature of the two materials are also different, so their thermal expansion will also be different during operation. Usually within one or two years of normal operation the gap between the pellet and the cladding closes completely and pieces of the pellet interact mechanically and chemically with the cladding. The iodine produced by the fission and the mechanical load exerted by the pellet together can lead to stress corrosion cracking, the zirconium iodide produced in the cracks, which makes the metal brittle, promotes the propagation of cracks in zirconium.

Examining the cracking and fracture behaviour of the cladding is important for both normal operation and accident scenarios. During a reactivity accident, the ductile or brittle deformation of the cladding at operating temperature determines which cracking or fracture mechanisms are initiated by the suddenly increased mechanical stress and whether the integrity of the cladding is maintained. Similarly, it is important to investigate the long-term behaviour of claddings exposed to normal operational corrosion and hydrogen uptake in a temporary dry storage, where the cladding temperature decreases together with the internal pressure. During the drying of the fuel assemblies, part of the precipitated hydrogen previously absorbed by the cladding may dissolve back into the metal, and radially oriented hydrides may be formed in addition to the hydrides that were typically circumferential. These can increase crack susceptibility and propagation risk, and their effect can be important during transfer to a final storage facility.

In order to model the interaction between the pellet and the cladding, mechanical tests are often carried out with the help of a multi-element tensile tool to determine the ductility limit of the fuel cladding tubes or the rings cut from them. These expanding segmented tensile tools are called mandrels. Their role is to evenly distribute the radial load along the cladding samples. The advantage of the test is that it is relatively easy to perform and does not require lengthy preparation and irradiation to produce pellets that are fragmented to the appropriate extent. The initial heat treatment and corrosion of the samples, the amount of absorbed hydrogen or iodine can be controlled, and the tested samples can be inactive or irradiated. These tests can be performed both at room temperature and elevated temperatures, closer to the operating temperature of the cladding.

Within the mandrel method, the design of the tools and the measuring arrangement can be different. In the simplest case, a tool consisting of 4 or up to 12 mandrels can be used for the tests, the more segments result in a more uniform stress distribution. Their number is limited only by their mechanical strength and by issues related to handling. Since they have to be located in a cladding tube or ring (with an inner diameter of 7.5 mm to 9.8 mm, depending on the fuel type), the mandrels are also extremely small and small tolerances must be used during their manufacturing. The tool material may be steel or some hard ceramic (such as tungsten carbide) and may be in direct or indirect contact with the ring samples. In the indirect case, to simulate the fragmentation of the fuel pellets, a fragile ceramic ring is placed between the tool and the sample, which breaks in several places during the test and a maximum stress develops where the pieces come into contact with the cladding.

Using the direct contact method, described by Karl- Fredrik Nilsson and his colleagues at JRC-IET Petten [105], a cone or spike is pressed into the centre of the mandrel segments (*Figure 4-1*). The fundamental disadvantage of this method is that the design of the tool is much more complicated. The advantage of the method is that the cone does not deform, that is, the measured force depends only on the angle of the cone and the friction between the contacting surfaces, so the radial force on the sample could be determined more precisely.

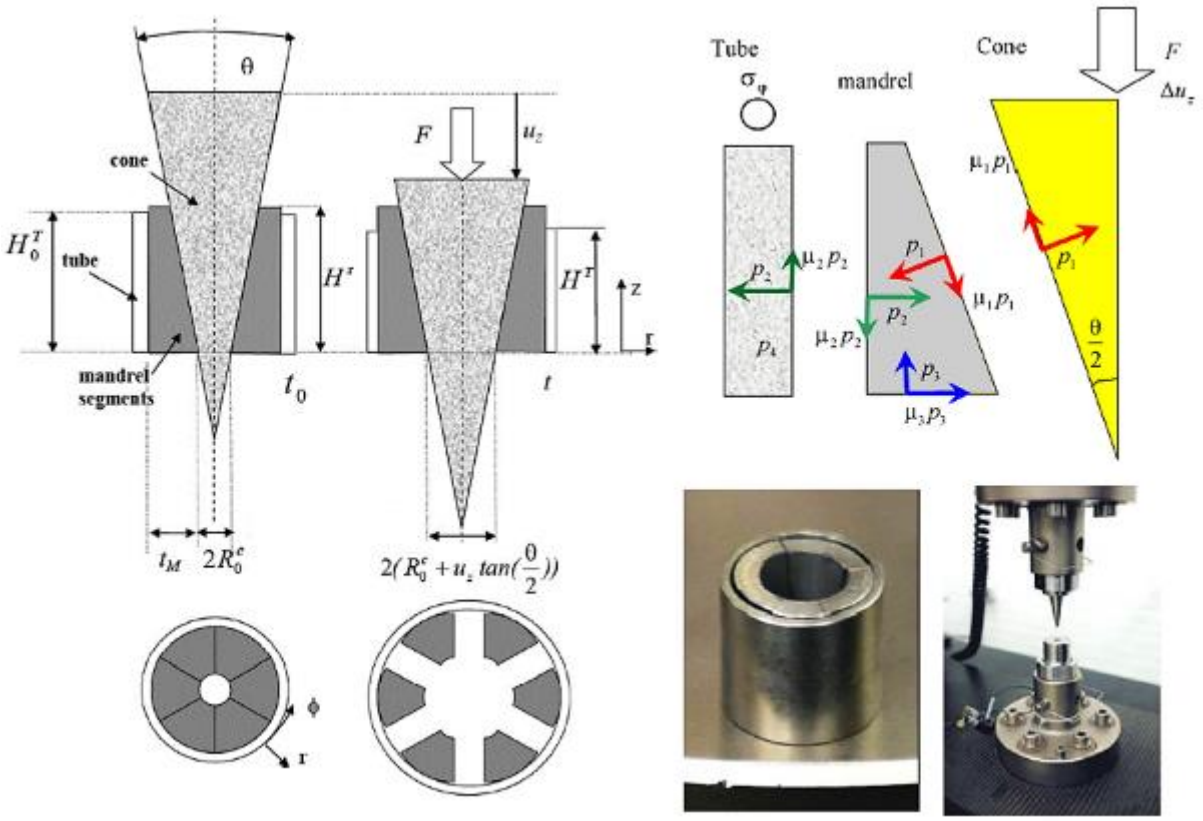

Figure 4-1: The mandrel method as described by Karl- Fredrik Nilsson and his colleagues at JRC-IET Petten [105].

4.2 Design of the test

4.2.1 The test apparatus

The initial objective of the research was to create a simple measurement procedure that can be used to model the mechanical interaction between the pellet and the cladding (PCMI). To model the interaction, we designed a unique measuring arrangement and a tool consisting of segmented mandrel elements, which can be used to test the ductility of ring samples produced from zirconium fuel cladding tubes under mostly radial load. The design basis was the geometry designed in JRC Petten, and we decided on using 8 mm long cladding ring samples. In order to prepare the experiments to be carried out with the segmented tool, we first created a three-dimensional finite element model, and with the help of this we analysed the selected tool geometry and designed the applicable tool [106]. The friction coefficient between the measured ring sample, the parts of the tool and the supporting base was defined as the same, and then the force associated with the spike was determined as a function of the friction. We have seen that the tool can be damaged during the test in the case of 20° cone angle spike, which was in the original design. By reducing the cone angle to 11.5°, this deformation stress was reduced by one order of magnitude. In the case of a spike with a smaller cone angle, to create the same stress in the sample, a larger crosshead displacement must be made, which enables loading at lower speeds. The finite element model was also suitable for the analysis of geometric cone angle.

We found that the greater the number of tool segments, the more uniform the stress on the zirconium cladding rings. The results of the calculations showed that stress inhomogeneity develops along the gaps between the segments of the tool, but this inhomogeneity decreases during the measurement, and a radial stress field is formed on the contacting surfaces while plain strain condition was observed

between the mandrel segments. However, increasing the number of segments means a decrease in the wall thickness of the mandrels themselves. Due to the small size of the test pieces and the achievable manufacturing accuracy (according to ISO2768m, the tolerance is 0.1 mm, which can be critical, primarily on the inner side of the tool), we chose to use a tool consisting of six segments. The results of the preliminary numerical simulation confirmed that in this case, a relatively homogeneous stress field is obtained in the part of the ring samples in contact with the mandrel.

During the design of the tool, we took the geometry obtained by finite element modelling as a basis, on which we made several changes based on the results of the simulation, as well as to facilitate the implementation of the measurement and to clarify the measurable values. The height of the mandrels was chosen to be 9 mm, so that the 8 mm long rings can fit well on them, while the outer radius of the tool was chosen to be 3.7 mm (the nominal inner diameter of the rings we used was 7.8 mm). Since a burr is usually formed during the cutting of the tubes with a lathe, reducing the effective inner diameter of the rings, this tolerance was necessary to facilitate the handling of the samples. We replaced the conical spike with a hexagonal pyramid and the inner side of the mandrels was also changed to accommodate that for a better fit between the spike and the mandrel. In order to improve the tool's handling, the mandrels have been expanded with a widening part under the active tensile region in contact with the samples, which on the one hand helps with the positioning of the rings, and on the other hand, the tool remains in one place between tests due to the circular spring that fits into the groove located in the middle of this wide part. This geometrical change was also an advantage in the later design phases, as the lower, wider rim can also help in removing the spike at the end of the test.

To support the mandrels and to be able to mount the measurement on the universal testing machine, we have designed a tool that guarantees that the mandrels stay together between measurements, and helps to separate the mandrels and the spike at the end of the test (*Figure 4-2*). If the test was stopped before sample failure, and the tested ring sample was not torn or broken, then due to the conical elements, the spike may get stuck between the mandrels held together by the ring. In this case, by raising the crosshead, the mandrels are pressed against the upper cover of the holding tool and get separated from the spike.

The need for tests at elevated temperatures necessitated the design and construction of a unique furnace around the mandrels. The holding tool designed around the mandrels and the spike was placed in a tube furnace, their size was limited by the inner diameter of this furnace. In order to achieve the high performance with the lowest possible heat loss, as well as due to the small amount of available space and the need to be able to heat up quickly, the furnace had to be compact. The main dimension of the furnace was the 40 mm inner diameter, for which the holding tool had to be redesigned. The size of the holding tool that fits into the tube furnace limited the maximum outer diameter of the mandrel. The radius of the lower part of the mandrel became 10.7 mm, and the size of the groove holding the spring was increased based on the preliminary results, so that it would sit in place even during the measurement of a brittle sample that breaks suddenly. This was necessary because during a high-temperature measurement it is not possible to adjust the mandrels enclosed in the holding tool. The mandrels were manufactured from Böhler K360 Isodur material, which is a cold forming chrome steel tool alloy. After manufacturing with a CNC milling machine, the surface was polished to remove milling marks, then hardened to a hardness of 60 HRC (Rockwell) with a heat treatment at 1050 °C for 20 minutes The final design of the mandrels and the spike can be seen on *Figure 4-2*.

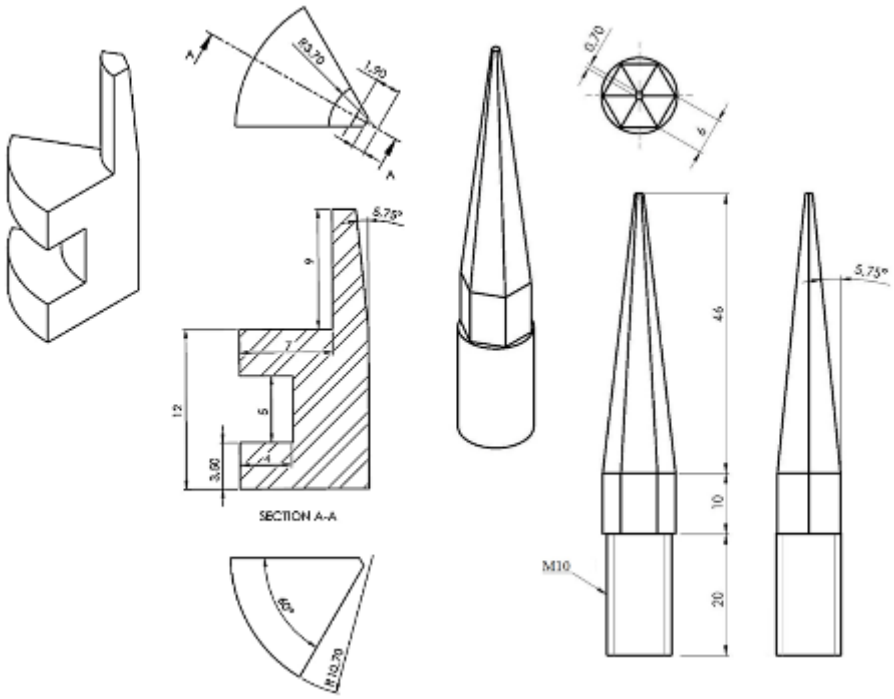

Figure 4-2: Drawing of the finalized mandrel segment (left) and the spike (right).

The furnace constructed around the test consists of two parts, the upper half heats the spike and an extension attached to the crosshead of the testing machine and the lower half heats the ring sample, the mandrels and the holding tool (*Figure 4-3* and *Figure 4-4*). The two halves built around the tools can be moved independently and close with a conical fit. To change the samples, the furnace had to be openable, since the 8 mm long rings can only be slid onto the mandrels from above, and the correct fit between the spike and the mandrels had to be checked every time. Easy handling and controllability had to be taken into account during the design of the furnace. When closed, the furnace maintains the set temperature within an accuracy of ±1 °C, in reference to previous tests performed at 150 °C and 300° C; the two halves are controlled separately based on two thermocouples. During the tests, it was found that after opening the furnace, due to the rapid cooling, the controller would heat with maximum power, but after closing, when the heat loss is significantly reduced again, the temperature will exceed the set value and would only slowly decrease back to the set point. To prevent this, we added a switch-off timer for both controllers, after which they automatically restarted. This was necessary due to the coupled nature of the two systems, as the lower half of the furnace in its closed state contacts and heats the upper half, and vice versa, but the masses of the two halves are different. For this reason, the heating was off while the furnace was open, the lower part started to heat immediately after the sample change and closing, and the upper part restarted about 1-2 minutes later. Thus, the time elapsed between the two tests, together with sample change and the holding time to ensure the constant temperature around the sample, could be shortened to about 10 minutes.

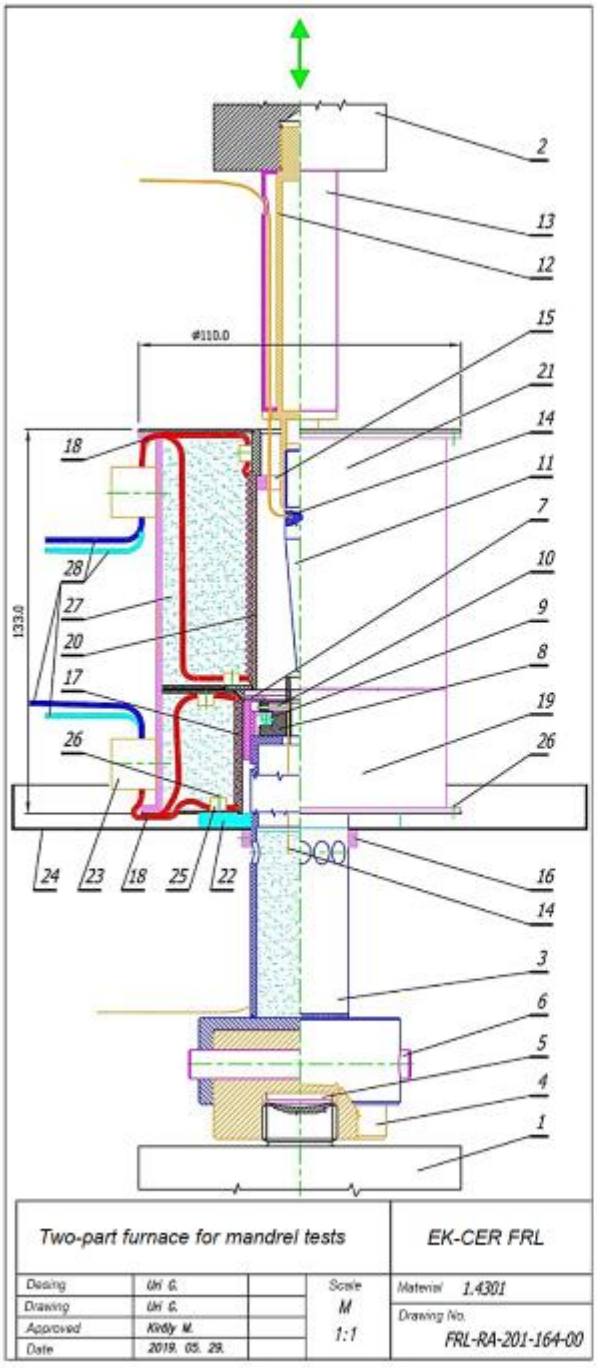

No.	Part
1.	Instron load cell connection
2.	Instron crosshead connection
3.	Mandrel holding tool
4.	Threaded lower connection
5.	Lens
6.	Bolt and nut
7.	Holding tool top cover
8.	Mandrel tool
9.	Circular spring
10.	Grub-screw
11.	Spike
12.	Threaded upper extension
13.	Sheath
14.	K type thermocouple
15.	Retainer ring 1
16.	Retainer ring 1
17.	Furnace lower part
18.	Thermocoax heating element
19.	Lower furnace casing
20.	Furnace upper part
21.	Upper furnace casing
22.	Insulating ring
23.	Ceramic terminal block
24.	Tray
25.	Retainer segment
26.	Dormant bolt
27.	Rockwool insulation
28.	Electric cable

Figure 4-3: Detailed blueprint of the furnace with individual elements.

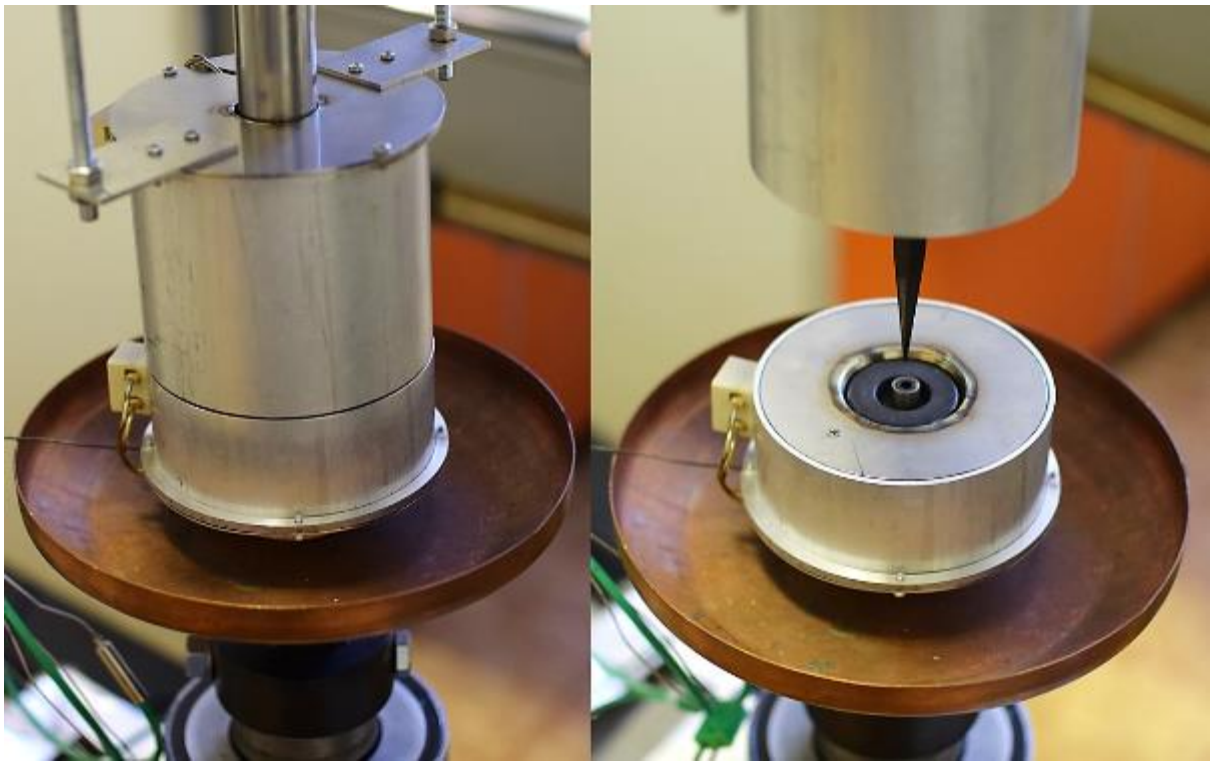

Figure 4-4: The mandrel furnace in the closed (left) and open (right) state. The fixing of the upper furnace half to the crosshead was solved with levers mounted on threaded rods.

4.2.2 Experimental design

Within the framework of the EURAD programme, we were investigating the behaviour of as-received cladding ring samples and samples exposed to hydrogenation. The tests were carried out with 8 mm long rings cut from the Zr1%Nb alloy E110 currently used in VVER reactors like Paks NPP, and rings cut from the fuel cladding tubes made of the very similar E110opt alloy fabricated using a new production technology [107]. Both tubes had the same geometric parameters of 9.097±0.008 mm outer and 7.755±0.005 mm inner diameter.

We prepared an experimental design, in which we proposed the parameters for the pre-treatment of the samples to be tested at room temperature and at 300 °C. The proposed hydrogen content was ranging from 500 wppm up to 3500 wppm, although for the samples tested at 300 °C we only went up to 2500 wppm hydrogen content. We completed the experimental design, which involved the testing of over 100 E110 and E110opt rings, both untreated and hydrogenated to varying degrees. During the tests, we recorded the displacement of the crosshead of the universal testing machine and the compressive force that could be measured under the holding tool. Since the purpose of the test was not to determine the tensile strength or the yield strength, but the determination of the ductile-brittle transition under PCMI conditions, the force-displacement values obtained during the test can only be used as approximations to estimate the loads taken by the samples.

For the hydrogenation of E110 and E110opt cladding samples, a three-zone tube furnace with a calibrated volume gas inlet system and a vacuum system was assembled according to *Figure 4-5*. Before starting the measurement, the samples were degreased with an organic solvent (acetone) and then air-dried. The weight of the samples before and after hydrogenation was measured on a Sartorius SE2 electronic ultramicrobalance. One sample at a time was placed on the quartz glass sample holder with a soft iron core. The sample together with the sample holder was first placed in the end of the quartz tube outside the furnace area and the apparatus was sealed. After evacuation, the system was filled with high-purity (99.9999%) hydrogen to the calculated initial pressure, and then the system pressure

was topped up to atmospheric pressure with high-purity (99.9999%) argon. The quartz glass sample holder with a soft iron core was pushed together with the sample into the preheated 700 °C furnace with the help of a strong magnet on the outside, and then at the end of the hydrogenation, the sample was pulled back into the cold part of the quartz tube. The pressure corresponding to the total volume (hydrogen + argon) was continuously measured. The process of hydrogen absorption in the cladding was indicated by a decrease in total pressure. The time and the approximate quantity of hydrogen required to charge the cladding samples with 1000 weight ppm of hydrogen was established based on previously performed tests. After 1 hour, the pressure did not decrease any further, i.e., the hydrogen content of the samples reached equilibrium with the hydrogen in the gas space. The hydrogen content was measured by weighing, using an ultra-micro balance (Mettler Toledo XP2U) with 10^{-7} g readability. The mass gain was corrected by the average mass gain of the blind samples, that were treated in pure argon in the same setup, in order to give the hydrogen uptake of each sample, with an accuracy of ± 5 ppm.
Loading with hydrogen was carried out at high temperature, during which the cladding samples were also subjected to heat treatment. In order to assess the effect of this heat treatment on the ductility and to separate it from the effect of the hydrogen, a few E110 and E110opt samples were heat treated in high-purity argon at 700 °C for the same period of time, and their behaviour was examined under the same conditions as the hydrogenated samples.

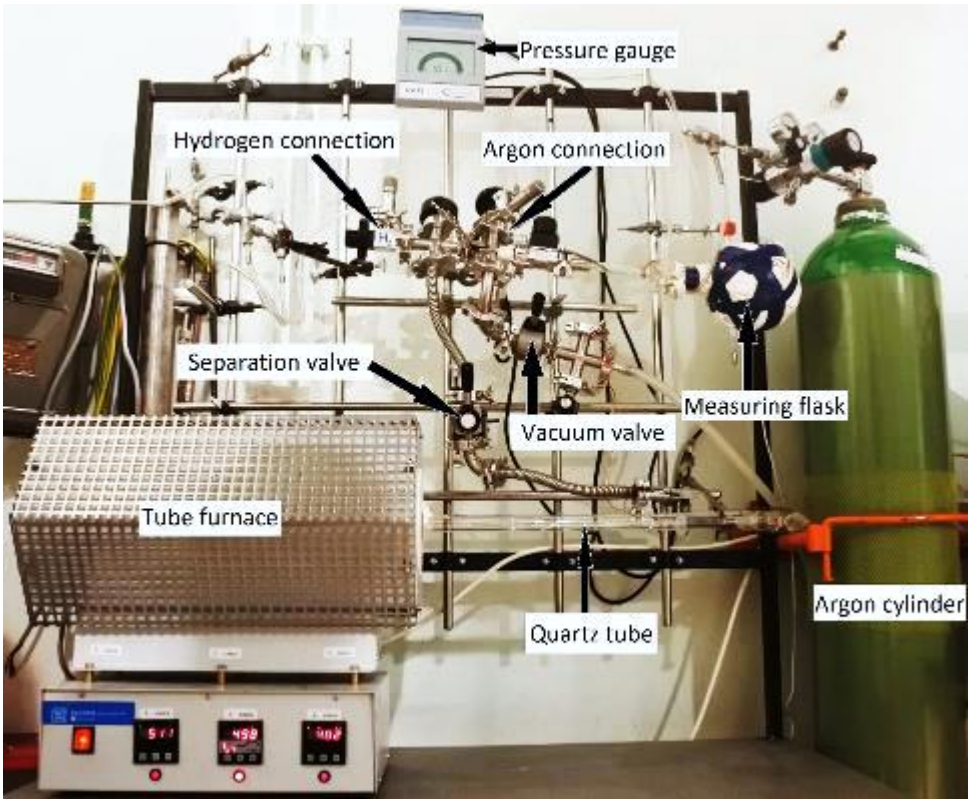

Figure 4-5: The equipment used to load the cladding samples with hydrogen.

4.3 Experimental

The mandrel test apparatus was placed on the lower crosshead of an Instron 1195 type universal testing machine, the load cell was located under the holding tool and the spike with its extension was attached to the upper crosshead. At the beginning of the test, the moving spike pulls the mandrels into the centre, then the ring is positioned so that it rests evenly on the tool. The initial movement of the loosely fitting mandrels and the ring is normal, this usually occurs at a low force, typically below the measured force

of 1000 N. During the tests, we experienced a slight deflection of the upper extension holding the spike by a few degrees. This was to be expected due to the construction of the extension that was welded together from several pieces. Since brittle samples tended to break into several pieces and fly apart, the furnace was closed during the tests, even with tests conducted at room temperature.

In order to determine the loading speed of the rings to be used during the measurement series, we previously carried out measurements with different movement speeds of the spike [108]. During the speed tests, we chose the crosshead speed of 2 mm/min. The speed of 2 mm/min ensures a slow loading, the sample reaches the maximum force in about 2-3 minutes at the beginning of the measurement, and in the case of plastic samples, the measurement is completed in 12-15 minutes.

The tests were carried out until the samples broke or failed, because the maximum diameter change up to failure (similar to the maximum elongation) also provides important information in addition to the measured force. We started each measurement day with a baseline measurement (using as-received samples) to check the reproducibility of the mandrel test. These results were in good agreement, the variation was about 5%.

We used a high temperature grease to lubricate the contacting surfaces to lower overall friction. However, most lubricating greases available on the market can be used up to a maximum of 200 °C, instead of the needed 300 °C. Lubricating fats and oils will either boil off or decompose above 200 °C. This is also true for paraffin-based, silicone-based and linseed-based greases. In the case of greases mixed with graphite, Teflon decomposes at higher temperatures, while molybdenum sulphide solid lubricants use a diluting oil the typically disappears above 200 °C, and the friction properties of the remaining lubricant thus changes. According to the manufacturer's data, a bearing grease called Molykote 41, which is a mixture of phenyl-methyl-silicone and graphite powder, can be used between -20 and 290 °C, so we were able to use the same lubrication for both room temperature and high temperature measurements. In the case of measurements at elevated temperatures, the greasing had to be repeated every measurement day, thus ensuring a constant coefficient of friction. Overall, it can be said that reliable, reproducible results were obtained during the measurements, in which the lubrication of the tool played a decisive role.

4.3.1 Evaluation of the data

The purpose of the mandrel tests was to model the mechanical interaction between the cladding and the pellet, i.e., to examine how the cladding behaves after different treatments when it comes into contact with the fuel pellet fragments, which are considered rigid. It is possible to evaluate the ductility of the samples based on several different measured and calculated values. When evaluating the test results, we determined three basic parameters: the relative inner diameter increase (ΔD%), the specific force (F_{max}/H_0) and the integral work (IW). These were calculated from the force-displacement data recorded by the testing machine.

The maximum inner diameter reached before failure characterises the residual ductility. In the measured data, the crosshead displacement (T) is the maximum measured crosshead displacement before failure, from which the increase in the inner diameter of the rings can be calculated. Although the diameter of the rings did not increase cylindrically symmetrically, this value gives an average displacement of the ring. The average inner diameter change compared to the original diameter in can be calculated as follows:

$$\Delta D_i(\%) = \frac{T \cdot 2 \cdot \sin\left(11.5^\circ / 2\right)}{D_{i0}} \cdot 100\% \approx \frac{T}{39} \cdot 100\% \quad ,$$

where: T (mm) is the measured crosshead displacement

D_0 (mm) is the original inner diameter of the samples (in our case it was 7.8 mm).

The maximum of the measured force is related to the strength of the samples. This value was typically lower in the case of highly ductile samples than in the case of brittle samples, and with increasing temperature it decreases similarly to the tensile strength. The specific force was obtained by dividing the maximum force achieved during the measurement by the original length of the ring samples (F_{max}/H_0).

The calculation of the area under the force-displacement curve serves to take the previous two values into account. The force measured at each moment is proportional to the differential work required to deform the given ring sample. During the measurement, the displacement of the crosshead of the testing machine and the vertical compressive force were continuously registered with the help of the load cell under the tool. The obtained integral of the force-displacement curve was normalized to the diameter increase of the ring, and then the obtained value was divided by the original length of the rings. With this, we defined a value which is proportional to the deformation work done on the ring samples. We named this integral work (IW), and its unit of measure became mJ/mm. This value is proportional to the work performed on the ring, but also includes the sum of the friction work performed on the tool and other losses, but these factors remained constant during the test.

4.4 Results

4.4.1 As-received samples

First, we performed mandrel ductility tests on as-received samples at room temperature and at 300 °C. The results of the tests with the as-received samples are shown in *Table 4-1*. The sample name MSE8 means 8 mm long E110 samples and the MSG8 refers to E110opt samples. Both examined zirconium alloys behaved very plastically. After reaching the yield point, the deformation of the rings progressed up to 60-80% inner diameter increase before failure (*Figure 4-6*). The holding tool was designed to enable measurements of up to 90% diameter increase (if the mandrels are in the centre of the tool), and we approached this limit during some tests. The rings took on a hexagonal shape due to the six-piece tool. The degree of expansion was not uniform since different stresses develop on the parts of the ring in contact with the tool and in the parts between the mandrels. As a result of the plain strain between the mandrels, the height of the rings decreased faster there, so the samples took on a "crown" shape at the end of the tests, and necking also usually started between the mandrels. The deformation obtained as a result of the experiments was similar to that expected based on the finite element simulation [106]. The location of the point of failure was variable between measurements, i.e., there was no significant difference between the mandrels and there was no primary orientation, the sample could break between any two mandrels. In terms of the way of failure, the crack usually started from the centre of the laced part, in the axial direction, and then the two wings that were created in this way broke off at around the same time (*Figure 4-8*)[2]. At 300 °C the measured maximum force was about half of the force measured at room temperature and the change in diameter until failure was somewhat higher (*Figure 4-7*).

[2] In the case of irradiated fuel rods under interim storage conditions, breaking of the cladding can occur through additional phenomena e.g., delayed hydride cracking, stress corrosion cracking or alpha-radiation induced damaging of the cladding.

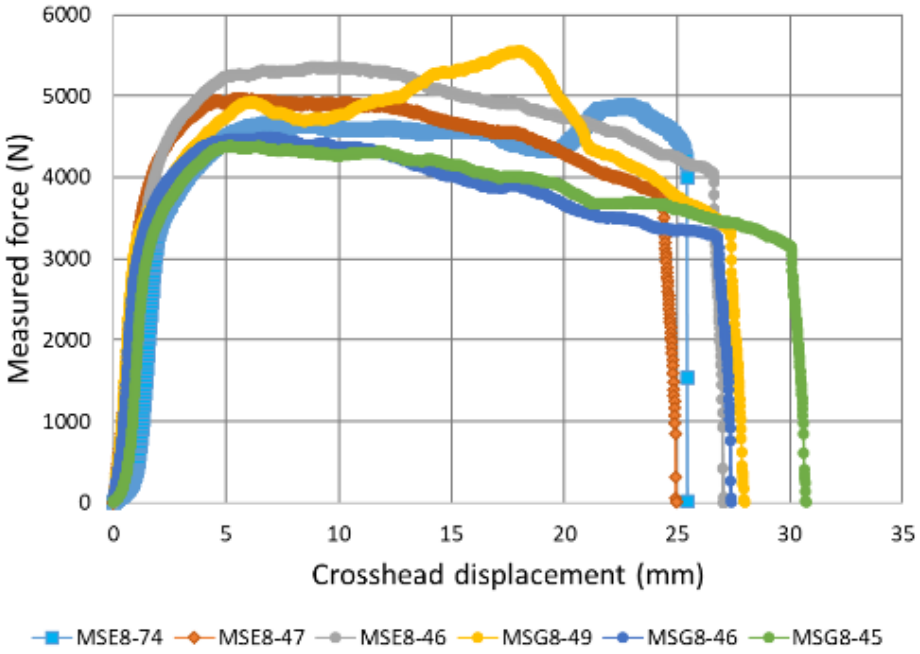

Figure 4-6: The measured force as a function of the crosshead displacement for as-received samples at 20 °C.

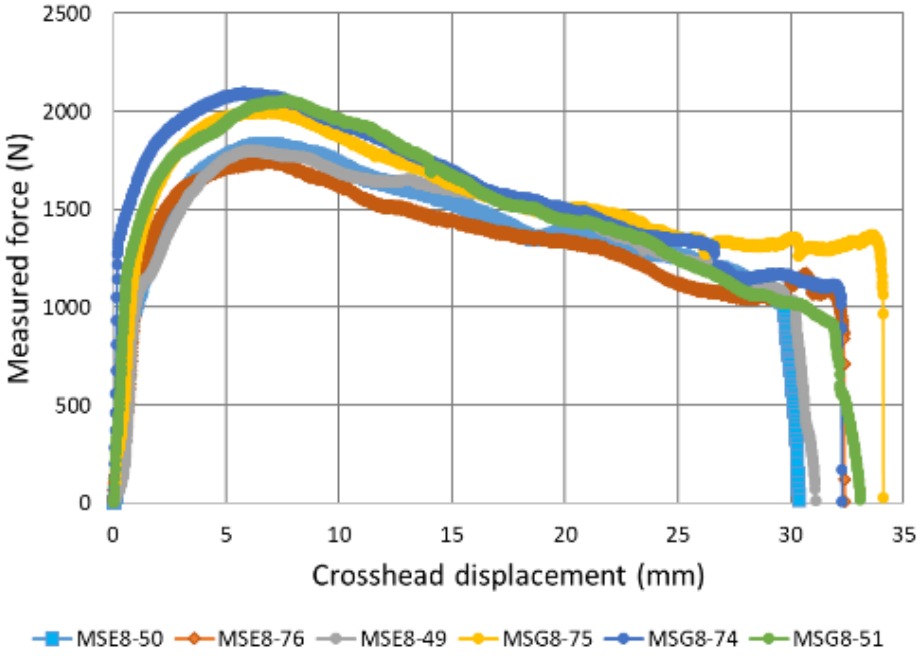

Figure 4-7: The measured force as a function of the crosshead displacement for as-received samples at 300 °C.

Figure 4-8: Deformations caused by the mandrel tool. On the left is an 8 mm as-received E110opt ring, in the middle after 30% diameter increase and on the right side, a torn sample with an inner diameter increased by about 80%.

Table 4-1: The results of the mandrel tests with the as-received samples.

Sample No.	Temperature (°C)	Material	ΔD% (%)	Fmax/Ho (N/mm)	IW (mJ/mm)
MSE8-74	20	E110	65.23	596.2	2624.9
MSE8-47	20	E110	64.00	602.1	2653.3
MSE8-46	20	E110	69.44	663.1	3118.8
MSG8-49	20	E110opt	71.79	682.8	3062.2
MSG8-46	20	E110opt	70.26	549.6	2562.6
MSG8-45	20	E110opt	78.74	542.1	2849.7
MSE8-50	300	E110	77.81	226.7	1068.8
MSE8-76	300	E110	83.04	216.8	1080.1
MSE8-49	300	E110	79.73	221.3	1084.5
MSG8-75	300	E110opt	87.45	246.1	1272.9
MSG8-74	300	E110opt	82.74	256.1	1267.0
MSG8-51	300	E110opt	84.85	254.8	1229.0

4.4.2 Hydrogenated samples

The hydrogenated samples were also tested both at room temperature and at 300 °C. The upper limit of the hydrogen content was set at 3500 wppm, as we did not expect any further changes above that. The results are summarized in the tables within the appendix section of this report. The sample name PHE refers to hydrogenated E110 samples and the PHG refers to E110opt samples. The increasingly brittle behaviour was also observed during the tests, as the plastic deformation of the samples with low hydrogen content was replaced by brittle fracture of samples with high hydrogen content (*Figure 4-9*). By increasing the hydrogen content, the samples failed sooner, with a smaller maximum inner diameter increase, and the ductility decreased almost linearly up to 2000 wppm hydrogen content (*Figure 4-10*).

The transition can also be seen in the specific maximum force, as the brittle samples took significantly, 50-100% more force during the measurements than the ductile samples (*Figure 4-11*). The values reach the limit between 1500-2000 wppm, after which they do not change much, this can be considered the ductile-brittle transition threshold. The sharp transition found in ring compression tests between ductile and brittle behaviour was not observed (*Figure 4-12*) since the more even load in the radial direction promotes plastic deformation.

Figure 4-9: Mandrel tests of hydrogenated E110opt samples at room temperature after 15% inner diameter increase. The left sample (PHG-53, 489 wppm hydrogen) still exhibited ductile behaviour while the right sample (PHG-83, 2059 wppm hydrogen) was brittle and broke.

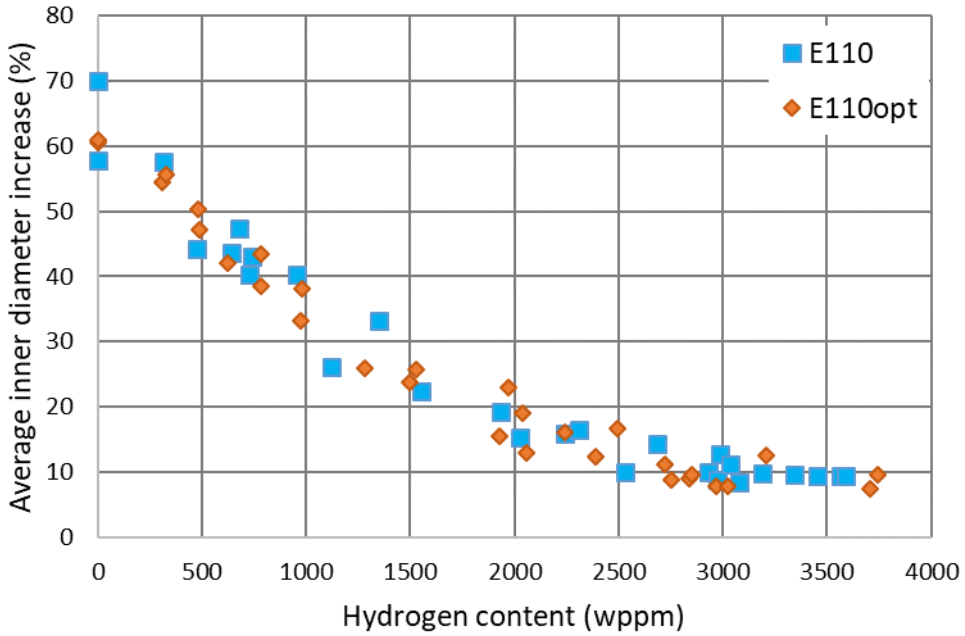

Figure 4-10: The maximum diameter change as a function of the hydrogen content at 20 °C.

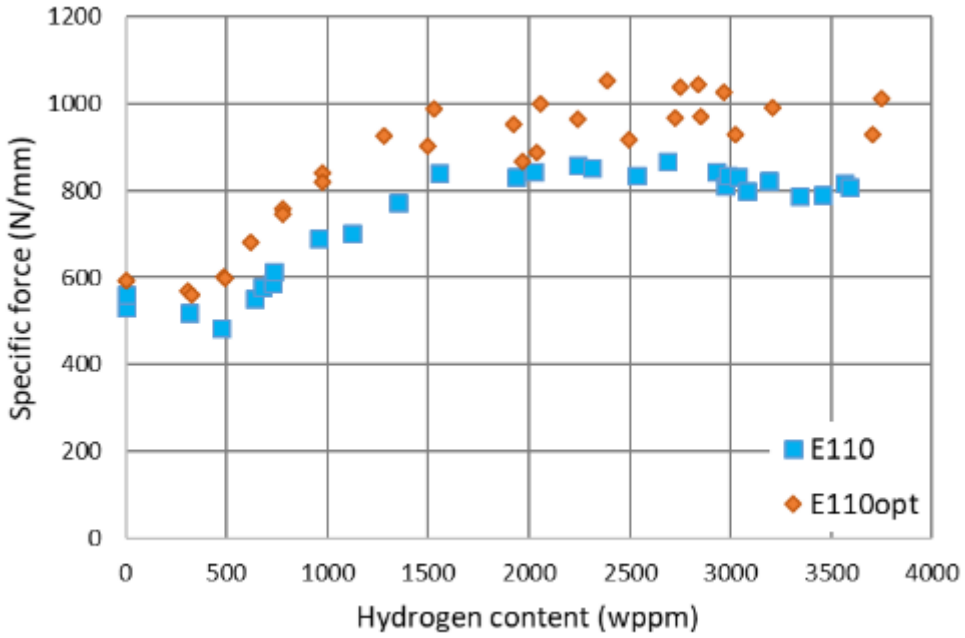

Figure 4-11: The specific maximum force as a function of the hydrogen content at 20 °C.

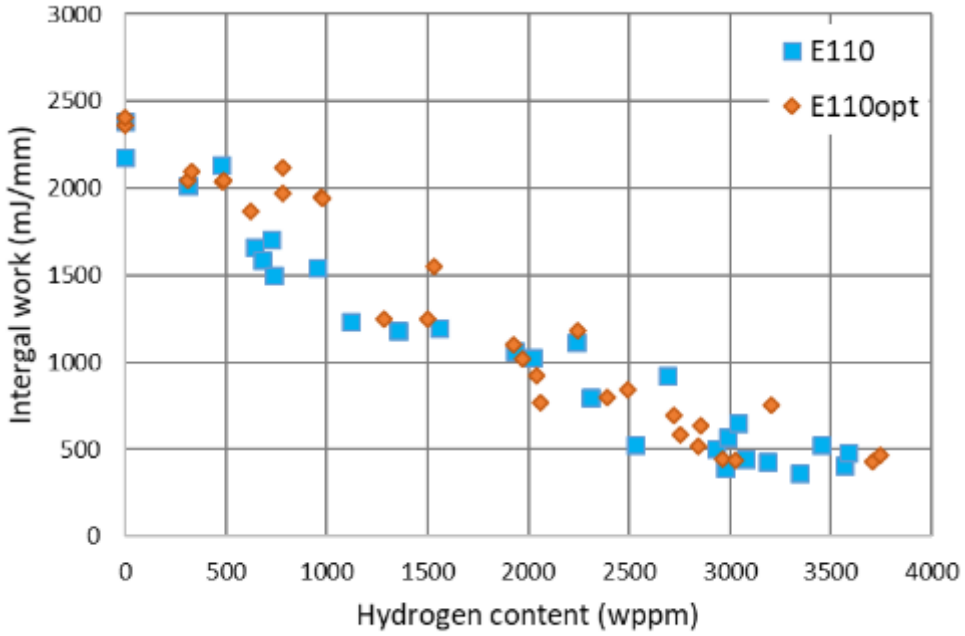

Figure 4-12: The integral work as a function of the hydrogen content at 20 °C.

In the mandrel tests conducted at 300 °C, the total elongation increased, but the measured force was lower than at room temperature (*Figure 4-13* and *Figure 4-14*), as expected based on the effect of temperature on the strength [109]. However, in contrast to the measurements at room temperature, the integral work did not decrease up to a hydrogen content of 1500 wppm (*Figure 4-15*), and the maximum inner diameter was also above those measured at room temperature, i.e., the greater ductility at higher

temperatures can somewhat offset the hardening effect of the hydrogenation. The so-called blank samples, containing no hydrogen but treated under the same conditions - subjected to the same heat treatment at 700 °C as the hydrogenated samples - showed that the heat treatment increases the strength by a few percent compared to the as-received state [107].

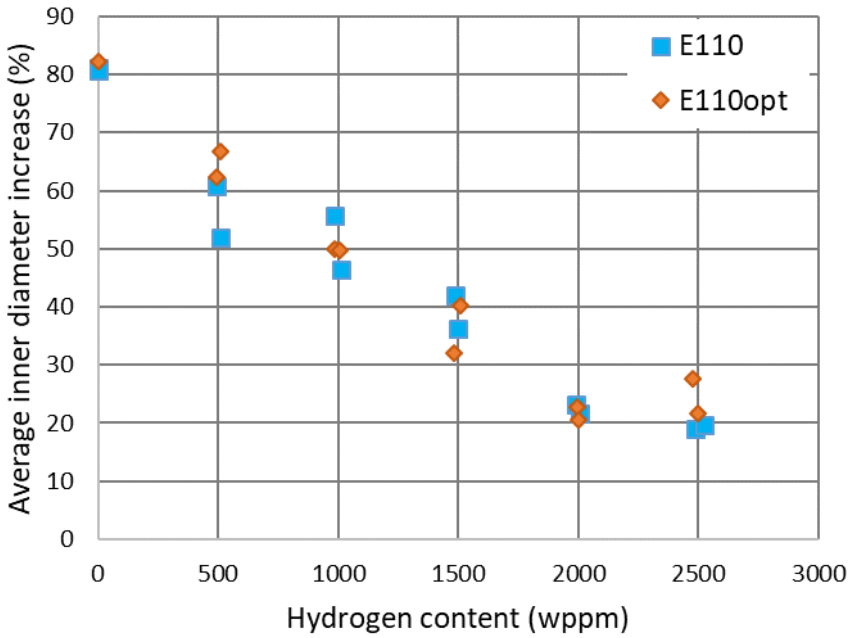

Figure 4-13: The maximum diameter change as a function of the hydrogen content at 300 °C.

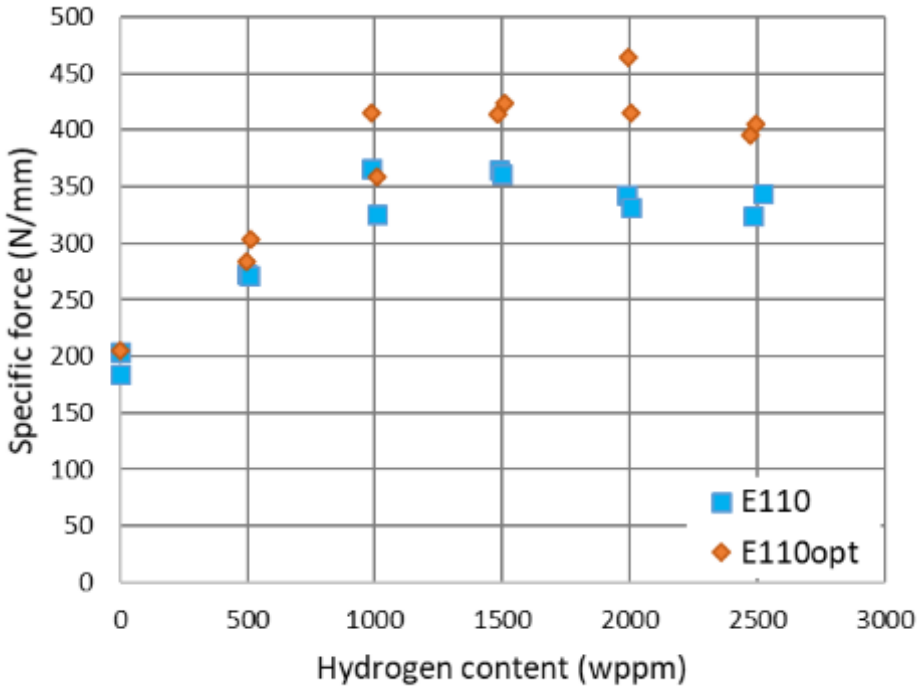

Figure 4-14: The specific maximum force as a function of the hydrogen content at 300 °C.

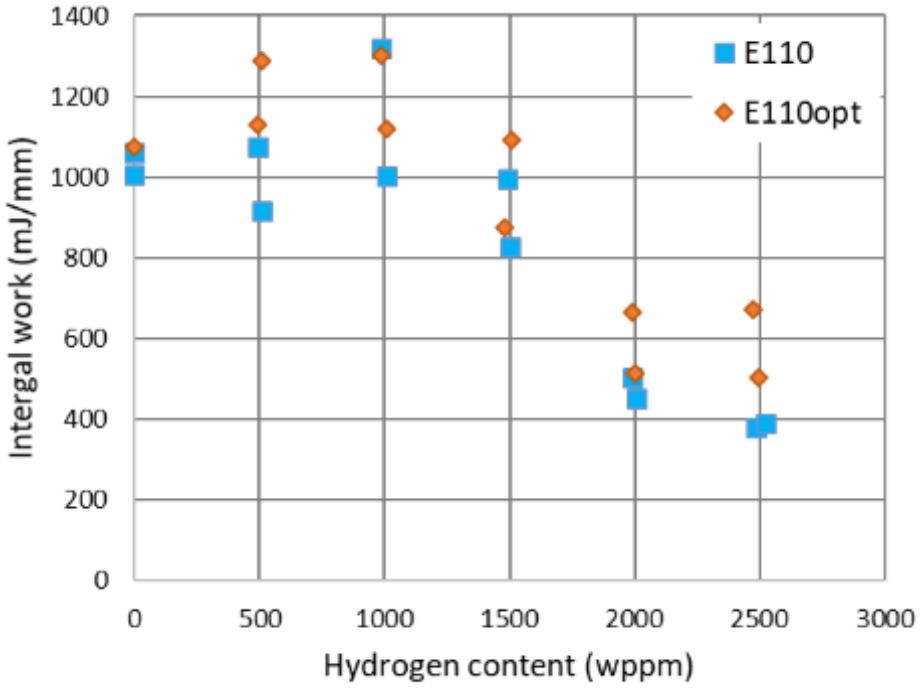

Figure 4-15: The integral work as a function of the hydrogen content at 300 °C.

4.5 Summary

Based on the available literature, we designed and built a measurement arrangement with which the processes that occur during the mechanical interaction between the pellet and the cladding can be examined under the influence of radial load. Within the framework of the EURAD project, mandrel ductility tests were performed to examine the ductility of ring samples cut from zirconium fuel cladding tubes. The behaviour of these samples exposed to hydrogen at high temperature and inert gas was also measured. A two-part, high-temperature tube furnace was built around the measurement arrangement, with which we were able to perform tests at room temperature and at 300 °C.

By increasing the hydrogen content, the samples failed at smaller maximum inner diameter, and the ductility decreased almost linearly up to 2000 wppm hydrogen content. The transition can also be seen in the specific maximum force, as the brittle samples absorbed significantly, 50-100% more force during the measurements than the ductile samples. The values reach the limit between 1500-2000 wppm, after which they do not change much, this can be considered the ductile-brittle transition threshold.

5. Synchrotron investigations and neutron radiography on the pellet-cladding interface of a high burn-up BWR fuel performed by PSI

5.1 Introduction

During irradiation of fuel rods in light water reactors (LWR), the UO_2 pellets directly interact with the enclosing Zircaloy cladding above a threshold burn-up of ~40 GWd/t_{HM}. This occurs when the fuel-cladding gap tends to close due to pellet swelling and cladding creep-down onto the fuel. After a physical contact between the pellet and cladding is established, the inner surface of the Zircaloy wall at the pellet-cladding interface is oxidized due to the oxygen diffusion from fuel. This leads to the formation of a bonding layer of zirconia at the region of the fuel-cladding interface (FCI). As the presence of fuel-cladding bonding may affect the thermo-mechanical behaviour of a fuel rod, especially for high burn-up fuel, experimental analyses of the formation, stability, stress-strain states, and microstructure of this bonding layer are important for ascertaining validity and reliability in predicting the thermal as well as mechanical behaviour of fuel rods, especially in the context of intermediate dry storage. The focus of this study lies in the FCI region of a high burn-up spent fuel pellet irradiated in a commercial Swiss BWR (*Figure 5-1*). The cladding material of a BWR fuel rod typically consists of an outer Zircaloy-2 cladding tube and an inner liner, comprised of several ten micrometres in thickness, fabricated by co-extrusion. The liner had been invented to mitigate effects of pellet-cladding interaction during power transients. Post-irradiation examinations showed that the liner attracts hydrogen, and densely formed hydrides can be found in the liner by light optical microscopy [110–112] as shown (*Figure 5-2*). The accumulation of hydrides in the liner can be considered as beneficial because it leaves the bulk material of the cladding relatively hydrides free. Our specific interest has been to study in how far local stresses at the FCI may have an influence on the formation of hydrides and their morphology. It has also been of interest whether massive local hydrides accumulation could occur and act as potential site for crack initiation. Our method of choice has been synchrotron-based techniques at PSI's Swiss Light Source (SLS).

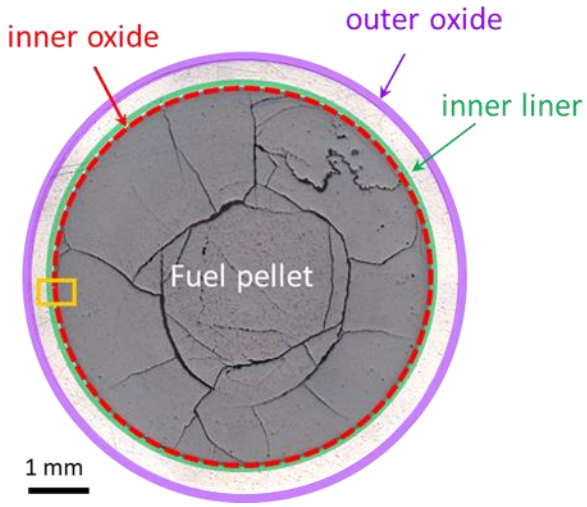

Figure 5-1: Optical image of a fuel rod cross-section: area of interest at interface region between cladding and pellet (yellow rectangle), comprising inner liner as used for BWR cladding, inner oxide (bonding layer) and fuel [112].

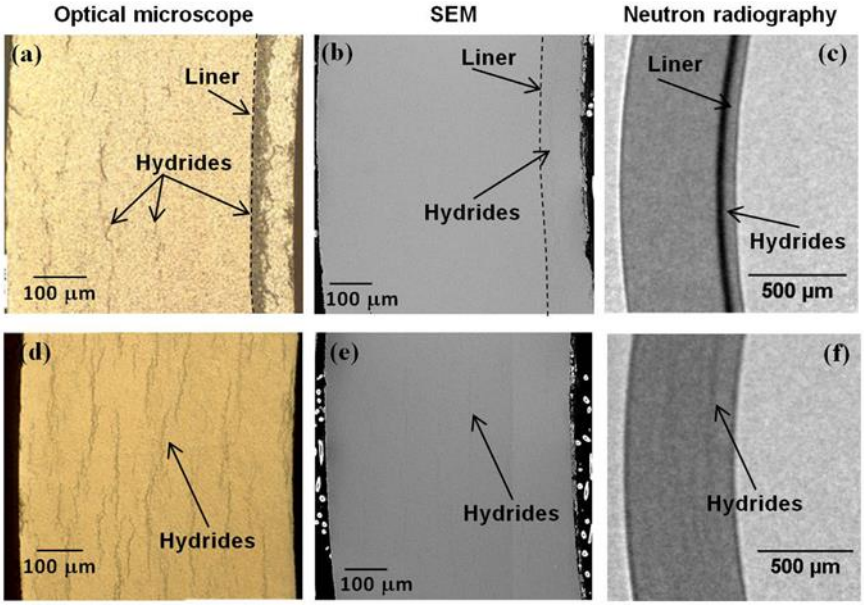

Figure 5-2: Hydrides distribution in Zircaloy-2 BWR cladding after slow cooling visualized by light optical microscopy, SEM and neutron radiography; comparison between cladding with liner, top row, (a) – (c), and without liner, bottom row, (d) – (f), strong accumulation of hydrides in the liner [111].

5.1 Sample material and preparation

5.1.1 BWR cladding and microstructure at fuel-cladding interface area

A spent fuel rod from a Swiss BWR was chosen. The pellet consists of standard UO_2, and the cladding of Zircaloy-2 with an inner liner (LK3/L). The rod average burn-up was 61 GWd/t_{HM}. The cladding liner exhibits a strong accumulation of hydrides, especially close to the substrate-liner interface. At the inner surface of the cladding (i.e., the liner), a bonding layer follows, which consists mainly of ZrO_2. Adjacent to the bonding layer, the pellet outer area exhibits high burn-up structure (HBS) with many pores due to the fission gas bubbles and further precipitated or dissolved fission products (*Figure 5-3*).

Data on the structural properties (phases, crystallography, lattice strain) of the bonding layer and its potential impact on residual stresses and thus possibly on the hydrides' formation are scarce, and for BWR cladding inexistent.

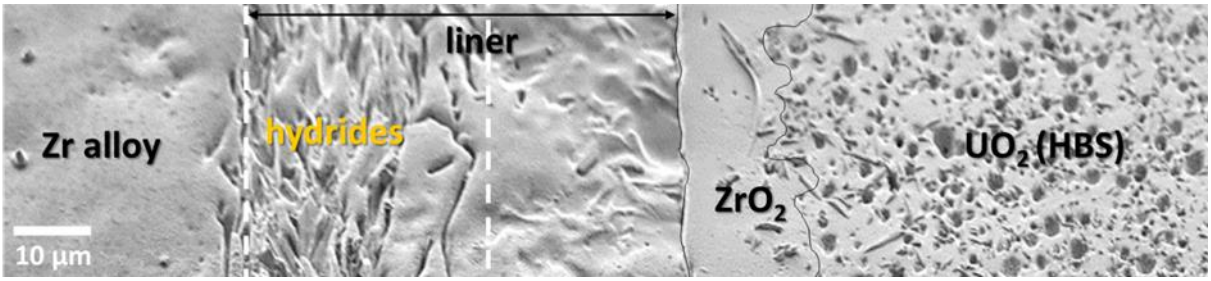

Figure 5-3: SEM image of areas from cladding to pellet, comprising hydrides accumulation in the liner, bonding layer and high burn-up structure (HBS) at the periphery of the fuel pellet [112].

For the structural characterisations of the prepared samples, a combined synchrotron-based micro-beam X-ray fluorescence (µXRF) and X-ray diffraction (µXRD) experiment was carried out in tomo-graphic mode, performed at the microXAS beamline of the Swiss Light Source (SLS) at PSI.

Two samples were extracted close together:

- one from the strongly hydrides dense area of the liner (see *Figure 5-4*), and
- one at the interface including the liner, zirconia layer and the fuel in contact (see *Figure 5-5*).

To comply with the radioprotection aspects as well as legislation issues for investigation of radioactive materials at the SLS, the sample size was reduced to micrometric scale by focused ion beam (FIB) technique.

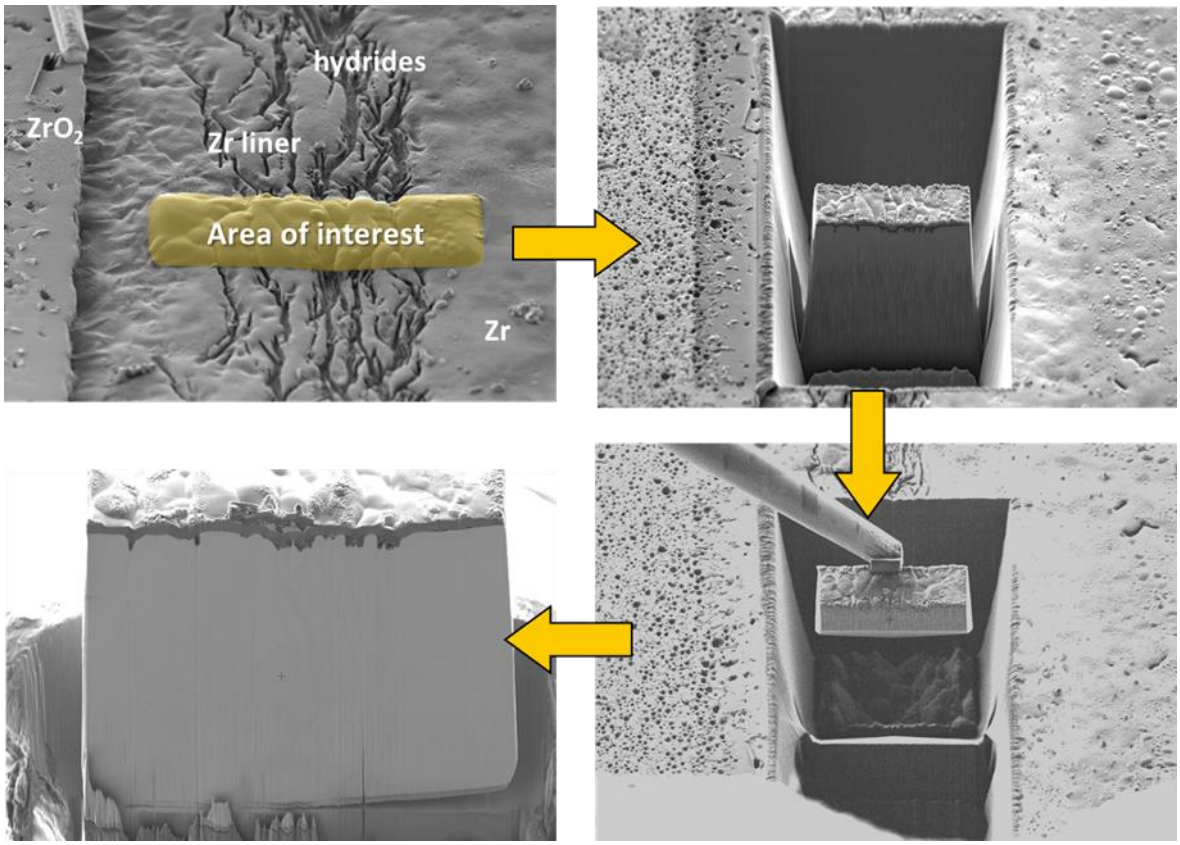

Figure 5-4: SEM pictures of FIB preparation of densely hydrided sample area, final sample size is about 34 µm x 58 µm x 18 µm; area selection, milling, lift-out and bonding (in clockwise direction) [112].

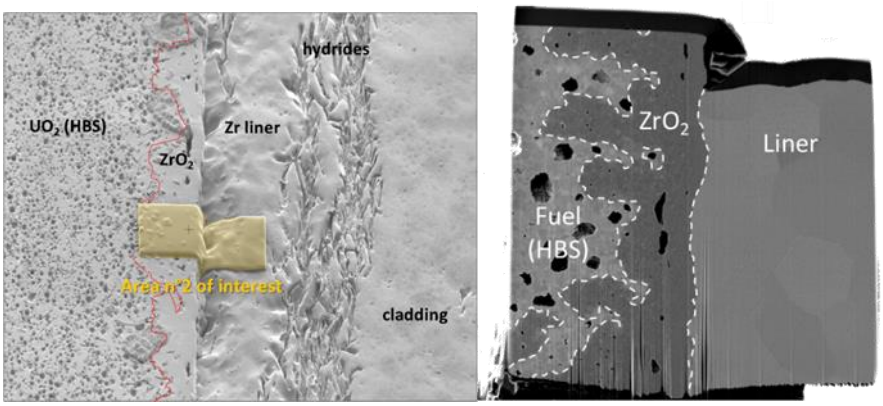

Figure 5-5: SEM pictures of area of ZrO_2 bonding layer (area 2) and FIB prepared sample, final sample size is about 34 µm x 34 µm x 17.5 µm [112].

5.2 Synchrotron investigations

5.2.1 Experimental conditions

The synchrotron experiment was performed at the microXAS beamline of PSI's Swiss Light Source SLS. The experiment was carried out in scanning transmission configuration, whereas the fluorescence (XRF) signal and diffraction (XRD) pattern could be simultaneously acquired at the same beam spot location. To achieve this, a 2D detector was used for XRD, as well as four SSD detectors arranged around the sample for XRF, see *Figure 5-6*. Two beam energies were used, 17.95 and 18.01 keV (below and above the Zr K-edge), in tomography mode (i.e., with a rotation +/-90° of the sample). Data acquisition was carried out using a focused beam about 0.9 µm in size, with a step size of 0.3 µm and dwell time of 200 ms.

µXRF maps, obtained with high spatial resolution, were used to precisely localize the different materials making up the FCI (Zr, ZrO_2 and UO_2). The crystalline phases were identified using the µXRD with a correlation map representing the spatial distribution of the diffracting domains.

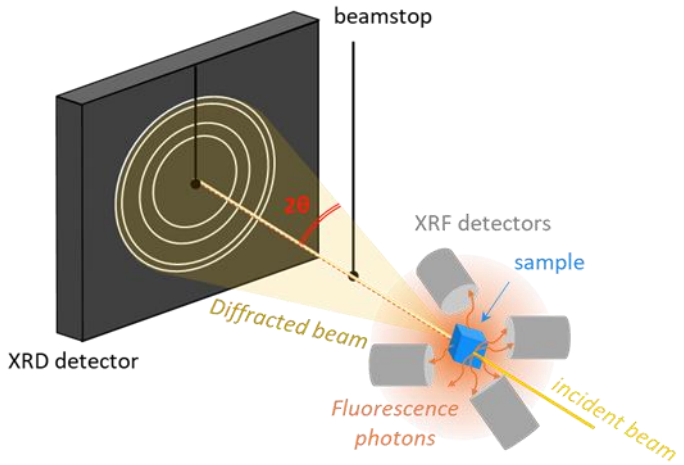

Figure 5-6: Schematic set-up at beam line, XRF signal and XRD pattern simultaneously acquired in tomography mode [110].

The XRD data were analyse using Match!3 software [113], and PyMca 5.8.7 [114] was used for analysing the XRF data.

5.2.2 Synchrotron results

The hydrides phases could be very well localized. Based on the micro-scanning, XRD reconstruction maps could be created, showing the locations of the different types of hydrides, see *Figure 5-7*.

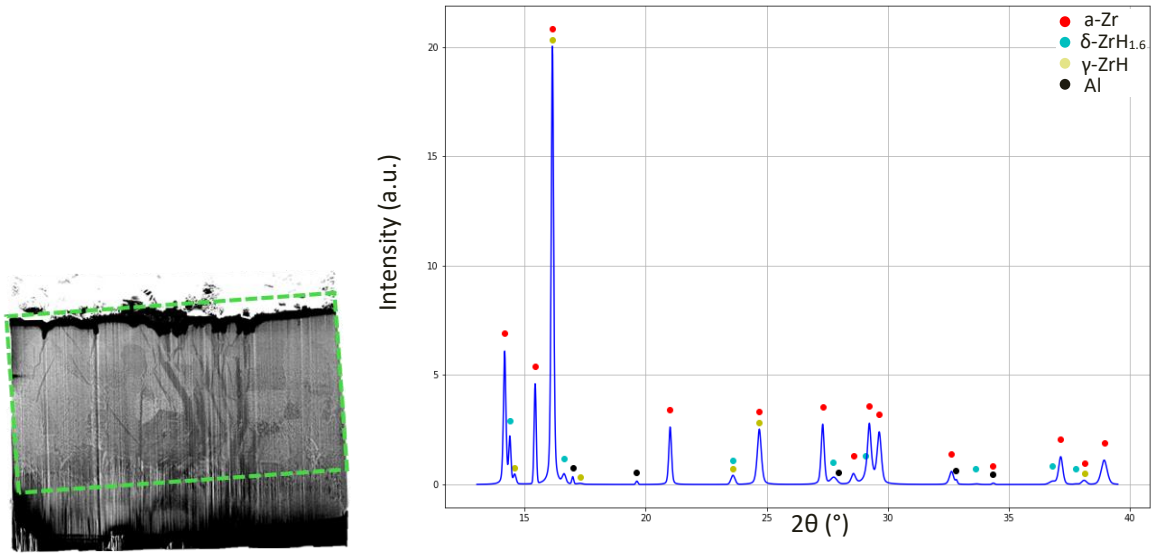

Figure 5-7: XRD analysis of hydrides. The green rectangle indicates the area of interest. XRD pattern shows clearly peaks from δ- and γ-hydrides phases [112].

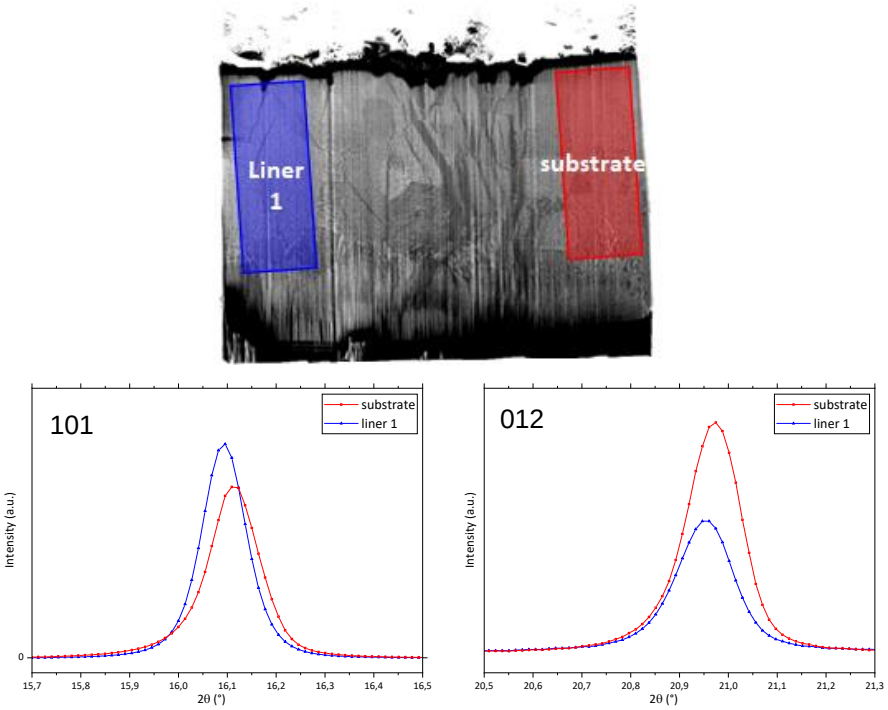

Figure 5-8: Shifts of (101) and (012) peaks at two different positions, i.e., in the substrate close to the substrate-liner interface (indicated in red), in the liner close to the accumulated hydrides (in blue) [112].

The δ-phase is predominant at the interface between liner and substrate. The γ-phase is minor and occurred more within the liner thickness. It is unclear whether this difference can be attributed to possibly higher residual stresses inside the liner due to the interaction between pellet and the cladding exerted by the bonding layer. A closer look onto XRD peaks at locations in the liner close to the hydrides' accumulation, as well as in the substrate close to the substrate-liner interface, reveals slight shifts on some peaks, see *Figure 5-8*. However, before making a valid statement about induced stresses by the pellet-cladding interface, the influence of created stresses by the sample preparation method, i.e., by

FIB cutting needs to be clarified and decoupled from the inherent material stresses. The respective work is ongoing.

In respect to the ZrO_2 bonding layer, tomographic XRF and XRD slicing was performed. The results show that the tetragonal zirconia (t-ZrO_2) is the main phase present, although it is a metastable form under LWR temperature and pressure conditions. In addition, the cubic phase of UO_2 (in contact with zirconia) has a larger lattice parameter than that of unirradiated UO_2. The presence of implanted fission products could be the reason for these differences. Further analysis of the fission products reveals the presence of a hexagonal crystalline phase corresponding to the one of the ε-particles structure, probably metallic fission products precipitates. In addition, krypton bubbles were observed within the zirconia layer using XRF (*Figure 5-9*). Although Xe could not be detected due to the technique used here, it is reasonable to assume that this fission gas, which is produced above 6 times more than Kr [115], is present in the bubbles at the FCI (already observed in the zirconia layer in non-negligible proportion using EPMA and STEM-EDS [116,117]).

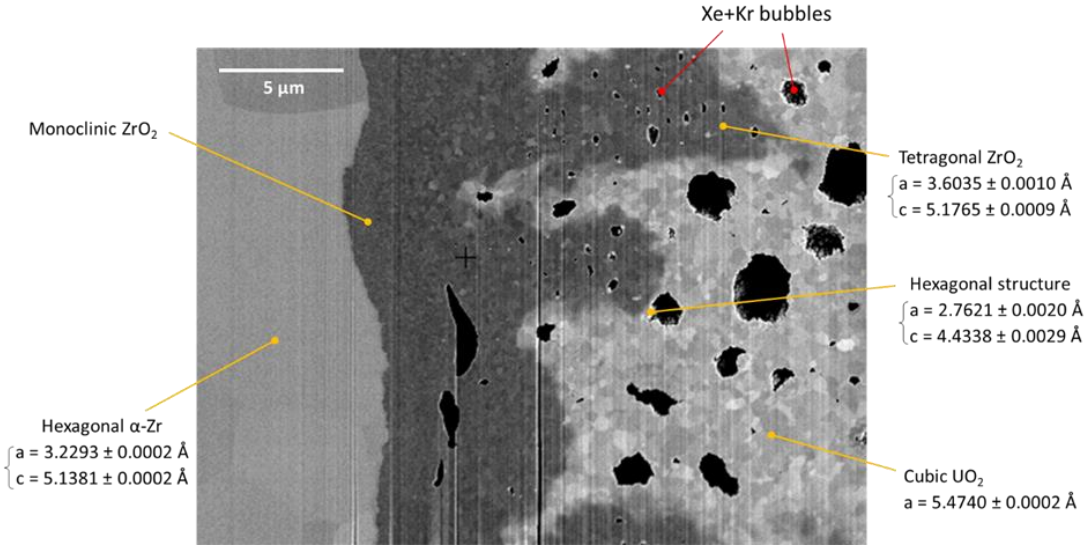

Figure 5-9: Phases identified at the fuel-cladding interface by XRD: in particular, presence of monoclinic and tetragonal ZrO_2 phases within zirconia interlocked in UO_2 (respective lattice parameters are indicated); in addition, identification of fission gas bubbles by XRF [118].

5.3 Inner oxide neutron radiography

A feasibility study has been performed on characterisation of the inner cladding oxide using neutron radiography. The problematic of the inner oxide is that there are various implanted spallation products with different contributions to the neutron attenuation. These elements had been investigated by EPMA beforehand. Although the inner oxide is visible with neutron radiography, the spatial resolution is too small to identify structures like undulations of the pellet-cladding interface, see *Figure 5-10*. Nonetheless, an advantage of neutron radiography is its non-destructive character and the possibility to detect stronger inhomogeneities like cracks or hydrides at the interface.

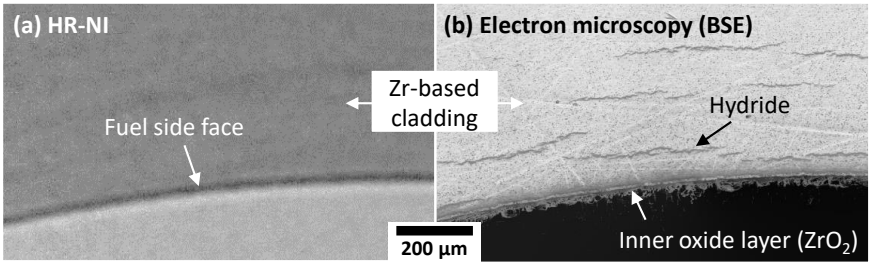

Figure 5-10: Comparison of high-resolution neutron image (HR-NI) (a) and SEM image based on backscattered electrons (BSE) (b), with their apparent different spatial resolution [110].

6. General conclusions

Within Subtask 3.3 of EURAD SFC, the outstanding work of all partners involved allowed to improve the understanding of the chemical and structural properties of the pellet-cladding system of irradiated nuclear fuels. By using state-of-the-art methods, ranging from synchrotron-based X-ray analyses of activation and fission products as well as incorporated hydrides into the cladding, mechanical tests of cladding material to scrutinise the mechanical interaction between fuel and cladding, as well as Raman measurements to further characterise the UO_2-ZrO_2 interdiffusion layer, the interaction between nuclear fuel pellet and cladding tube could be further elucidated.

This short summary of the work performed by the different partners is presented to illustrate the new insights gained by every institution contributing to this report in order to improve the knowledge on the behaviour of the fuel-cladding system:

Mandrel ductility test:

It was demonstrated, that by increasing the hydrogen content in the cladding specimens, a linear relationship between ductility decrease of the samples and incorporated hydrogen up to 2000 wppm hydrogen could be identified, indicating the presence of radial hydrides. The transition between ductile to brittle was also shown in the maximum force applied to the cladding specimens, as the brittle samples were able to absorb up to 100% more force during the measurement campaigns than the ductile specimens. After application of 1500 – 2000 wppm of hydrogen to the specimens, no change in mechanical behaviour was seen; thus, it is concluded, that the ductile-to-brittle transition threshold is then reached.

Investigations on the ZrO_2-UO_2-system:

The results obtained further elucidated the oxidation performance of the ZrO_2-UO_2 system, i.e., the pellet-cladding interaction layer, by using SNF surrogates. Furthermore, the oxidation resistance of UO_2 to U_3O_8 was shown, when it forms part of the (U, Zr)O_2 solid solution, mimicking the chemical bonding between ZrO_2 and UO_2. The overall results of this study improve the knowledge on the possible oxidation of SNF during loading / unloading in O_2 containing environments, when the fuel-cladding gap was closed.

Spectroscopic measurements on irradiated fuel:

Further insights on the behaviour of activation and fission products, present on the inner part of the cladding with respect to their chemical and structural properties on SNF rods could be gained. The results presented, elucidated the importance of measurements on actual SNF in order to complement the understanding of all processes involved in the behaviour of nuclear fuel after reactor irradiation.

X-ray analyses of irradiated fuel:

Thanks to the application of microfabrication techniques, it was possible to carry out synchrotron analysis of two samples of a high burn-up fuel rod. The combined µXRD/µXRF technique revealed (i) the presence of Kr bubbles at the fuel-cladding interface, (ii) hydrides in the cladding near the interface with the fuel, and (iii) lattice deformations in the three materials making up the pellet-cladding interaction, the Zr-based cladding, the zirconia and the UO_2 fuel. Although these results are still being analysed, they already demonstrate the complexity of the interface, given the many phases that need to be taken into account, but they are also a precursor for future experimental campaigns using large instruments for highly radioactive samples.

References

[1] R.C. Ewing, Long-term storage of spent nuclear fuel, Nat Mater 14 (2015) 252–257. https://doi.org/10.1038/nmat4226.

[2] IAEA, Behaviour of Spent Power Reactor Fuel during Storage, 2014. http://www-ns.iaea.org/standards/.

[3] IAEA ENERGY SERIES, Impact of High Burnup Uranium Oxide and Mixed Uranium – Plutonium Oxide Water Reactor Fuel on Spent Fuel Management, 2011.

[4] J. Bruno, R.C. Ewing, Spent nuclear fuel, Elements 2 (2006) 343–349. https://doi.org/10.2113/gselements.2.6.343.

[5] H. Kleykamp, The chemical state of the fission products in oxide fuels, Journal of Nuclear Materials 131 (1985) 221–246. https://doi.org/10.1016/0022-3115(85)90460-X.

[6] R.J.M. Konings, T. Wiss, O. Beneš, Predicting material release during a nuclear reactor accident, Nat Mater 14 (2015) 247–252. https://doi.org/10.1038/nmat4224.

[7] D.W. Shoesmith, Fuel corrosion processes under waste disposal conditions, Journal of Nuclear Materials 282 (2000) 1–31. https://doi.org/10.1016/S0022-3115(00)00392-5.

[8] E.C. Buck, B.D. Hanson, B.K. McNamara, The geochemical behaviour of Tc, Np and Pu in spent nuclear fuel in an oxidizing environment, in: Energy, Waste and the Environment: A Geochemical Perspective, 2004.

[9] D. Olander, Nuclear fuels - Present and future, Journal of Nuclear Materials 389 (2009) 1–22. https://doi.org/10.1016/j.jnucmat.2009.01.297.

[10] H. Bailly, D. Ménessier, C. Prunier, The nuclear fuel of pressurized water reactors and fast reactors: design and behaviour, Lavoisier Publishing, Paris, 1999.

[11] P. Rudling, A. Strasser, F. Garzarolli, Welding of Zirconium Alloys, 2007. https://doi.org/10.1080/09507119409548564.

[12] C. Ciszak, M. Mermoux, S. Miro, G. Gutierrez, F. Lepretre, I. Popa, K. Hanifi, I. Zacharie-Aubrun, L. Fayette, S. Chevalier, Micro-Raman analysis of the fuel-cladding interface in a high burnup PWR fuel rod, Journal of Nuclear Materials 495 (2017) 392–404. https://doi.org/10.1016/j.jnucmat.2017.08.038.

[13] R. Viswanathan, Fuel clad chemical interactions in fast reactor MOX fuels, Journal of Nuclear Materials 444 (2014) 101–111. https://doi.org/10.1016/j.jnucmat.2013.09.044.

[14] T. König, Examination of the radionuclide inventory and chemical interactions on the interface between nuclear fuel and Zircaloy-4 cladding in irradiated LWR-fuel samples, Dissertation, Karlsruhe Institute of Technology, 2022. https://doi.org/https://doi.org/10.5445/IR/1000148648.

[15] R.J. Pulham, M.W. Richards, Chemical reactions of dicaesium telluride, Cs2Te, and of dicaesium telluride/caesium mixtures with zirconium and with Zircaloy-4, Journal of Nuclear Materials 218 (1995) 143–150. https://doi.org/10.1016/0022-3115(94)00518-4.

[16] P.S. Sidky, Iodine stress corrosion cracking of Zircaloy reactor cladding: Iodine chemistry (a review), Journal of Nuclear Materials 256 (1998) 1–17. https://doi.org/10.1016/S0022-3115(98)00044-0.

[17] C.C. Busby, R.P. Tucker, J.E. McCauley, Halogen stress corrosion cracking of zircaloy-4 tubing, Journal of Nuclear Materials 55 (1975) 64–82. https://doi.org/10.1016/0022-3115(75)90137-3.

[18] O. Götzmann, H.J. Heuvel, Einfluss von Verunreinigungen auf die Hüllinnenkorrosion von stahlumhüllten oxidischen Brennstäben, Journal of Nuclear Materials 81 (1979) 231–219.

[19] D. Cubicciotti, J.E. Sanecki, Characterization of deposits on inside surfaces of LWR cladding, Journal of Nuclear Materials 78 (1978) 96–111. https://doi.org/10.1016/0022-3115(78)90508-1.

[20] R.W. Ohse, M. Schlechter, The Role of Caesium in Chemical Interaction of Austenitic Stainless Steels with Uranium Plutonium Oxide Fuels, EUR 4893 e, Karlsruhe, Germany, 1972.

[21] K. Konashi, T. Yato, H. Kaneko, Radiation effect on partial pressure of fission product iodine, Journal of Nuclear Materials 116 (1983) 86–93.

[22] P. Hofmann, J. Spino, Chemical aspects of iodine-induced stress corrosion cracking failure of zircaloy-4 tubing above 500°C, Journal of Nuclear Materials 114 (1983) 50–65. https://doi.org/10.1016/0022-3115(83)90072-7.

[23] J.C. Wood, FACTORS AFFECTING STRESS CORROSION CRACKING OF ZIRCALOY IN IODINE VAPOUR, Journal of Nuclear Materials 45 (1972) 105–122.

[24] R. Kaufmann, Oberflächenanalytische Untersuchungen zum thermischen Verhalten von passivierten Zircaloy-4 Oberflächen und Reaktionsverhalten von Iod an Zircaloy-4 Oberflächen, Technische Hochschule Karlsruhe, 1988.

[25] W.R. Stratton, F. Botta, R. Hofer, G. Ledergerber, F. Ingold, C. Ott, J. Reindl, H.U. Zwicky, R. Bodmer, F. Schlemmer, A comparative irradiation test of UO2 sphere-pac and pellet fuel in the Goesgen PWR., in: Int. Topical Meeting on LWR Fuel Performance “Fuel for the 90’s,” Avignon, France, 1991: pp. 174–183.

[26] K. Gösgen, Technik und Betrieb - Technische Hauptdaten, 2015.

[27] W. Goll, F. Schlemmer, P. Dewes, G. Fischer, D. Porsch, F. Sontheimer, R. Würtz, Abschlussbericht Förderungsvorhaben BMFT AtT 7685/8: Qualifikation von leicht löslichem Mischoxid-Brennstoff, Erlangen, Germany, 1988.

[28] H. Roepenack, F.U. Schlemmer, G.J. Schlosser, Development of Thermal Plutonium Recycling., Nucl Technol 77 (1987) 175–186. https://doi.org/10.13182/NT87-A33982.

[29] C.T. Walker, W. Goll, T. Matsumura, Effect of inhomogeneity on the level of fission gas and caesium release from OCOM MOX fuel during irradiation, Journal of Nuclear Materials 228 (1996) 8–17. https://doi.org/10.1016/0022-3115(95)00191-3.

[30] C.T. Walker, W. Goll, T. Matsamura, Further observations on OCOM MOX fuel: microstructure in the vicinity of the pellet rim and fuel-cladding interaction, Journal of Nuclear Materials 245 (1997) 169–178. https://doi.org/10.1016/S0022-3115(97)00009-3.

[31] P. Carbol, P. Fors, S. Van Winckel, K. Spahiu, Corrosion of irradiated MOX fuel in presence of dissolved H2, Journal of Nuclear Materials 392 (2009) 45–54. https://doi.org/10.1016/j.jnucmat.2009.03.044.

[32] V. V. Rondinella, T. Wiss, The high burn-up structure in nuclear fuel, Materials Today 13 (2010) 24–32. https://doi.org/10.1016/S1369-7021(10)70221-2.

[33] B. Ravel, M. Newville, ATHENA, ARTEMIS, HEPHAESTUS: data analysis for X-ray absorption spectroscopy IFEFFIT, J Synchrotron Radiat 12 (2005) 537–541. https://doi.org/10.1107/S0909049505012719.

[34] V.A. Solé, E. Papillon, M. Cotte, P. Walter, J. Susini, A multiplatform code for the analysis of energy-dispersive X-ray fluorescence spectra, Spectrochim Acta Part B At Spectrosc 62 (2007) 63–68. https://doi.org/10.1016/j.sab.2006.12.002.

[35] C. Degueldre, J. Bertsch, M. Martin, Post irradiation examination of nuclear fuel: Toward a complete analysis, Progress in Nuclear Energy 92 (2016) 242–253. https://doi.org/10.1016/j.pnucene.2016.03.025.

[36] H. Kleykamp, The chemical state of LWR high-power rods under irradiation, Journal of Nuclear Materials 84 (1979) 23–25.

[37] H. Matzke, Oxygen potential measurements in high burnup LWR U02 fuel, Journal of Nuclear Materials 223 (1995) 1–5. https://doi.org/10.1016/0022-3115(95)00004-6.

[38] O. Götzmann, A thermodynamic model for the attack behaviour in stainless steel clad oxide fuel pins, Journal of Nuclear Materials 84 (1979) 39–54. https://doi.org/10.1016/0022-3115(79)90149-1.

[39] J. McFarlane, Fission Product Tellurium Chemistry from Fuel to Containment, in: Proceedings on the OECD CSNI Workshop on the Chemistry of Iodine in Reactor Safety, Würenlingen, Switzerland, 1996: pp. 563–585.

[40] Y. Pipon, N. Toulhoat, N. Moncoffre, H. Jaffrézic, S. Gavarini, P. Martin, L. Raimbault, A.M. Scheidegger, Thermal diffusion of chlorine in uranium dioxide, Radiochim Acta 94 (2006) 705–711. https://doi.org/10.1524/ract.2006.94.9-11.705.

[41] F.L. Yaggee, R.F. Mattas, L.A. Neimark, Characterization of Irradiated Zircaloys: Susceptibility to Stress Corrosion Cracking, NP-1557, 1980.

[42] D. Cubicciotti, J.E. Sanecki, Characterization of deposits on inside surfaces of LWR cladding, Journal of Nuclear Materials 78 (1978) 96–111. https://doi.org/10.1016/0022-3115(78)90508-1.

[43] P. Bouffioux, J. Van Vliet, P. Deramaix, M. Lippens, Potential causes of failures associated with power changes in LWR's, Journal of Nuclear Materials 87 (1979) 251–258. https://doi.org/10.1016/0022-3115(79)90561-0.

[44] B.J. Lewis, W.T. Thompson, F.C. Iglesias, Fission product chemistry in oxide fuels, 1st ed., Elsevier Inc., 2012. https://doi.org/10.1016/B978-0-08-056033-5.00042-2.

[45] R.G.J. Ball, W.G. Burns, J. Henshaw, M.A. Mignanelli, P.E. Potter, The chemical constitution of the fuel-clad gap in oxide fuel pins for nuclear reactors, Journal of Nuclear Materials 167 (1989) 191–204. https://doi.org/10.1016/0022-3115(89)90442-X.

[46] D.G. Frost, C.O.T. Galvin, M.W.D. Cooper, E.G. Obbard, P.A. Burr, Thermophysical properties of urania-zirconia (U,Zr)O2 mixed oxides by molecular dynamics, Journal of Nuclear Materials 528 (2020). https://doi.org/10.1016/j.jnucmat.2019.151876.

[47] K.T. Kim, UO2/Zry-4 chemical interaction layers for intact and leak PWR fuel rods, Journal of Nuclear Materials 404 (2010) 128–137. https://doi.org/10.1016/j.jnucmat.2010.07.013.

[48] NEA, State-of-the-Art Report on Multi-scale Modelling of Nuclear Fuels, 2015. www.oecd-nea.org.

[49] M.R. Christensen, D.C. Koelsch, L. Stewart, M.A. Mckinnon, Spent Nuclear Fuel Dry Transfer System Cold Demonstration Project, 2000.

[50] M.G. El-Samrah, A.F. Tawfic, S.E. Chidiac, Spent nuclear fuel interim dry storage; Design requirements, most common methods, and evolution: A review, Ann Nucl Energy 160 (2021). https://doi.org/10.1016/j.anucene.2021.108408.

[51] USNRC, Standard Review Plan for Spent Fuel Dry Storage Systems at a General License Facility Final Report Office of Nuclear Material Safety and Safeguards, 2010.

[52] B. Hanson, H. Alsaed, C. Stockman, D. Enos, R. Meyer, K. B. Sorenson, Gap Analysis to Support Extended Storage of Used Nuclear Fuel, 2012.

[53] USNRC, Potential Rod Splitting Due to Exposure to an Oxidizing Atmosphere During Short-term Cask Loading Operations in LWR or Other Uranium Oxide Based Fuel, 2006.

[54] USNRC, Standard Review Plan for Spent Fuel Dry Storage Systems and Facilities, 2017. http://www.nrc.gov/reading-rm/adams.html.

[55] USNRC, Standard Review Plan for Spent Fuel Transportation, 2019. https://www.nrc.gov/reading-rm/.

[56] J. Belle, Uranium Dioxide: Properties and Nuclear Applications, 1961.

[57] R.J. Mceachern, P. Taylor, A review of the oxidation of uranium dioxide at temperatures below 400°C, 1998.

[58] S.I. Sinkov, C.H. Delegard, A.J. Schmidt, Preparation and Characterization of Uranium Oxides in Support of the K Basin Sludge Treatment Project, 2008. http://www.ntis.gov/ordering.htm.

[59] B.D. Hanson, The Burnup Dependence of Light Water Reactor Spent Fuel Oxidation "D, 1998.

[60] J.-B. Minne, Contribution à la modélisation du couplage mécanique-chimique de l'évolution de l'interface pastille-gaine sous irradiation, 2013.

[61] Cloé Schneider, EVOLUTION PHYSICO-CHIMIQUE ET MECANIQUE DE L'INTERFACE PASTILLE-GAINE DES CRAYONS COMBUSTIBLES DES REACTEURS A EAU PRESSURISEE, 2022.

[62] C. Ciszak, L. Desgranges, P. Garcia, C. Sabathier, L. Fayette, S. Chevalier, On the origins and the evolution of the fuel-cladding bonding phenomenon in PWR fuel rods, Journal of Nuclear Materials 520 (2019) 110–120. https://doi.org/10.1016/j.jnucmat.2019.04.015.

[63] N. Rodríguez-Villagra, L.J. Bonales, S. Fernández-Carretero, A. Milena-Pérez, L. Gutierrez, H. Galán, Exploring a surrogate of Pellet–Cladding interaction: Characterization and oxidation behavior, MRS Adv 8 (2023) 238–242. https://doi.org/10.1557/s43580-022-00475-0.

[64] A. Milena-Pérez, N. Rodríguez-Villagra, S. Fernández-Carretero, A. Núñez, Thermal air oxidation of UO2: Joint effect of precursor's nature and particle size distribution, Progress in Nuclear Energy 159 (2023). https://doi.org/10.1016/j.pnucene.2023.104629.

[65] S. Fernandez, M.I. Nieto, J. Cobos, R. Moreno, CeO2 pellet fabrication as spent fuel matrix analogue, J Eur Ceram Soc 36 (2016) 3505–3512. https://doi.org/10.1016/j.jeurceramsoc.2016.05.052.

[66] A. Milena-Pérez, L.J. Bonales, N. Rodríguez-Villagra, S. Fernández, V.G. Baonza, J. Cobos, Raman spectroscopy coupled to principal component analysis for studying UO2 nuclear fuels with different grain sizes due to the chromia addition, Journal of Nuclear Materials 543 (2021). https://doi.org/10.1016/j.jnucmat.2020.152581.

[67] N. Rodríguez-Villagra, O. Riba, A. Milena-Pérez, J. Cobos, L. Jimenez-Bonales, S. Fernández-Carretero, E. Coene, O. Silva, L. Duro, Dopant effect on the spent fuel matrix dissolution of new advanced fuels: Cr-doped UO2 and Cr/Al-doped UO2, Journal of Nuclear Materials 568 (2022). https://doi.org/10.1016/j.jnucmat.2022.153880.

[68] I. Cohen, R.M. Berman, A METALLOGRAPHIC AND X-RAY STUDY OF THE LIMITS OF OXYGEN SOLUBILITY IN THE UOyThOz SYSTEM, JOURNAL OF NUCLEAR MATERIALS 18 (1965) 77–107.

[69] H. Xiao, X. Wang, C. Long, Y. Liu, A. Yin, Y. Zhang, Investigation of the mechanical properties of ZrO2-doped UO2 ceramic pellets by indentation technique, Journal of Nuclear Materials 509 (2018) 482–487. https://doi.org/10.1016/j.jnucmat.2018.07.035.

[70] A. Arafati, E. Borhani, S.M.S. Nourbakhsh, H. Abdoos, Synthesis and characterization of tetragonal / monoclinic mixed phases nanozirconia powders, Ceram Int 45 (2019) 12975–12982. https://doi.org/10.1016/j.ceramint.2019.03.225.

[71] R. Terki, G. Bertrand, H. Aourag, C. Coddet, Structural and electronic properties of zirconia phases: A FP-LAPW investigations, Mater Sci Semicond Process 9 (2006) 1006–1013. https://doi.org/10.1016/j.mssp.2006.10.033.

[72] S. Kumar, S. Bhunia, A.K. Ojha, Effect of calcination temperature on phase transformation, structural and optical properties of sol-gel derived ZrO2 nanostructures, Physica E Low Dimens Syst Nanostruct 66 (2015) 74–80. https://doi.org/10.1016/j.physe.2014.09.007.

[73] J.M. Elorrieta, L.J. Bonales, N. Rodríguez-Villagra, V.G. Baonza, J. Cobos, A detailed Raman and X-ray study of UO2+: X oxides and related structure transitions, Physical Chemistry Chemical Physics 18 (2016) 28209–28216. https://doi.org/10.1039/c6cp03800j.

[74] J.D. Axz, G.D. Pzttit, Infrared Dielectric Dispersion and Lattice Dynamics of Uranium Dioxide and Thorium Dioxide, n.d.

[75] J. Schoenes, ELECTRONIC TRANSITIONS, CRYSTAL FIELD EFFECTS AND PHONONS IN UO2, 1979.

[76] S. Karcher, R. Mohun, T. Olds, M. Weber, K. Kriegsman, X. Zhao, X. Guo, C. Corkhill, D. Field, J. McCloy, Benefits of using multiple Raman laser wavelengths for characterizing defects in a UO2 matrix, Journal of Raman Spectroscopy 53 (2022) 988–1002. https://doi.org/10.1002/jrs.6321.

[77] D.R. Costa, M. Hedberg, S.C. Middleburgh, J. Wallenius, P. Olsson, D.A. Lopes, Oxidation of UN/U2N3-UO2 composites: an evaluation of UO2 as an oxidation barrier for the nitride phases, Journal of Nuclear Materials 544 (2021). https://doi.org/10.1016/j.jnucmat.2020.152700.

[78] K. Johnson, V. Ström, J. Wallenius, D.A. Lopes, Oxidation of accident tolerant fuel candidates, J Nucl Sci Technol 54 (2017) 280–286. https://doi.org/10.1080/00223131.2016.1262297.

[79] R.D. Scheele, B.D. Hanson, A.M. Casella, Effect of added gadolinium oxide on the thermal air oxidation of uranium dioxide, Journal of Nuclear Materials 552 (2021). https://doi.org/10.1016/j.jnucmat.2021.153008.

[80] H. He, D. Shoesmith, Raman spectroscopic studies of defect structures and phase transition in hyper-stoichiometric UO2+x, Physical Chemistry Chemical Physics 12 (2010) 8108–8117. https://doi.org/10.1039/b925495a.

[81] D. Michel, M.P. y Jorba, R. Collongues, Study by Raman spectroscopy of order-disorder phenomena occurring in some binary oxides with fluorite-related structures, Journal of Raman Spectroscopy 5 (1976) 163–180. https://doi.org/10.1002/jrs.1250050208.

[82] A. Miskowiec, J.L. Niedziela, T.L. Spano, M.W. Ambrogio, S. Finkeldei, R. Hunt, A.E. Shields, Additional complexity in the Raman spectra of U3O8, Journal of Nuclear Materials 527 (2019). https://doi.org/10.1016/j.jnucmat.2019.151790.

[83] I. Butler, G. Allen, T. Nguyen, Micro-Raman spectrum of triuranium octoxide, Appl Spectrosc (1988) 901–902.

[84] M.L. Palacios, S.H. Taylor, Characterization of Uranium Oxides Using in Situ Micro-Raman Spectroscopy, Appl Spectrosc 54 (2000) 1372–1378.

[85] S.N. Basahel, T.T. Ali, M. Mokhtar, K. Narasimharao, Influence of crystal structure of nanosized ZrO2 on photocatalytic degradation of methyl orange, Nanoscale Res Lett 10 (2015). https://doi.org/10.1186/s11671-015-0780-z.

[86] D. Bersani, P.P. Lottici, G. Rangel, E. Ramos, G. Pecchi, R. Gómez, T. López, Micro-Raman study of indium doped zirconia obtained by sol-gel, in: J Non Cryst Solids, 2004: pp. 116–119. https://doi.org/10.1016/j.jnoncrysol.2004.08.006.

[87] A. Milena-Pérez, L.J. Bonales, N. Rodríguez-Villagra, M.B. Gómez-Mancebo, H. Galán, Oxidation of accident tolerant fuels models based on Cr-doped UO2 for the safety of nuclear storage facilities, Journal of Nuclear Materials 582 (2023). https://doi.org/10.1016/j.jnucmat.2023.154502.

[88] L. Quémard, L. Desgranges, V. Bouineau, M. Pijolat, G. Baldinozzi, N. Millot, J.C. Nièpce, A. Poulesquen, On the origin of the sigmoid shape in the UO2 oxidation weight gain curves, J Eur Ceram Soc 29 (2009) 2791–2798. https://doi.org/10.1016/j.jeurceramsoc.2009.04.010.

[89] R.J. Ackermann, A.T. Chang, C.A. Sorrell, THERMAL EXPANSION AND PHASE TRANSFORMATIONS OF THE U3Os_z PHASE IN AIRt, Pergamon Press, 1977.

[90] T.K. Campbell, E.R. Gilbert, C.K. Thornhill, B.J. Wrona, Oxidation Behavior of Spent UO2 Fuel, Nucl Technol 84 (1989) 182–195.

[91] P. Taylor ', D.D. Wood, A.M. Duclos, The early stages of U,O, formation on unirradiated CANDU UO, fuel oxidized in air at 200-300°C *, 1992.

[92] C. Gu E Eneau, M. Baichi, D. Labroche, C. Chatillon, B. Sundman, Thermodynamic assessment of the uranium-oxygen system, n.d. www.elsevier.com/locate/jnucmat.

[93] P. Taylor, Thermodynamic and kinetic aspects of UO2 fuel oxidation in air at 400-2000 K, in: Journal of Nuclear Materials, 2005: pp. 206–212. https://doi.org/10.1016/j.jnucmat.2005.04.043.

[94] G. Rousseau, L. Desgranges, F. Charlot, N. Millot, J.C. Nièpce, M. Pijolat, F. Valdivieso, G. Baldinozzi, J.F. Bérar, A detailed study of UO2 to U3O8 oxidation phases and the associated rate-limiting steps, Journal of Nuclear Materials 355 (2006) 10–20. https://doi.org/10.1016/j.jnucmat.2006.03.015.

[95] S.A. Utlak, J.W. McMurray, Thermodynamic modeling of the U3O8-x solid solution phase, Journal of Nuclear Materials 530 (2020). https://doi.org/10.1016/j.jnucmat.2019.151844.

[96] S. Aronson, R.B. Roof, J. Belle, Kinetic study of the oxidation of uranium dioxide, J Chem Phys 27 (1957) 137–144. https://doi.org/10.1063/1.1743653.

[97] K.S. Kumar, T. Mathews, H.P. Nawada, N.P. Bhat, Oxidation behaviour of uranium in the internally gelated urania-ceria solid solutions - XRD and XPS studies, Journal of Nuclear Materials 324 (2004) 177–182. https://doi.org/10.1016/j.jnucmat.2003.09.014.

[98] C. Jégou, R. Caraballo, S. Peuget, D. Roudil, L. Desgranges, M. Magnin, Raman spectroscopy characterization of actinide oxides (U1-yPuy)O2: Resistance to oxidation by the laser beam and examination of defects, Journal of Nuclear Materials 405 (2010) 235–243. https://doi.org/10.1016/j.jnucmat.2010.08.005.

[99] Y.K. Ha, J. Lee, J.G. Kim, J.Y. Kim, Effect of Ce doping on UO2 structure and its oxidation behavior, Journal of Nuclear Materials 480 (2016) 429–435. https://doi.org/10.1016/j.jnucmat.2016.08.026.

[100] J.M. Elorrieta, D. Manara, L.J. Bonales, J.F. Vigier, O. Dieste, M. Naji, R.C. Belin, V.G. Baonza, R.J.M. Konings, J. Cobos, Raman study of the oxidation in (U, Pu)O2 as a function of Pu content, Journal of Nuclear Materials 495 (2017) 484–491. https://doi.org/10.1016/j.jnucmat.2017.08.043.

[101] R. Eloirdi, P. Cakir, F. Huber, A. Seibert, R. Konings, T. Gouder, X-ray photoelectron spectroscopy study of the reduction and oxidation of uranium and cerium single oxide compared to (U-Ce) mixed oxide films, Appl Surf Sci 457 (2018) 566–571. https://doi.org/10.1016/j.apsusc.2018.06.148.

[102] J.M. Elorrieta, L.J. Bonales, S. Fernández, N. Rodríguez-Villagra, L. Gutiérrez-Nebot, V.G. Baonza, J. Cobos, Pre- and post-oxidation Raman analysis of (U, Ce)O2 oxides, Journal of Nuclear Materials 508 (2018) 116–122. https://doi.org/10.1016/j.jnucmat.2018.05.042.

[103] L. Desgranges, G. Baldinozzi, P. Simon, G. Guimbretière, A. Canizares, Raman spectrum of U4O9: A new interpretation of damage lines in UO2, Journal of Raman Spectroscopy 43 (2012) 455–458. https://doi.org/10.1002/jrs.3054.

[104] J. Lee, C. Kwon, J. Kim, Y.S. Youn, J.Y. Kim, B. Han, S.H. Lim, Integrated study of experiment and first-principles computation for the characterization of a corium type ZrO8 complex in a Zr-doped fluorite UO2, Int J Energy Res 43 (2019) 3322–3329. https://doi.org/10.1002/er.4469.

[105] K.F. Nilsson, O. Martin, C. Chenel-Ramos, J. Mendes, The segmented expanding cone-mandrel test revisited as material characterization and component test for fuel claddings, Nuclear Engineering and Design 241 (2011) 445–458. https://doi.org/10.1016/j.nucengdes.2010.10.026.

[106] R. Nagy, M. Király, D.M. Antók, L. Tatár, Z. Hózer, Dynamic finite element analysis of segmented mandrel tests of hydrogenated E110 fuel cladding tubes, Mater Today Commun 24 (2020). https://doi.org/10.1016/j.mtcomm.2020.101005.

[107] M. Király, Z. Hózer, M. Horváth, T. Novotny, E. Perez-Feró, N. Vér, Impact of thermal and chemical treatment on the mechanical properties of E110 and E110G cladding tubes, Nuclear Engineering and Technology 51 (2019) 518–525. https://doi.org/10.1016/j.net.2018.11.002.

[108] M. Király, M. Horváth, R. Nagy, N. Vér, Z. Hózer, Segmented mandrel tests of as-received and hydrogenated WWER fuel cladding tubes, Nuclear Engineering and Technology 53 (2021) 2990–3002. https://doi.org/10.1016/j.net.2021.03.019.

[109] M. Király, D.M. Antók, L. Horváth, Z. Hózer, Evaluation of axial and tangential ultimate tensile strength of zirconium cladding tubes, Nuclear Engineering and Technology 50 (2018) 425–431. https://doi.org/10.1016/j.net.2018.01.002.

[110] C. Schneider, O. Yetik, L. Duarte, P. Trtik, R. Grabherr, J. Bertsch, Neutron imaging of irradiated fuel rod: contribution of the inner oxide to the contrast, in: NuMat22, Ghent, 2022.

[111] L.I. Duarte, F. Fagnoni, R. Zubler, W. Gong, P. Trtik, J. Bertsch, Effect of the inner liner on the hydrogen distribution of zircaloy-2 nuclear fuel claddings, Journal of Nuclear Materials 557 (2021). https://doi.org/10.1016/j.jnucmat.2021.153284.

[112] C. Schneider, M. Makowska, J. Bertsch, Synchrotron analysis of spent fuel irradiated in BWR: focus on the inner cladding wall, in: MiNES 2023, New Orleans, 2023.

[113] H. Putz, K. Brandenburg, Match! - Phase Analysis using Powder Diffraction, (2023).

[114] V.A. Solé, E. Papillon, M. Cotte, P. Walter, J. Susini, A multiplatform code for the analysis of energy-dispersive X-ray fluorescence spectra, Spectrochim Acta Part B At Spectrosc 62 (2007) 63–68. https://doi.org/10.1016/j.sab.2006.12.002.

[115] C. Lemaignan, Science des matériaux pour le nucléaire, Institut National des Sciences et Techniques Nucléaires, EDP Sciences, Les Ulis, 2004.

[116] C. Schneider, Physical, chemical, and mechanical evolution of the fuel-cladding interface of irradiated PWR fuel rods, UBFC, 2022.

[117] C. Schneider, L. Fayette, I. Zacharie-Aubrun, T. Blay, C. Onofri-Marroncle, C. Sabathier, D. Drouan, J. Sercombe, J. Favergeon, S. Chevalier, Fission products at the fuel-cladding interface of PWR fuel rods: morphological and chemical study, Journal of Nuclear Materials 585 (2023). https://doi.org/10.1016/j.jnucmat.2023.154600.

[118] C. Schneider, M. Makowska, J. Bertsch, Characterisation of the fuel-cladding interface in a high burnup fuel rod by combined µXRD/µXRF, in: NuFuel 2023, Marseille, France, 2023.

Appendix

Table A-1: The results of the mandrel tests with the hydrogenated E110 samples at 20 °C.

Sample No.	Hydrogen content (wppm)	Temperature (°C)	Material	ΔD% (%)	Fmax/Ho (N/mm)	IW (mJ/mm)
PHE-45	0	20	E110	69.91	529.9	2383.3
PHE-130	0	20	E110	57.88	560.8	2175.0
PHE-51	313	20	E110	57.61	519.5	2017.5
PHE-138	475	20	E110	44.27	482.7	2131.1
PHE-58	639	20	E110	43.62	551.2	1663.8
PHE-142	678	20	E110	47.38	577.9	1586.6
PHE-63	725	20	E110	40.38	585.9	1702.8
PHE-146	737	20	E110	43.08	612.9	1502.4
PHE-151	955	20	E110	40.34	688.3	1542.0
PHE-70	1119	20	E110	26.09	702.3	1233.2
PHE-161	1351	20	E110	33.26	772.8	1183.1
PHE-114	1555	20	E110	22.39	838.8	1193.4
PHE-83	1934	20	E110	19.18	830.7	1064.4
PHE-167	2024	20	E110	15.28	843.3	1026.2
PHE-170	2241	20	E110	15.86	858.8	1117.1
PHE-87	2309	20	E110	16.51	851.0	796.1
PHE-91	2531	20	E110	9.98	834.2	525.7
PHE-175	2687	20	E110	14.29	866.2	923.9
PHE-98	2931	20	E110	10.05	842.8	504.0
PHE-95	2973	20	E110	8.85	809.2	393.3
PHE-101	2988	20	E110	12.85	835.0	573.1
PHE-182	3038	20	E110	11.18	832.3	648.7
PHE-179	3081	20	E110	8.41	797.8	443.2

PHE-183	3189	20	E110	9.85	820.7	432.9
PHE-103	3343	20	E110	9.57	785.5	362.9
PHE-186	3454	20	E110	9.37	788.5	526.3
PHE-107	3567	20	E110	9.47	815.9	405.1
PHE-118	3588	20	E110	9.44	808.0	483.5

Table A-2: The results of the mandrel tests with the hydrogenated E110opt samples at 20 °C.

Sample No.	Hydrogen content	Temperature	Material	ΔD%	Fmax/Ho	IW
	(wppm)	(°C)		(%)	(N/mm)	(mJ/mm)
PHG-159	0	20	E110opt	60.55	592.1	2361.6
PHG-74	0	20	E110opt	60.92	592.7	2403.1
PHG-134	310	20	E110opt	54.50	569.8	2046.0
PHG-51	327	20	E110opt	55.59	558.7	2097.6
PHG-139	483	20	E110opt	50.22	600.7	2038.6
PHG-53	489	20	E110opt	47.11	598.8	2047.3
PHG-141	620	20	E110opt	42.15	679.6	1870.9
PHG-147	780	20	E110opt	43.49	758.0	2120.5
PHG-62	781	20	E110opt	38.46	746.9	1968.1
PHG-67	975	20	E110opt	33.16	839.6	1946.5
PHG-149	978	20	E110opt	38.05	817.8	1937.6
PHG-155	1283	20	E110opt	25.91	924.7	1248.1
PHG-626	1499	20	E110opt	23.69	901.7	1245.2
PHG-622	1529	20	E110opt	25.68	987.4	1547.1
PHG-166	1925	20	E110opt	15.56	952.4	1098.8
PHG-633	1968	20	E110opt	22.97	866.6	1019.9
PHG-630	2040	20	E110opt	19.08	885.6	920.1
PHG-83	2059	20	E110opt	12.92	999.7	765.6
PHG-171	2242	20	E110opt	16.03	964.2	1179.1

PHG-87	2388	20	E110opt	12.41	1050.9	802.0
PHG-642	2493	20	E110opt	16.75	915.9	843.1
PHG-174	2724	20	E110opt	11.28	965.7	697.1
PHG-91	2752	20	E110opt	8.89	1037.4	582.9
PHG-97	2841	20	E110opt	9.03	1042.7	520.2
PHG-181	2853	20	E110opt	9.64	969.9	634.7
PHG-95	2966	20	E110opt	7.93	1024.6	443.2
PHG-177	3026	20	E110opt	7.76	927.2	438.0
PHG-99	3206	20	E110opt	12.55	991.2	756.0
PHG-187	3705	20	E110opt	7.49	927.8	430.1
PHG-186	3746	20	E110opt	9.68	1010.9	463.3

Table A-3: The results of the mandrel tests with the hydrogenated samples at 300 °C.

Sample No.	Hydrogen content	Temperature	Material	ΔD%	Fmax/Ho	IW
	(wppm)	(°C)		(%)	(N/mm)	(mJ/mm)
PHE-485	0	300	E110	81.23	204.1	1059.2
PHE-529	0	300	E110	80.68	184.4	1005.1
PHE-489	494	300	E110	60.72	272.0	1074.8
PHE-490	510	300	E110	51.93	271.7	917.0
PHE-501	986	300	E110	55.76	365.4	1318
PHE-502	1010	300	E110	46.50	325.9	1000.6
PHE-506	1490	300	E110	41.98	365.3	994.0
PHE-508	1501	300	E110	36.24	360.6	827.1
PHE-512	1989	300	E110	23.08	342.2	502.9
PHE-516	2008	300	E110	21.64	331.7	450.0
PHE-519	2486	300	E110	18.97	323.6	380.9
PHE-520	2523	300	E110	19.66	343.6	391.3
PHG-601	0	300	E110opt	82.22	204.5	1074.2

PHG-610	494	300	E110opt	62.39	283.6	1130.6
PHG-605	511	300	E110opt	66.77	303.2	1286.1
PHG-614	985	300	E110opt	49.88	414.7	1302.6
PHG-618	1009	300	E110opt	49.68	358.3	1120.5
PHG-625	1483	300	E110opt	31.93	414.2	874.3
PHG-621	1509	300	E110opt	40.14	424.0	1090.5
PHG-629	1994	300	E110opt	22.84	464.6	665.8
PHG-634	2003	300	E110opt	20.58	414.6	513.3
PHG-641	2476	300	E110opt	27.62	396.0	670.8
PHG-637	2496	300	E110opt	21.57	404.9	503.2